VILNIUS UNIVERSITY

CENTER FOR PHYSICAL SCIENCES AND TECHNOLOGY

Andrius Devižis

CHARGE CARRIER TRANSPORT IN CONJUGATED POLYMER FILMS REVEALED BY ULTRAFAST OPTICAL PROBING

Doctoral thesis
Physical sciences, physics (02 P)

Vilnius, 2011

Thesis was prepared at Center For Physical Sciences and Technology (Institute of Physics) in 2006–2010

Scientific supervisor:
habil. dr. Vidmantas Gulbinas (Institute of physics, physical sciences, physics - 02 P)

Introduction

Organic optoelectronics has undergone tremendous development over the recent decades. There are already many commercial products based on organic technology [1]. Manufacturing technologies of organic optoelectronic devices based on solution and printing promise low processing costs, environment-friendly fabrication and disposal. Large scale OLED (organic light emitting diode) displays have fundamental advantages over other existing technologies in terms of the energy consumption efficiency. Mechanical flexibility is another attractive and unique feature of organic devices. However, there is a lot of space for improvement, and deeper fundamental knowledge about electronic processes in organic materials is required.

Conjugated polymers are promising candidates for applications in all kinds of organic optoelectronic devices: OLEDs, organic field-effect transistors (OFETs) and organic photovoltaic cells. In the future they are likely to replace small molecular weight materials in organic devices, since solution-based polymer processing is cheaper in comparison to vacuum deposition of small organic molecules. π – bonds of the conjugated polymer backbone have large degree of electron delocalization and, thus, determine good intrachain transport of the electric charge. Over the recent decade, studies on photophysics of polymers have mainly been focused on *homo*-polymers such as poly(phenylene-vinylene)s or polyfluorenes [2]. Current state-of-the-art materials, however, are often *co*-polymers with four or more chemically different subunits [3]. Each unit carries one or more functionality ranging from enhancing the solubility, suppression of aggregation to modification of charge transport, recombination, and light emission properties. It turned out that *co*-polymers based on fluorene are suitable as emitters to cover the entire visible spectrum in OLED or lasing applications [4]. Mixtures (blends) of electron and hole transporting fluorene *co*-polymers are efficient as charge generation and transport layers in bulk heterojunction photovoltaic devices [5]. To increase the thermal and electrical stabilities of polyfluorenes, introduction of a spiro-linked fluorene has proven to be successful [6]. Efficient light output was maintained in polyfluorene based OLEDs as well [7].

Charge carrier mobility is one of the crucial parameters that determine applicability of organic semiconductors. Despite record braking bulk mobilities above

10 cm^2/Vs in single cystalline organic materials [8], polymers have characteristic mobilities of the order of $10^{-2} – 10^{-6}$ cm^2/Vs [9]. A common approach is that charge transport in disordered organic materials occurs via temperature-activated hopping and is relatively slow [10]. Based on calculations of the charge transfer integrals in organic solids [11] and effective-mass calculations of charge carriers in conjugated polymers [12] a charge mobility as high as 1000 cm^2/Vs can be predicted under ideal conditions. The calculated effective carrier mass agrees with experimental results obtained in single crystalline polydiacetylenes [13]. Thus, it appears that high mobilities in organic solids might be feasible. This is further substantiated by recent studies of optical coherence in these materials [14]. Microwave conductivity measurements in a ladder-type polyphenylene (MeLPPP) have shown that the one-dimensional mobility is close to 600 cm^2/Vs [15]. On the contrary, the average bulk mobility in amorphous organic semiconductors is orders of magnitude lower. Apparently, the conventional mobility, which is commonly assumed as being constant in time, might not be sufficient to fully describe charge transport on the nano scale, such as in organic devices. Considering that the size of organic device structures ranges from almost molecular dimensions to micrometer length, it is a challenge to probe charge transport on vastly different time scales ranging from femtoseconds to microseconds. Insight into mobility dynamics could improve charge transport models. However, it was not possible to probe the time-resolved charge carrier drift in disordered organic materials on ultrafast time scales due to the lack of an appropriate experimental method.

A novel experimental method for the charge carrier mobility investigation on ultrafast time scales in organic films and devices was developed in the course of this thesis in the laboratory of Molecular compound physics (Institute of Physics). It is based on time-resolved electric field-induced second harmonic generation (TREFISH). Electric field-induced second harmonic generation (EFISH) is commonly used for the determination of molecular hyperpolarizability and surface chemistry investigations [16, 17, 18]. A pump-probe version of the method has been applied to investigate the electric field dynamics on interfaces of inorganic semiconductors [19] and ultrafast electrical pulses propagating on thin-film microstrip lines [20]. The second harmonics cannot be generated in amorphous and other centrosymmetrical materials. The centrosymmetry can be broken by the

application of an external electric field. The second harmonic generation efficiency then is proportional to the hiperpolarizability of the material and to the second power of the applied field. Any process changing the electric field distribution in the material will affect the measured temporal second harmonic (SH) signal; thus, the SH intensity can be considered being a good probe for changes of the electric field strength due to charge motion. The TREFISH method is applicable to all π-conjugated organic materials, and its time resolution is limited only by the duration of the optical pulses used. Manaka *et al*. [21] also employed EFISH for direct observation of the carrier motion with low temporal resolution in OFET.

The main goal of this work was to investigate transport features of photogenerated electrical charge by means of TREFISH technique in π-conjugated polymers. The main attention was focused on transport dynamics of the photogenerated charge carriers. Several **tasks** have been completed to achieve this goal. TREFISH measurement setup was implemented in the laboratory of Molecular compounds physics, and applicability of the method has been verified. Measurements were performed on three different model polymers: methyl substituted ladder-type poly(para-phenylene) (MeLPPP), poly(fluorene-co-benzothiadiazole) (F8BT) and poly(spirobifluorene-co-benzothiadiazole) (PSF-BT), having different morphological and chemical structure. Relaxation of the excited state and generation of the charge carriers in a new co-polymer PSF-BT have been determined by means of time and spectrally-resolved fluorescence, field-induced fluorescence quenching, optical pomp-probe and electromodulated differential absorption (EDA) measurements. These findings provided complementary information for determination of charge transport properties from TREFISH measurement data. It concerns details of the charge carrier generation, exciton density dynamics and other peculiarities of the excited state evolution. Temperature dependences were investigated for the examination of temperature-activated transport concept. Monte-Carlo computer simulations within the framework of Gaussian disorder model were performed to interpret motion of the electric charge carrier on short time and length scales.

Several polymers have been investigated. The MeLPPP was selected since its optical and electrical properties are well studied [9, 22]. It has a low intrinsic disorder due to the rigid molecular subunits constituting its backbone. Its peculiar structure leads to favorable on-chain [15] and bulk mobilities [23]. PSF-BT is an

amorphous and disordered conjugated co-polymer with the spiro-linked fluorene side group. The morphology of the co-polymer F8BT film can be tuned by annealing on oriented substrates due to its liquid crystalline properties [24]. This feature was exploited in order to elucidate the morphology role on charge transport. F8-BT and PSF-BT showed different excited state relaxation patterns. This elucidated influence of spiro-linkage to the polymer photophysics, as the structure of these materials is very alike except that spiro-linkage is absent in F8-BT.

Novelty and importance. Dynamic behavior of the photogenerated charge carrier transport in π-conjugated polymers has been experimentally examined in detail for the first time. These findings provide knowledge about charge transport mechanisms in polymers. Also, they may give guidelines for the designers of organic electronic devices.

Layout of the thesis. Chapter 1 overviews π-conjugated polymers and polyfluorenes as class of materials in general. It also briefly overviews conceptual approaches of electrical charge transport in disordered solids and experimental methods employed for investigations of charge carrier mobility. In chapter 2 properties of investigated polymers (MeLPPP, PSF-BT, F8BT) are discussed, and the TREFISH method, which is the fundamental point of this thesis, is introduced. Chapters 3 and 4 are dedicated to the investigation of excited state relaxation and charge carrier generation in PSF-BT polymer. They provide supplementary information to the next chapters where charge transport dynamics is examined by means of TREFISH. Chapter 5 presents mobility dynamics of the photogenerated charge carriers in MeLPPP and PSF-BT. Results of the measurements at different temperatures are shown in chapter 6. They imply temperature-independent initial transport. Chapter 6 also demonstrates the influence of film morphology on charge transport. Multiphase transport concept is suggested here relying on results obtained for samples of different composition and intrinsic ordering.

The author's contribution. Most of the technical experimental work including development of the experimental setup and programming tasks of the experiment control and data acquisition has been performed by the author. The author performed the majority of experimental investigations. Sample preparations, measurements of electrochemical potentials and quantum chemical calculations have been performed by German colleagues. However, these works are the integral part of

investigation and, therefore, are included into this thesis. The author also wrote the computer code for Monte Carlo simulations and performed these numerical experiments. The author contributed to the data analysis and preparation of publication manuscripts.

Acknowledgment. The author is very grateful to his scientific supervisor habil. dr. Vidmantas Gulbinas and dr. Dirk Hertel. Thanks to all people who have helped and assisted the author in preparation of this thesis.

The main statements:

1. The developed time-resolved electric field-induced second harmonic generation method enables investigation of ultrafast charge carrier dynamics in conjugated polymers.

2. Mobility of photogenerated charge carriers on ultrafast time scale is orders of magnitude higher in comparison to stationary values. Mobility experiences rapid relaxation during one nanosecond from approximately 10^{0} and 10^{-1} to 10^{-3} and 10^{-4} cm^2/Vs in MeLPPP and PSF-BT polymers, respectively.

3. The structural hierarchy of conjugated polymers causes dynamics of the charge carrier transport; motion along conjugated segment or single polymer chain is fast and hopping between separate chains corresponds to slow macroscopic transport.

List of publications that constitute basis of this thesis:

[A1] A. Devižis, K. Meerholz, D. Hertel, V. Gulbinas, "Hierarchical charge carrier motion in conjugated polymers", *Chem. Phys. Lett*., **498**, 302 (2010).

[A2] A. Devižis, K. Meerholz, D. Hertel, V. Gulbinas, "Ultrafast charge carrier mobility dynamics in poly(spirobifluorene-*co*-benzothiadiazole):Influence of temperature on initial transport", *Phys. Rev. B*, **82**, 155204 (2010).

[A3] A. Devižis, A. Serbenta, D. Peckus, A. Thiessen, R. Alle, D. Hertel, V. Gulbinas, „Electric field assisted charge carrier photogeneration in poly(spirobifluorene-*co*-benzothiadiazole)", *J. Chem. Phys*., **133**, 164904 (2010).

[A4] A. Devižis, A. Serbenta, K. Meerholz, D. Hertel, V. Gulbinas "Ultrafast Dynamics of Carrier Mobility in a Conjugated Polymer Probed at Molecular and Microscopic Length Scales", *Phys. Rev. Lett*., **103**, 027404 (2009).

[A5] A. Devižis, A. Serbenta, K. Meerholz, D. Hertel, V. Gulbinas "Excited state relaxation in poly(spirobifluorene-co-benzothiadiazole) films", *J. Chem. Phys.*, **131**, 104902 (2009).

[A6] A. Devižis, A. Serbenta, D. Hertel and V. Gulbinas „Exciton and Polaron Contributions to Photocurrent in MeLPPP on a Picosecond Time Scale“ *Molecular Crystals and Liquid Crystals*, **496**, 16 (2008).

List of conference theses

1. D. Peckus, A. Devižis, V. Gulbinas “Exciton-exciton annihilation and charge carrier generation in fluorene based conjugated polymers”. Developments in optics and communications 2010 (Latvia, Riga, 2010).

2. A. Devižis, D. Hertel, V. Gulbinas “Multiphase charge carrier transport in conjugated polymers”. 8-th international conference on Electronic processes in organic and inorganic materials (Ivano-Frankivsk, Ukraine, 2010).

3. A. Devižis, D. Peckus, V. Gulbinas, D. Hertel “Exciton dynamics and charge carrier generation in multifunctional fluorene-based conjugated polymers”. Baltic polymer symposium 2010 (Palanga, Lithuania, 2010).

4. A. Devižis, D. Hertel, V. Gulbinas “Ultrafast charge carrier transport in conjugated polymers”. COST D35 workshop: Controlling photophysical properties of metal complexes: toward molecular photonics (Prague, Czech Republic, 2010).

5. A. Devižis, D. Hertel, V. Gulbinas “Multiphase motion of photogenerated charge carrier in conjugated polymers” VII international Krutyn summer school 2010: Organic Optoelectronics on the move (Krutyn, Poland, 2010).

6. A. Devižis, A. Serbenta, D. Hertel, V. Gulbinas “Initial carrier mobility in conjugated polymers probed by electric field-induced second harmonic”. Frontiers in Polymer Science : International symposium celebrating the 50th Anniversary of the journal Polymer (Mainz, Germany, 2009).

7. A. Devižis, A. Serbenta, D. Hertel, V. Gulbinas “Excited state relaxation in polyspirobifluorene-co-benzothiadiazole films”. XIX International school-seminar: Spectroscopy of molecules and crystals; devoted to the 175th Anniversary of Kyiv Taras Shevchenko University (Beregove, Ukraine, 2009).

8. A. Devižis, V. Gulbinas “Krūvininkų judrio konjuguotuosiuose polimeruose nustatymas panaudojant elektriniu lauku indukuotą antrosios optinės harmonikos generaciją”. 38-oji Lietuvos nacionalinė fizikos konferencija (Vilnius, 2009).

9. A. Serbenta, A. Devižis, V. Gulbinas “Sužadintos būsenos relaksacija konjuguotame polispirobifluoreno-benzotiadiazole” 38-oji Lietuvos nacionalinė fizikos konferencija (Vilnius, 2009).

10. A. Devižis, D. Hertel, V. Gulbinas “Initial carrier mobility in conjugated polymers probed by electric field-induced second harmonic”. Electronic processes in organic materials : 7-th international conference (Lviv, Ukraine, 2008).

11. A. Devižis, A. Serbenta, D. Hertel, V. Gulbinas “Initial carrier mobility in conjugated polymers probed by electric field-induced second harmonic”. COST D35 - ESF DYNA conference "Electronic excited states in condensed phases" (Santa Tecla, Italy, 2008).

12. A. Devižis, A. Serbenta, V. Gulbinas “Antrosios harmonikos generacijos panaudojimas ultrasparčiosios elektrinio lauko dinamikos polimerinėse plėvelėse tyrimams” 37-oji Lietuvos nacionalinė fizikos konferencija (Vilnius, 2007).

List of author’s publications not included into the thesis:

[] A. Devižis, V. Gulbinas “Kinetics of the real and imaginary permittivity parts of silver revealed by surface plasmon resonance method” *Appl. Opt.* 47, 10, 1632-1637 (2008)

[] A. Devižis, V. Vaičikauskas, and V. Gulbinas, "Ultrafast pump-probe surface plasmon resonance spectroscopy of thin gold films," *Appl. Opt.* **45**, 2535-2539 (2006)

1 Literature survey

1.1 Conjugated polymers

Charge transport is a key aspect of any material used in electronic devices. Heavily halogen-doped polyacetylene films exhibit conductivity of 10^5 S/m [25]. Admitting the importance of the field, Nobel Prize in chemistry (2000) was awarded for the development of electrically conductive polymers [26]. Doping modifies the density of the charge carriers but the ability to transport these carriers arises from delocalization of electron wave function, be it doped organic conductors or pure organic semiconductors. π-bonds are responsible for delocalization of electron density in π-conjugated polymers. A carbon atom has four electrons in the outer shell and the electron configuration is $2s^2 2p_x 2p_y$. These orbitals can constitute hybrid orbitals by mixing in the following way: $2s^2 2p_x 2p_y \rightarrow 2s2p_x 2p_y 2p_z \rightarrow 3\cdot\left(sp^2\right)p_z$ [27], the last superscript "2" does not refer to the number of electrons. It means that hybrid orbital sp^2 is mixed of one *s* and two *p* orbitals. Orbitals sp^2 make σ-bonds and p_z orbital makes π-bond in a chemical compound. There are two other types of hybrid orbitals: sp and sp^3. The simplest examples of these are found in acetylene and methane, respectively. However, sp^2 hybridization is of major importance to π-conjugated polymers. sp^2 hybridized carbon atoms constitute the backbone of the conjugated polymer where single and double bonds between carbon atoms alternate one after other as in polyacetylene. It was confirmed by X-ray diffraction [28, 29], electron diffraction measurements [30] and numerical calculations [31] that single and double bonds indeed alternate in polyacetylene. These findings provide slightly different values of the bond length, but they clearly show difference in the length of double and single bonds. Contrarily, the bonds between carbon atoms are identical in benzene, and quantum chemical calculations show delocalization of electron density over the ring of six atoms. Delocalized character of the electron density provides charge transporting abilities to the systems of sp^2 hybridized carbon atoms, *i. e.* charge added to the system at one spatial location may be removed from the other afterwards. Delocalization does not extend over the whole macromolecule due to

physical and chemical defects, which suppress charge transport. Usually the conjugation length extends from several up to a few tens of monomer units, *i.e.* 1,5÷5 nm [27].

σ-conjugation exists as well, for example polysilanes are σ-conjugated polymers. However, these belong to completely different (silicon based) class of materials and are out of scope of this work.

Polyfluorenes (fluorene is shown in Fig. 1.1) are conjugated polymers that meat all requirements for electro-optical applications concerning processing aspects, high photoluminescence quantum yield and possibility to control physical (optical) properties via chemical modification of substituents in the position 9,9 [32] or by copolymerization. For instance, Pei *et al.* demonstrated green electroluminescence of polyfluorene copolymerized with bithiophene [33]. 9,9-Dioctylfluorene copolymerized with 4,7-di-2-thienyl-2,1,3-benzothiadiazole exhibited electroluminescence in a red spectral range [34]. Unmodified polyfluorenes are blue emitters. Thus, polyfluorenes are attractive materials for display applications.

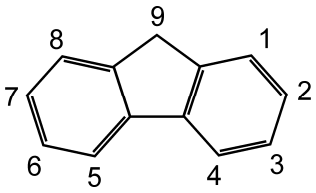

Fig. 1.1 Fluorene.

Spiro linkage is a connection of two π-conjugated molecular segments via a common sp^3-hybridized carbon atom (Fig. 1.2). The π-conjugated system is planar by its nature, except specific compounds such as fullerenes and carbon nanotubes. Therefore, segments of the molecule linked by a spiro atom are perpendicular to each other (Fig. 1.2). Initially, the use of spiro-linkage was driven by the need to prevent crystallization of low molecular mass compounds in organic electronic divices [35]. However, it has turned out that it has benefits in polymer materials as well [36]. Recently it has been demonstrated that spiro-linked side groups improve thermal and optical stability of blue light-emitting spiro-bridged ladder-type poly(*p*-phenylene) [7]. The copolymerization of spirobifluorene with a hole transporting phenylene-diamine (TPD) improved the efficiency in blueemitting OLEDs significantly [37]. The hole transporting TPD has a lower oxidation potential compared with the polyfluorene making it a trap for holes relative to the polyfluorene

[37]. The alkoxy substituted spiro groups have a similar oxidation potential. Thus, they play a role in charge transport via trapping and introducing dipolar disorder. In this respect the spiro unit plays an active role in charge transport instead of only stabilizing morphology. It is known that side chains play an important role in the photophysics of, *e.g.*, poly-(9,9 dioctyl)fluorene, but more indirect via changing the morphology. It is, thus, much more challenging to develop reliable structure-property relations.

The focus of research in the field of OLEDs has shifted to white light emitting polymers. The electronic properties are much more complex in materials used in these devices. They do not only need different charge transporting capabilities of different subunits but also have to secure efficient energy transfer. Since polyfluorenes have a large optical gap, efficient white emission can only be obtained with red-emitting chromophores polymerized into the chain [3]. Since the overlap of emission and absorption spectra usually limits the energy transfer rate, chromophores emitting in the green spectral range are also polymerized into the chain [38]. These chromophores, however, have not only to increase the energy transfer rate but also function as an emitter to enable white light emission.

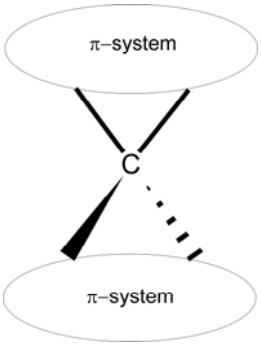

Fig. 1.2 Spiro compound [36].

The role of conjugated side groups such as the spirofluorene for the excited state properties of polyspirofluorenes is much less investigated. Due to the different energy levels of the constituting subunits, one can expect a rich variety of photophysical phenomena in these materials.

1.2 Charge transport in disordered organic materials

Disordered organic solids exhibit completely different features of the charge transport in comparison with molecular crystals. Increase of temperature, for instance, stimulates scattering and suppresses the coherent transport in crystals. It is *vice versa* in disordered materials where stochastic hops of the charge carriers are temperature-activated. From the technological point of view organic crystals cannot compete with disordered organic materials due to poor mechanical properties and impossibility to grow large-scale pure crystals [39]. Therefore, scientific investigations, which started on organic crystals several decades ago, eventually became focused on disordered polymer or vapor-deposited films of small organic molecules.

Adding or removing the electron to or from the molecule, a polymer chain or its segment will always cause redistribution of electron density and, thus, a change of bond lengths (conformational relaxation). These processes lead to the reduction of total energy and formation of a quasi-particle named polaron. Electrical charge becomes self-trapped and cannot be transmitted to neighboring moiety without assistance of external field or thermal energy. It is widely accepted that polaron effects play a major role in crystals, while in polymer films they are overyielded by static structural disorder of the polymer film [2].

Theoretical models of the charge transport can be developed and verified by analyzing the influence of temperature and electric field on experimental observations and theoretical predictions. Observations have revealed that mobility of charge carriers increases with an increase of the electric field strength and obeys the law of Poole-Frenkel:

$$\mu = \mu_0 \exp(\gamma \cdot \sqrt{E}), \tag{1.1}$$

at fields of $10^4 \div 10^6$ V/cm. Here μ_0 is the constant and γ is the positive material specific coefficient. However, deviation appears at lower fields eventually leading to the reduction of the mobility with an increase of the electric field strength [40, 11]. Empirical equation, which accounts for low field behavior, was introduced by W. G.

Gill in 1973. It interconnects mobility with the strength of the electric field and temperature:

$$\mu = \mu_0 \exp\left(-\frac{\Delta_0 - \gamma \cdot \sqrt{E}}{kT_{\text{eff}}}\right); \tag{1.2}$$

here Δ_0 is the activation energy and T_{eff} is an "effective" temperature defined as: $1/T_{\text{eff}} = 1/T - 1/T^*$ (T^* is the temperature when mobility becomes independent of the electrical field) [40]. Bässler *et al.* employed Monte Carlo computer simulations of the charge transport. Computer simulations mimicked the field dependence of non-Poole-Frenkel type if coupling disorder was introduced. The explanation for decrease of mobility with an increase of the field strength is as follows. Due to different coupling between sites the fastest route for the carrier is not necessarily the straight one. At lower fields carriers may escape dead ends via hopping against the field, but strong directionality prevents this at higher fields. The model developed by Bässler *et al.* assumes that charge carriers are localized at sites characterized by intrinsic energy and transport proceeds via hopping between these sites. The site energies are scattered due to disordered nature of the material and the distribution is Gaussian:

$$p(\varepsilon) = \frac{1}{\sqrt{2\pi\sigma^2}} \exp\left(-\frac{\varepsilon^2}{2\sigma^2}\right). \tag{1.3}$$

Thus, the model is often referred to as a Gaussian disorder model. Here $p(\varepsilon)$ is the probability density function, ε is the site energy determined with respect to the average energy and σ is the standard deviation, which characterizes the width of DOS. There is no clear evidence that Gaussian distribution is the correct form of DOS. The Gaussian-shaped profiles of absorption bands only indirectly support this assumption. There are reports that claim a more complex shape of DOS [41, 42]. Monroe proposed the model for hopping in exponential DOS [43]. Wissenberg and Matters claim that DOS in OFETs may be considered as exponential [44], which, in fact, approximates the tail of Gaussian DOS [45]. The next concern besides the DOS shape is the probability for the carrier to hop from one site to another. Miller-Abrahams hopping rate [46] (see for details chapter 2.5) works well for systems with weak electron-phonon coupling. Miller-Abrahams expression predicts the same probability for downward hops. Thus, it assumes that downward hops cannot be accelerated by the electric field and that there is always a coupled vibrational mode to

absorb the excess energy. Marcus expression [47] is the other choice that accounts for polaron effects and has an inverted region. Namely the inverted region, the decrease of downward hop probability with an increase of driving force above some extent, is the major implication of Marcus hopping rate [11].

In the Gaussian disorder model the cubic lattice describes geometrical localization of the sites, and spatial disorder is introduces by attributing a random coupling parameter to each site. This parameter is also taken from the Gaussian distribution and determines a prefactor for hop probability. It reflects non-uniform overlap of wavefunctions of different sites in a real disordered solid. Off-diagonal disorder is the other term referring to spatial disorder and diagonal disorder refers to energetic disorder. These terms came from matrix representation of wavefunctions.

Based on Monte Carlo calculations with Miller-Abrahams hopping type the following relation between mobility temperature and the electric field was established [10]:

$$\mu(T,E)=\mu_0\exp\left(-\left(\frac{2}{3}\frac{\sigma}{kT}\right)^2\right)\cdot\begin{cases}\exp\left[C\left(\left(\frac{\sigma}{kT}\right)^2-\Sigma^2\right)\sqrt{E}\right], \text{for}\,\Sigma\geq 1{,}5,\\ \exp\left[C\left(\left(\frac{\sigma}{kT}\right)^2-2{,}25^2\right)\sqrt{E}\right], \text{for}\,\Sigma<1{,}5.\end{cases} \tag{1.4}$$

Here C is the empirical constant and Σ is the parameter related to off-diagonal disorder. Still expression (1.4) was applicable to relatively high field limit (above 10^5 V/cm). Completely random distribution of site energies was found to be too rough [48, 49, 50, 51]. Dunlop *et al.* have shown that correlation between adjacent site energies arises from interaction of charge carrier with permanent or induced electrical dipoles [48]. The correlation function $C(r)$ is inversely proportional to the first power of distance between sites r [49]:

$$C(r)=\langle\varepsilon(0)\cdot\varepsilon(r)\rangle\sim\frac{1}{r}. \tag{1.5}$$

The validity of the correlated disorder model extends to low fields in comparison to GDM.

Considerations above neglect interaction of carriers and influence of concentration. At high concentrations mobility increases because deep traps become populated and the other carriers move more rapidly despite increased scattering [52]. Charged traps act as scattering centres.

The temperature dependence of the mobility varies depending on a particular system under investigation. Conventionally, the observed temperature dependence of the mobility follows the form of $\mu \sim \exp\left[-(T_0/T)^2\right]$ according to (1.4) or the correlated disorder model. T_0 is related to diagonal disorder σ. The deviation from a conventional Arrhenius activated transport is related to temperature dependence of the equilibrium transport energy in a disordered material with a Gaussian shaped density of states. For a detailed discussion the reader is referred to [10]. Recently, it has been found that the temperature dependence of the mobility is best described by an Arrhenius-like law ($\mu \sim \exp(-\Delta/kT)$, Δ is the activation energy), in a variety of materials [53, 54]. Coropceanu *et al.* [11] claim that both relations in general fit the experimental observations within experimentally available temperature intervals.

The elucidation of the detailed transport process is still lacking due to limited information about the dynamics of charge transport. In conventional experiments the carrier mobility is averaged in time, and information about its dynamics is not accessible. Time-resolved investigations are necessary to obtain details of this process. Fast time and short length scales are important because the active layers of the organic opto-electronic devices such as OLEDs or solar cells are of the order of tens of nanometers, only. Consider for example photoexcitation of a polymer in a solar cell. The excess energy of a photon might be used to increase the mobility of carriers within tens of picoseconds after generation. On the scale of this dimension non-stationary effects can manifest themselves as reported in [55]. Juška *et al.* employed integral mode TOF [56, 57] to elucidate initial transport of the photogenerated charge carriers. They obtained the same fast initial transport distance for two different polymers RRa-PHT and PFB. It exceeded a few tens of nanometers and was electric field-dependent. The initial transport on a picosecond time scale escaped determination due to limited time resolution of TOF measurements. Higher time resolution was demonstrated by Lee *et al.*, who implemented photoconductivity probing with the ultrashort electrical pulses by using the Auston strip line technique ensuring time resolution of tens of picoseconds [58]. Their investigations showed fast, temperature-independent photoconductivity during initial hundreds of picoseconds in PPV polymer. It was attributed to the interband carrier generation. However, their model for charge generation and transport is meanwhile obsolete, thus

making the data analysis questionable. Several attempts have been made to examine initial transport processes with better time resolution using pulse-radiolysis time-resolved microwave conductivity (TRMC) [59] or terahertz spectroscopy methods [60]. All of the above mentioned techniques have serious drawbacks that limit their application. With TRMC, free carriers are probed on the molecular dimensions only, often in a liquid solution. Highly sophisticated modeling has to be used to extract information on the mobility and the obtained values are time-averaged. Ultrafast terahertz spectroscopy allows time resolution of less than 1 ps [60] but the data interpretation is not straightforward. It was demonstrated that the Stark shift of absorption bands can be used as an ultrafast probe of charge drift dynamics in conjugated polymer MeLPPP [61]. Later, this method has been applied to the investigation of the initial carrier mobility in [6, 6]-Phenyl C_{61}-butyric acid methyl ester (PCBM) [62]. The time resolution of the Stark shift method is limited by the light pulse duration only. However, its application is limited to a relatively narrow class of materials with a clearly observed Stark shift, and its experimental realization is relatively difficult, particularly for materials without absorption bands in the visible spectral range. Moreover, treatment of the obtained experimental information is complicated because the absorbance dynamics caused by the Stark shift appears in the same spectral region and in the same time domain as the transient absorption related to excitons. Generally speaking, interest in the field of charge transport in organic materials remains.

1.3 Experimental methods for the mobility investigation

Mobility of charge carriers is the quantity used to describe the ability of the material to transport the electrical charge. Charge carriers that are present in a material manifest diffusive motion if there is no external electrical field. The diffusion coefficient D relates to the mobility μ *via* the Einstein's equation:

$$\frac{\mu}{D} = \frac{e}{kT}. \tag{1.6}$$

Once the external electric field is applied, carriers will tend to drift in (holes) or against (electrons) the direction of the field. The average drift velocity is proportional to the strength of the electric field and drift mobility expresses this proportionality:

$$\langle \vec{v} \rangle = \boldsymbol{\mu}_{\text{drift}} \cdot \vec{E}. \tag{1.7}$$

In general, mobility $\boldsymbol{\mu}_{\text{drift}}$ is the tensor of the second rank with six independent components [63]. Equation (1.7) becomes scalar in fully amorphous materials: $\langle v \rangle = \mu_{\text{drift}} \cdot E$. It is worth noting that μ_{drift} does not always obey the Einstein's equation (1.6) and this phenomenon is referred to as dispersive transport. In addition, the mobility in disordered materials is field-dependent, which makes definition (1.7) slightly ambiguous. Nevertheless mobility is a widely used quantity, noting the strength of the electric field. Usually, the mobility is expressed in units of $\text{cm}^2/(\text{V} \cdot \text{s})$.

Time of flight (TOF). The idea of TOF measurement is very simple. The film made of the investigated material is sandwiched between two electrodes. One of the electrodes is transparent to light. Short exposure to light creates charge carriers near the transparent electrode and they start to drift towards the opposite electrode under the applied external electrical field (Fig. 1.3). The photocurrent is measured with the oscilloscope. Time duration between the light pulse and the moment when the carriers reach the electrode (the current drops) is called the drift time t_{d}. Knowing the drift time the mobility can be easily calculated for given values of the film thickness and the applied voltage:

$$\mu = \frac{D^2}{V_0 \cdot t_{\text{d}}} \tag{1.8}$$

Mobility of holes and electrons is measured separately by changing bias polarity. Kepler [64] and LeBlanc [65] were the first who used this technique to measure carrier mobility in organic solids.

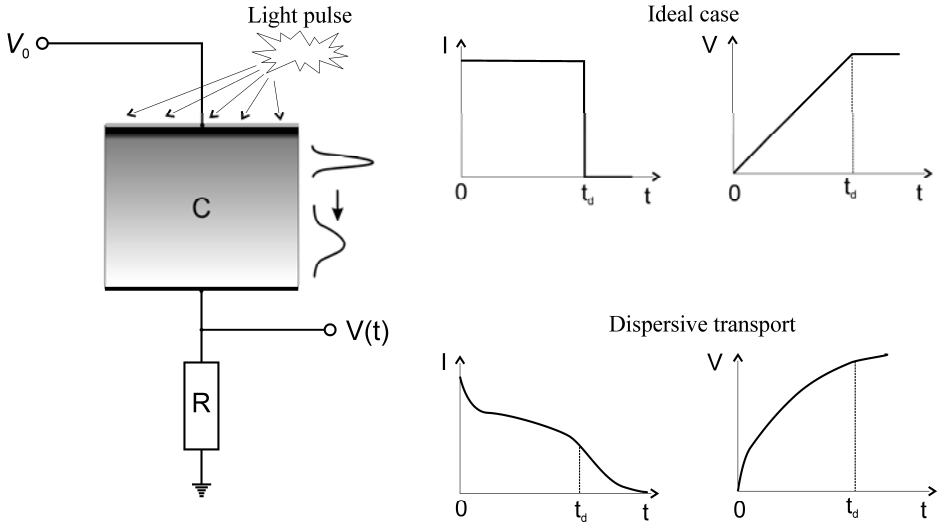

Fig. 1.3 Principal electric scheme of the TOF measurement setup. Current I (differential mode) and voltage V (integral mode) diagrams in the ideal case and in the case of dispersive transport.

The current is obtained by measuring the voltage on the load resistor having the resistance *R* (Fig. 1.3). The sample is like a capacitor having the capacitance *C*. Time constant *RC* has to be properly chosen. It should be much less than the drift time or much longer than the drift time. The former condition determines a differential mode of the measurement and the latter condition determines an integral mode of the measurement. Current as a function of time is registered if a differential mode is used. If the integral mode is chosen, the integrated current (transmitted charge) is registered. Basically, the current is the subject of interest. Thus, temporal derivative of the obtained result has to be calculated. Thin films lead to the large capacitance of the sample and prevent availability of the differential mode.

Other conditions also have to be fulfilled. The field inside the investigated film has to be uniform [66]. Therefore, the amount of the generated charge has to be much smaller than the charge stored on the electrodes of the capacitor-type sample. Limitation concerns dark conductivity, TOF cannot be employed if conductivity exceeds 10^{-10} Sm^{-1} [9]. Naturally, duration of the light pulse used to create carriers has to be much shorter than the drift time.

If all carriers moved with the same speed, the current would emerge together with the excitation pulse and would end instantaneously as soon as carriers

reach the electrode. This is shown in the upper part of Fig. 1.3. However, the speed of the carriers is statistically distributed, and a sharp drop of the current is blurred by the slower carriers. This phenomenon is known as dispersive transport. Characteristic diagrams of differential and integral mode measurements in case of dispersive transport are depicted in the lower part of Fig. 1.3. The sheet of generated carriers also tends to spread due to diffusive motion and repulsive forces between carriers.

TOF also manifests a sharp peak of current at the moment of photoexcitation. This peak is caused by non-stationary transport as the photogenerated carriers initially have excess energy and rapidly move relaxing within DOS. This non-stationary phase takes place on a picosecond time scale and is not resolved by the TOF measurement because of the limited time resolution.

For determination of the drift distance one assumes that the spatial distribution of photogenerated charge is close to the delta function in the vicinity of a transparent electrode. This assumption is reasonable if absorption of the material at a given excitation wavelength is rather strong and the film is rather thick. Homogeneous excitation of the film volume is the peculiarity of thin films. Drift time can be obtained for homogeneous carrier generation in bulk as well. However, clear evaluation of the drift time becomes even more complicated because of dispersive transport.

The applicability of TOF is limited to the class of materials where charge carriers can be generated by light. In opposite case the additional thin layer of photogeneration material helps to overcome this obstacle. The carriers are generated in this photogeneration layer and injected into the investigated layer.

Carrier extraction by linearly increasing voltage (CELIV). This method has been developed in Vilnius University Faculty of Physics and firstly was implemented to study charge transport in microcrystalline silicone [67]. CELIV can be applied to investigation of relatively conductive materials. This is the main advantage versus TOF. Besides, intrinsic charge carriers are probed by CELIV technique. The experimental equipment is very similar to the one used for TOF. The difference is that a triangular pulse of the linearly increasing voltage is applied to the sample. A schematic representation of the applied pulse and the observed current is shown in Fig. 1.4. It should be noted that CELIV requires the blocking contacts, which prevent

injection of the carriers from electrodes. A step-like increase of the current at the beginning of the voltage pulse is related to the capacitance of the sample and does not carry any meaningful information concerning charge transport. An increase of the current continues with an increase of the voltage, reaches the maximum value and starts to decline at some moment of time t_{max}. A decline indicates that the majority of carriers are already extracted from the sample. The time when the maximum current is observed depends on the mobility of the carriers. Thus, mobility can be obtained on the basis of CELIV data [67]:

$$\mu = \frac{2}{3A} \cdot \frac{D^2}{t_{max}^2}. \tag{1.9}$$

A is the speed of the voltage rise. If there are no intrinsic charge carriers in the material, they can be photogenerated and this technique is called photo-CELIV [68].

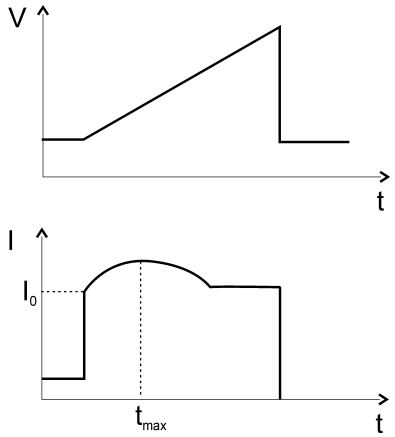

Fig. 1.4 Schematic CELIV curves of the applied voltage and the observed current.

Space charge limited current. This method relies on the following consideration. The conductive electrode attached to the organic layer, in general, can supply an infinite number of the charge carriers, electrons or holes depending on the applied bias. If the injection of the carriers does not experience a substantial energetic barrier, finally, the charge will accumulate near the interface of the electrode and the organic layer, thus, reducing the electric field and preventing injection. The amount of the injected charge is approximately equal to the charge stored on the electrodes of the capacitor-type sample. This amount of charge is transmitted through the sample over the drift time, which is proportional to the applied bias and mobility of the charge carriers. This simple picture gives the space charge limited current proportional to:

$$I_{\mathrm{SCLC}} \sim q / t_{\mathrm{d}} \sim \left(\frac{V}{D}\right) / \frac{D^2}{\mu V} = \frac{\mu V^2}{D^3}. \tag{1.10}$$

The exact solution employing the Poisson's equation, according to [69], is as follows:

$$I_{\mathrm{SCLC}} = \frac{9}{8} \frac{\varepsilon \varepsilon_0 \mu V^2}{D^3}. \tag{1.11}$$

However, one has to carefully check if the current-voltage characteristic is determined by the space charge and not by the voltage dependence of the carrier injection. This condition can be examined by varying the thickness of the sample, however, within a relatively narrow range. Besides, varying the thickness may lead to the changes of the film structure and this in turn may change the mobility [9].

Field effect transistor configuration. The organic field effect transistor (OFET) is made of organic material with two metal electrodes attached directly and the third electrode separated by a thin dielectric layer (see Fig. 1.5). If the voltage V_{g} is applied to the gate electrode, the sandwich-type structure (organic layer-insulator-gate electrode) acts like a capacitor and the corresponding amount of charge accumulates in the organic layer near the interface with an insulator. This charge will move under action of the voltage V_{sd} applied between the source and the drain at the same time. The amount of the moving charge equals to the product of the device capacitance *C* and V_{g}. It is a straightforward way to find mobility once the current and amount of moving charge are known. According to [70] the current between the source and the drain I_{sd} relates to the mobility as:

$$I_{\mathrm{sd}} = \frac{W}{L} C\left(V_g - V_t\right) \cdot V_{sd} \cdot \mu. \tag{1.12}$$

L and *W* are length and width of the channel as indicated in Fig. 5, and V_t is the value of threshold voltage required to obtain the current. Equation (1.12) is derived for a linear regime of the device when I_{sd} linearly depends on voltage between the source and the drain V_{sd}. I_{sd} relates to mobility in the saturated regime as well [71]:

$$I_{\mathrm{sd}} = \frac{W}{2L} C\left(V_g - V_t\right)^2 \cdot \mu. \tag{1.13}$$

Experimentally measured current-voltage dependences of the OFET help to determine the mobility. However, it is assumed that drain and source electrodes constitute an omic contact with the organic layer, which is not necessarily the case. In

addition, charges move in a close proximity to the organic-dielectric interface. Thus, the transport in bulk may be different [11]. It is found that mobility depends on the device geometry [71]. Therefore, the obtained mobility becomes device characteristic and not the intrinsic property of the material.

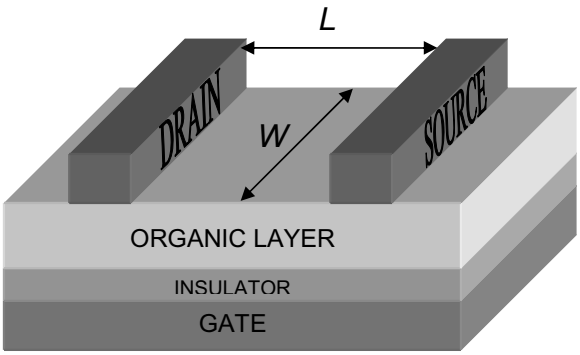

Fig. 1.5 Structure of the OFET with contacts on top.

Pulsed-radiolysis time-resolved microwave conductivity (PR-TRMC). This technique is developed in the University of Delft (Netherlands) and firstly reported in [72]. It uses absorption of microwave as a probe for the carrier mobility. Originally a nanosecond pulse of electrons from the accelerator having the energy of several MeV was used to irradiate the sample and to create charge carriers. The following change of the microwave absorption reflects the mobility of created carriers: $\Delta\sigma = e \cdot n \cdot (\mu_e + \mu_h)$. Here n is the density of carriers, μ_e and μ_h are the mobility of the electrons and holes. Thus, obtaining the mobility requires information on the carrier density, which is estimated from the absorbed energy of the electron pulse, the energy needed to create the pair of carriers and their recombination probability. The electric field strength can be tuned by changing the power of microwave radiation. It should be noted that this technique provides information about the carrier mobility within short distances down to intrachain movement. Depending on the microwave power and frequency the probed spatial range falls into the range of several nanometers. Mobility obtained at high microwave frequencies may be treated as the upper limit for macroscopic mobility [11]. The advantage of PR-TRMC is that it can be applied to bulk material as well as isolated chains of polymers in solutions. It is contactless, thus, the result is not affected by any interfacial phenomena. However,

mobility is averaged over electrons and holes. Therefore, special intentionally added traps for one sort of carriers have to be used to obtain the mobility of the other.

Terahertz spectroscopy. With the advances in generation and detection of terahertz pulses, terahertz spectroscopy became a useful tool for investigations of conductive properties of materials. Usually femtosecond pulses of the Ti:sapphire laser are used to generate terahertz pulses in a photoconductive switch or in a non-linear crystal (ZnTe for instance). Detection of the terahertz pulses after passing the sample is done in a reverse manner used to generate terahertz pulses. The amplitude and the phase of transmitted terahertz pulse are detected. Therefore, it allows obtaining the refractive index and conductivity of the investigated material within a certain range of frequency. If steady-state properties are investigated, the technique is known as terahertz time-domain spectroscopy. A sample can be excited with a femtosecond light pulse prior to the arrival of the terahertz pulse. This pump-probe experiment (time-resolved terahertz spectroscopy) enables observation of the dynamic changes of conductivity with a picosecond time resolution. In order to obtain mobility from the terahertz spectroscopy experiment one needs a complementary information concerning density of charge carriers, which has to be acquired by other methods. A detailed review on terahertz spectroscopy is given in [2].

2 Materials and experimental techniques

2.1 Investigated polymers

MeLPPP is a widely investigated polymer [23, 61, 73, 74,]. Good solubility, high fluorescence quantum yield of spin-coated films (up to 40%) [75], high carrier mobility and other properties make MeLPPP a promising candidate in electroluminescent applications [76]. Ladder type structure of MeLPPP is the most prominent feature that prevents torsional defects and facilitates charge transport. However, MeLPPP suffers from ketonic defects, which act as traps [7].

F8BT is a copolymer of 9,9-dioctylfluorene and benzothiadiazole. Conventional polyfluorenes are hole transporting materials, while electron mobility is lower by at least one order of magnitude [32]. Imbalance of electron and hole transport in the OLED device reduces the efficiency. Benzothiadiazole is electron accepting moiety, which facilitates electron transport in F8BT. It is worth mentioning that F8BT has been employed as a light-emitting layer in air-stable hybrid organic-inorganic LEDs [77] and F8BT based photovoltaic devices exhibited high efficiency [78].

PSF-BT is still a relatively new electron transporting polymer, thus, photophysical properties and device performance are to be revealed. Structures of MeLPPP, F8BT and PSF-BT are depicted in Fig. 2.1.

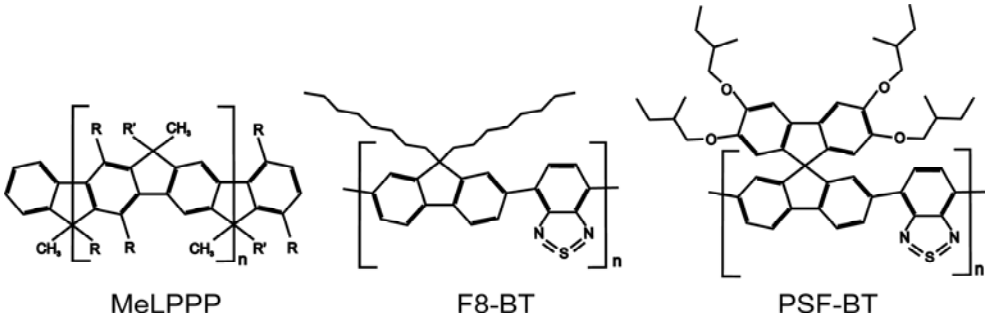

Fig. 2.1 Structural schemes of π-conjugated polymers MeLPPP, F8-BT and PSF-BT (R=alkyl, R'=aryl).

Steady-state absorption and fluorescence spectra of MeLPPP, PSF-BT and F8BT films are presented in Fig. 2.2. The maximum of absorption is around

450÷460 nm for all three materials. The emissions of F8BT and PSF-BT peak at about 540 and 570 nm, respectively. Compared with polyfluorene the absorption and emission bands of PSF-BT are shifted by about 100 nm to the long wavelength region. According to quantum chemical calculations performed in [79], the BT group included into the polymer backbone reduces the excited state energy by more than 1 eV, while the ground state energy remains almost unchanged. Similar shifts of absorption and emission bands were also found in F8BT [80, 81, 82]. The fluorescence of F8BT is slightly more structured compared with PSF-BT and less broadened. Rigidity and low diagonal disorder of MeLPPP manifest themselves spectroscopically. Small Stokes shift, sharp edges of the absorption and fluorescence bands and pronounced vibrational structure are present in MeLPPP.

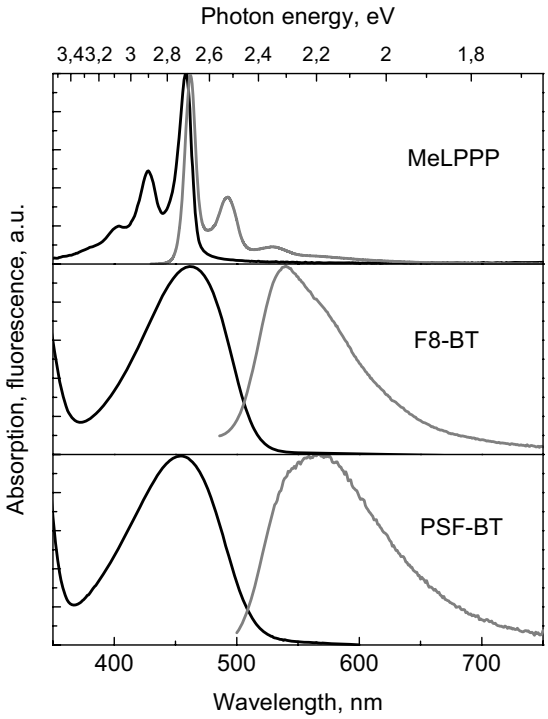

Fig. 2.2 Normalized absorption (black) and luminescence (grey) spectra of MeLPPP, F8-BT and PSF-BT films.

2.2 Samples

The polymer films of about 100 nm thickness were deposited on the indium-tin oxide (ITO) covered glass by spin coating from toluene solution, followed by the deposition of an aluminum/silver top electrode. The MeLPPP was synthesized as described in [83]. PSF-BT has been obtained from Merck KGaA (Darmstadt) and its synthesis is described in [3]. F8BT has been obtained from American Dye Source ADS, Canada. PSF-BT and F8-BT films were deposited from solutions of 10 and 20 g/L, respectively. The spin speeds were 500 rpm for PSF-BT and 2000 rpm for F8-BT. For polymer protection from the ambient the devices were capsulated by sealing a glass lid with epoxy resin in argon atmosphere. Electroluminescence of devices was observed with the naked eye at sufficiently high forward voltage despite the fact that the samples (Fig. 2.3) were not real multilayered OLEDs.

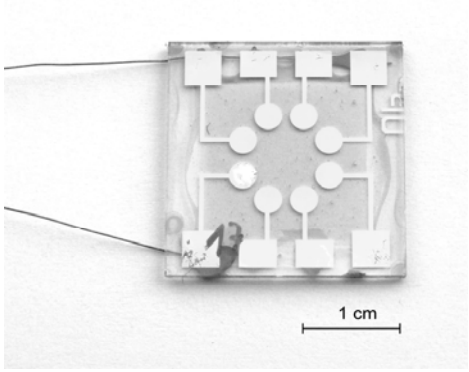

Fig. 2.3 Photography of the standard sample. Circle-shaped areas of the metal electrodes in a center constitute seven separate devices and one is used as wiring to ITO (the schematic cross-section of the device is presented in Fig. 2.7).

Fabrication of the oriented samples of F8-BT is similar except that it requires a special alignment layer (rubbed polyimide) on the top of ITO layer. Polymer chains align in parallel to the surface in one direction after annealing the sample with the alignment layer to 160°C. Fig. 2.4 shows absorbance of the oriented and non-oriented samples.

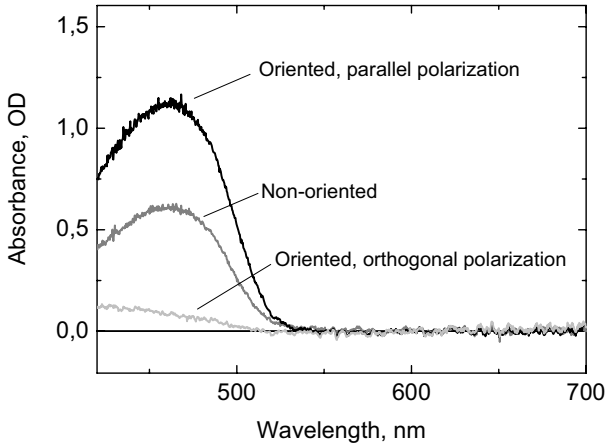

Fig. 2.4 Absorbance of the oriented F8BT sample when light is polarized parallel (black curve) and orthogonal (light grey curve) to the alignment direction. Grey curve shows absorbance of the non-oriented sample.

2.3 TREFISH technique

Briefly, the main idea of the TREFISH technique is as follows. In sandwich-type organic electronics devices an investigated functional material fills the space between electrodes forming a plate capacitor-like sample. If this capacitor is charged and material exposed to the light pulse afterwards, the drifting photogenerated charge carriers discharge the capacitor and the electric field in the material declines. If this decay is somehow recorded, estimations on the motion of photogenerated charge carriers can be made, as this motion is the primary cause of the electric field drop. One can observe the voltage (electric field) kinetics by electrical measurements. However, time resolution of electrical measurements is always limited by the time constant *RC* of the installation circuitry and does not exceed subnanoseconds in the best case. The investigated material itself can be used to measure the electric field strength optically if some of its optical properties depend on the applied field.

The TREFISH method enables measurement of the electric field strength inside the investigated materials by means of the optical second harmonic (SH) generation. It is based on a well-known electric field-induced second harmonic generation (EFISH) phenomenon, which is commonly used for the determination of the molecular hiperpolarizability [16, 17]. The second harmonic cannot be generated in amorphous and other centrosymmetric materials. The centrosymmetry is broken by

the application of an electric field. It may be considered that generation of second harmonic in the presence of static external field is the third order nonlinear process [84]. The second harmonic generation efficiency then is proportional to the hiperpolarizability of the molecules [16, 17] and to the second power of the applied field. Thus, the electric field E inside the investigated material can be monitored by measuring the second harmonic intensity I_{2H}:

$$E \sim \sqrt{I_{2H}} \quad . \tag{2.1}$$

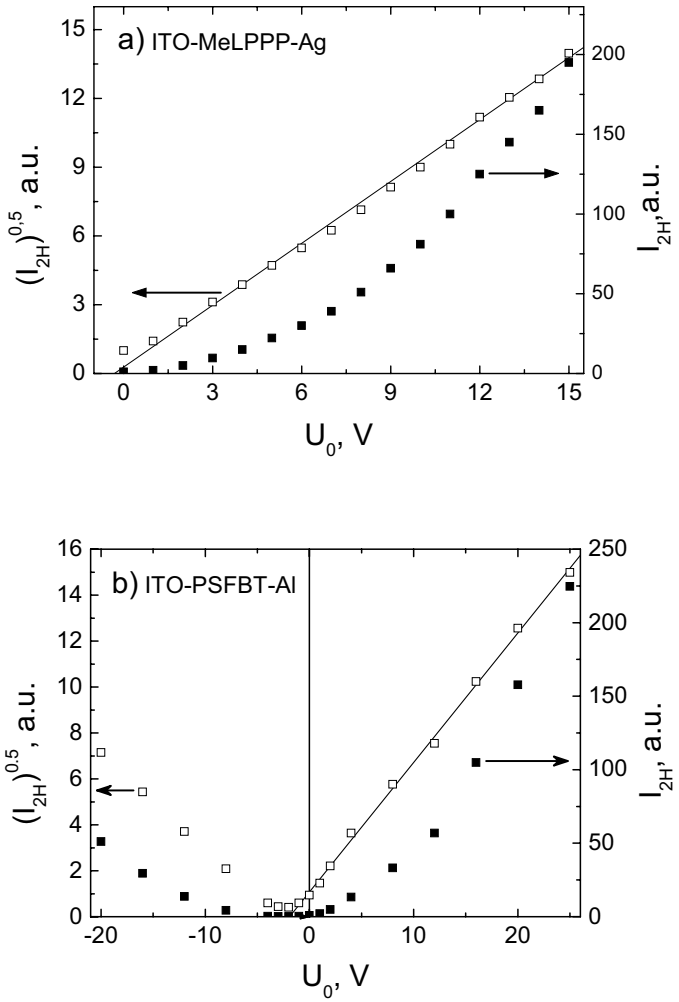

Fig. 2.5 Second harmonic intensity (■) and square root of second harmonic intensity (□) versus voltage applied to a) MeLPPP sample with silver electrode; b) PSF-BT sample with aluminum electrode. Bias voltage U_0 expresses bias applied to the metal electrode. Polymer thickness is 100 nm in both cases.

Fig. 2.5 demonstrates experimental evidence of eq. (2.1). The square root of the second harmonic intensity obeys a linear dependence on the external voltage applied to the sample. The intensity minimum shifted to the negative voltage (Fig. 2.5b) reflects the built-in electric field, arising from work function difference of the aluminum and ITO electrodes. This shift is evidently smaller for the ITO-MeLPPP-silver sandwich-type device. It may be explained by different work functions of aluminum and silver. Work function of silver depends on the crystal surface: 4,64eV for Ag(100), 4,52eV for Ag(110), 4,74 for Ag(111) and 4.3eV for polycrystalline [85]. Work function of aluminum is 4.06-4.26eV [85]. ITO work function also varies around 4.8eV depending on the surface preparation [86 and references therein]. 2H output obeys quadratic dependence on the intensity of fundamental harmonic (Fig. 2.6).

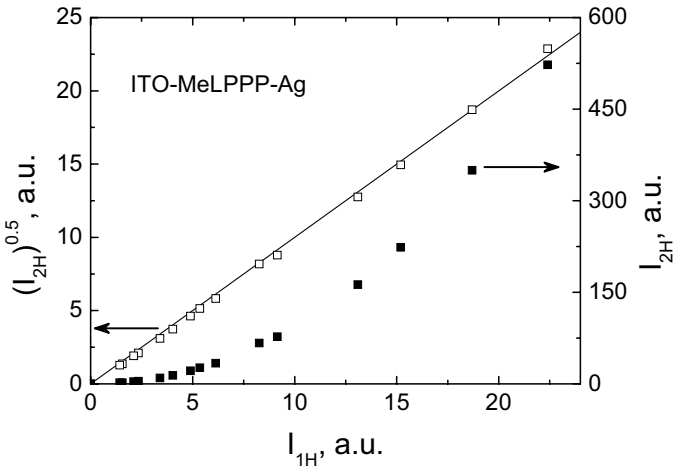

Fig. 2.6 Second harmonic intensity and square root of second harmonic intensity versus fundamental harmonic intensity acting on MeLPPP sample.

If one applies voltage U_0 to the capacitor-like sample, it becomes charged and the amount of charge is:

$$q = CU_0 = \varepsilon\varepsilon_0 \frac{A}{D} U_0; \tag{2.2}$$

where C is the sample capacitance, A is the area of electrodes and D is the distance between electrodes, *i.e.* thickness of the investigated film. The electric field assuming

homogeneous distribution inside the investigated material equals to: $E_0 = U_0 / D$. Therefore, the field and the voltage will be used as synonyms in the text. The capacitor-like sample, charged in advance by an external electric supply, is discharged by the photocurrent. Thus, the photocurrent reduces the initial electric field. The field change ΔE relates to the amount of the transported charge Δq and geometrical properties of the sample:

$$\Delta q = C \cdot D \cdot \Delta E . \tag{2.3}$$

Therefore, Δq and ΔE are equivalent quantities.

The TREFISH measurement is carried out in a pump-probe scheme. The pump pulse creates charge carriers, and the subsequent pulse probes the electric field strength in the polymer film. The electric field dynamics $\Delta E(t)$ may be obtained by changing time delay *t* between pump and probe pulses. In the case of relatively small field variations compared to E_0, the second harmonic kinetics intensity $I_{2H}(t)$ relates to $\Delta E(t)$ as:

$$\Delta E(t) \approx \left[\left(I_{2H}(t) / I_{2H}^0 \right)^{1/2} - 1 \right] E_0 . \tag{2.4}$$

I_{2H}^0 is the second harmonic intensity without excitation. If ultrashort light pulses are used for the sample excitation and for probing of the second harmonic generation efficiency, the electric field, and thus the photocurrent dynamics, may be determined with the femtosecond time resolution. The time resolution is limited by the duration of the optical pulses only, however the time domain of such measurements is limited at the most to several ns by the length of the optical delay line. The photocurrent dynamics at longer times may be obtained by the current or voltage mode TOF measurements with a typical time resolution of several ns. Thus, by combining both methods the photocurrent kinetics from the carrier photogeneration until their extraction from the sample can be determined.

A drift of photogenerated charge carriers creates the photocurrent and the field-induced polarization of photogenerated neutral excitons creates the displacement current. Therefore, the change of the electric field can be expressed as the sum of the exciton $\Delta E(t)_{\text{exc}}$ and charge carrier $\Delta E(t)_{\text{CC}}$ contributions:

$$\Delta E(t) = \Delta E_{\text{exc}}(t) + \Delta E_{\text{CC}}(t) ; \tag{2.5}$$

If the field change is small in comparison with the applied field, the exciton contribution may be approximately expressed as:

$$\Delta E_{\mathrm{exc}}(t) \approx -n_{\mathrm{exc}}(t)(\Delta\alpha)E_0 / 2\varepsilon\varepsilon_0 ; \tag{2.6}$$

$n_{exc}(t)$ is the exciton density, $\Delta\alpha$ is the change of the polarizability of the excited chain or chain segment with respect to the ground state. Excitons cause a rapid drop of the field during the excitation pulse action and the field recovers when the excitons decay. Their time-integrated contribution to the transported charge is zero. Since $\Delta E_{\mathrm{exc}}(t)$ is proportional to the exciton density, its kinetics may be obtained from time-resolved fluoresecence or transient absorption measurements (*e. g.*, see chapter 5.2). Proportionality of $\Delta E_{\mathrm{exc}}(t)$ to the applied electric field helps to determine its absolute value by measuring the electric field kinetics at different applied voltages. The exciton contribution has to be subtracted from the electric field dynamics $\Delta E(t)$ in order to obtain the charge carrier contribution $\Delta E(t)_{\mathrm{CC}}$.

The charge carrier contribution relates to photocurrent $j(t)$:

$$\Delta E(t)_{\mathrm{CC}} = \Delta q(t)_{\mathrm{CC}} / C \cdot D = \frac{1}{C \cdot D}\int_0^t j(t')dt', \tag{2.7}$$

where $\Delta q(t)_{\mathrm{CC}}$ is the amount of charge transported by the photocurrent. The $\Delta E_{\mathrm{CC}}(t)$ can also be expressed by the averaged drift distance $\langle l(t)\rangle$ and the density $n_{\mathrm{CC}}(t)$ of photogenerated charge carriers:

$$\Delta E(t)_{\mathrm{CC}} = n_{\mathrm{CC}}(t)e\langle l(t)\rangle / \varepsilon\varepsilon_0 . \tag{2.8}$$

If one seeks to obtain the carrier mobility, the current and the number of carriers have to be known. The current equals to a temporal derivative of equation (2.7). The charge carrier concentration $n(t)_{\mathrm{CC}}$ is more complex to deal with. The concentration changes due to carrier photogeneration and due to extraction from the sample. It has been shown that the majority of carriers are generated during the first picoseconds after excitation in MeLPPP and PSF-BT [61]. However, the carrier generation extends to the nanosecond time scale in PSF-BT (see chapter 4). The carrier concentration increase due to generation may be expressed as:

$$n_{\mathrm{CC}}(t) = n^0_{\mathrm{CC}} \cdot g(t) . \tag{2.9}$$

Here n_{CC}^0 is the carrier concentration at the end of generation process and $g(t)$ is the function of the carrier generation. Finding $g(t)$ is a separate task. It can be obtained from the field-modulated transient absorption data [87] or electric field-assisted fluorescence quenching measurements. In case of a thin film with low optical density, charge carriers are generated homogeneously over the film thickness. Moreover, photogeneration of charges is much faster than their extraction at the electrodes. Thus, the concentration of photogenerated charge carriers in the volume of a polymer film may be approximately written as follows:

$$n(t)_{CC} = n_{CC}^0 \cdot g(t) \cdot \left[1 - \langle l(t) \rangle / D\right]. \tag{2.10}$$

The photocurrent is proportional to the carrier concentration and to the drift speed:

$$j(t) = A \cdot e \cdot n(t)_{CC} \cdot \frac{d\langle l(t) \rangle}{dt} = A \cdot e \cdot n_{CC}^0 \cdot g(t) \cdot \left[1 - \langle l(t) \rangle / D\right] \frac{d\langle l(t) \rangle}{dt} \tag{2.11}$$

The latter equation can be solved numerically with respect to $\langle l(t) \rangle$:

$$\frac{l_{k+1} - l_k}{\Delta t} = \frac{j_k}{A e n_{CC}^0 g_k} \cdot \frac{1}{1 + l_k / D},$$

$$l_{k+1} = \left[l_k + \frac{j_k}{A e n_{CC}^0 g_k} \frac{1}{1 + l_k / D} \right] \Delta t \,. \tag{2.12}$$

where *k* numerates successive values in the data array, or analytically for the prompt carrier generation:

$$\Delta q(t)_{CC} = \int_0^t j(t')dt' = A e n_{CC}^0 [\langle l(t) \rangle - \langle l(t) \rangle^2 / 2d] \,. \tag{2.13}$$

Averaged mobility is obtained by calculating a temporal derivative of $\langle l(t) \rangle$ (eq. (2.12) or (2.13)) according to definition:

$$\mu = \frac{1}{E_0} \cdot \frac{d\langle l(t) \rangle}{dt} \,. \tag{2.14}$$

If mobility on a short time scale is the subject of interest and there is no need to account for the carrier extraction it may be calculated more straightforwardly by taking a temporal derivative of $\Delta E_{CC}(t)$:

$$\mu = \frac{j(t)}{A e E_0 n(t)_{CC}} = \frac{\varepsilon \varepsilon_0}{e E_0 n(t)_{CC}} \cdot \frac{dE(t)_{CC}}{dt} \,. \tag{2.15}$$

2.4 Experimental setup for TREFISH measurements

Fig. 2.7 shows experimental setup for TREFISH and TOF measurements. It was based on an amplified femtosecond Ti:Sapphire laser Quantronix *Integra-C* generating 130 fs duration pulses at 810 nm at the 1 kHz repetition rate. For tunable wavelength excitation the parametric generator *TOPAS C* was used. A probe beam of fundamental wavelength acted on the sample at an angle of incidence of approximately 45 degrees. It was adjusted to be *p*-polarized, because only the electric field of the *p*-polarized electromagnetic wave has a non-zero component in the direction of the applied DC electric field. The second harmonic intensity of the reflected probe beam was detected with a photo multiplying tube (PMT) blocking the fundamental and scattered excitation light by a bandpass filter. A mechanical chopper was used for modulation of the pump beam. The detected values of the second harmonic intensity obtained with an opened chopper were divided by the values obtained with a shut chopper. This ratio was recorded by the data acquisition program. In order to extend lifetime of the sample the external voltage U_0 was applied to the sample in a pulsed mode by the square pulse generator synchronized to the laser. The duration of the electric pulses was set to tens of microseconds. To avoid injection of the charge carriers, a positive bias was applied to the metal electrode (reversely biased device).

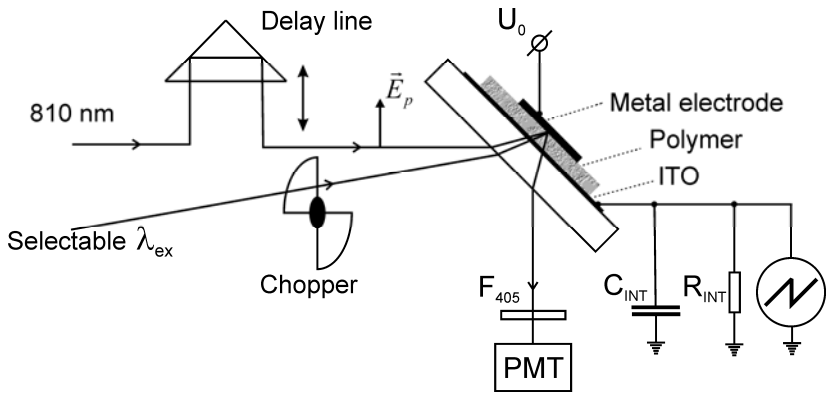

Fig. 2.7 Experimental setup for TREFISH and integral mode TOF measurement.

2.5 Computer modeling of the charge transport

The Gaussian disorder model developed by Bässler [10] was used to simulate the charge carrier transport. The model is reviewed in chapter 1.2. It relies on assumption that the carrier movement is determined by intrinsic disorder of the material. The carriers are located at particular sites in the volume. Transport proceeds via carrier hopping from site to site. Each site has intrinsic energy and the jump probabilities depend on the energies of the initial and target sites. It is considered that energies are scattered according to the Gaussian distribution. Analytical treatment of this problem is virtually impossible. Therefore, the Monte Carlo calculation algorithm is implemented. Monte Carlo algorithms require *a priori* information on the probability of any event in the investigated system. The final result is obtained by sequential calculation of event probabilities and making decision on the event, will it happen or not, according to randomly generated numbers.

The term Monte Carlo originates from Los Alamos National Laboratory (USA) [88]. Physicists being unable to get deterministic solution on neutron scattering have elaborated a calculation method which relies on repeated random sampling. As their work on the development of the nuclear weapon was secret, the code name Monte Carlo referring to the Monte Carlo Casino in Monaco was given.

The computer simulation program was developed to model the carrier transport and make comparison with experimental results. The input parameters were temperature, the applied voltage and standard deviation of site energies. The program performed the following steps: 1) generation of a cubic lattice; 2) randomly placing the carrier at some particular site; 3) simulating carrier hops from site to site until the carrier reached the lattice surface; 4) repeating steps 2 and 3 for statistics. These steps are explained further.

The lattice was generated infinite in one plane (film plane) applying periodic boundary conditions to the 128x128 lattice. The number of sites in the perpendicular direction to the film plane corresponded to the propositions about the density of conjugated segments in the modeled polymer. Indeed, it was the fourth input parameter. The site energy from a Gaussian distribution was assigned to each site. Programming languages usually have built in codes for generation of random uniformly distributed real numbers. If random numbers from normal (Gaussian)

distribution are needed, a specific algorithm has to be used. The Marsaglia polar method was employed in this work [89]. The algorithm is as follows: two independent uniformly distributed random numbers u and v $(-1 < u, v < 1)$ are generated and condition $R^2 = u^2 + v^2 < 1$ is checked. If it is satisfied, the expressions $u \cdot \sqrt{-2\ln(R^2)/R^2}$ and $v \cdot \sqrt{-2\ln(R^2)/R^2}$ give two independent normally distributed numbers, otherwise another pair of u and v is generated. Hereby, the mean is zero, and the standard deviation σ is equal to one. In order to get a demanded deviation the result was multiplied by the appropriate factor. A cubic lattice seems to be a very rough approximation for the disordered polymer film. However, it is very convenient for the computer machine and gives satisfactory results as was shown in [10].

The carrier photogeneration in polymers usually is not an instantaneous process; generation has a time span after photoexcitation [61]. In order to account for the non-instantaneous generation the program was provided with an option. The option allowed choosing carrier appearance at a random site (carrier generation) statistically compatible with the function of the carrier generation. This function for MeLPPP polymer is explored in [61].

The carrier motion was simulated by calculating probabilities for the charge carrier situated at some particular site to jump to some particular neighboring site by taking into account the electric field. The hop probabilities were calculated according to the Miller – Abraham's expression [46]:

$$\begin{cases} p_{ij} = \nu_0 & , \Delta\varepsilon_{ij} \le 0; \\ p_{ij} = \nu_0 \cdot \exp\left(-\dfrac{\Delta\varepsilon_{ij}}{kT}\right), & \Delta\varepsilon_{ij} > 0; \end{cases} \tag{2.16}$$

p_{ij} denotes probability to hop from site i to site j, $\Delta\varepsilon_{ij} = \varepsilon_j - \varepsilon_i$ is the energy difference between sites and ν_0 is the spatial overlapping factor, which, in general, may also be statistically distributed (off-diagonal disorder). Here, a few words about off-diagonal disorder have to be said. ν_0 depends on molecular orientations and overlapping of molecular wave functions on a microscopic scale. It is impossible to account for these interactions precisely. Overlapping parameter ($\nu_0 \sim \exp(-\Gamma_{ij} R_{ij})$, where R_{ij} is distance between sites i and j) taken from the Gaussian distribution seems to be zero-order approximation [10]. In [10] it is obtained in the following

way: $\Gamma_{ij} = \Gamma_i + \Gamma_j$, where Γ_j and Γ_i are numbers from Gaussian distribution assigned to sites *i* and *j*. It is arguable because it predetermines probability to hop from site *i* with the selection of Γ_i. Assignment of independent Γ_{ij} for each pair of *i* and *j* meets the difficulties in the sense of computer capability as the number of Γ_{ij} tremendously rises with an increase of the lattice size. In this elaboration the set of independent Γ_{ij} was generated dynamically with the simulation of the carrier movement. In other words: the set of Γ_{ij} was generated for the closest proximity of the carrier residing at the site *i*, Γ_{ij} values and carrier path were kept in memory. It was more convenient because the carrier visits much less sites compared to the number of sites in the whole lattice.

Each possible hop from a given site has attributed length in a random number-space proportional to the hopping probability. Subsequently, a random number picked from a uniform distribution determines the destination site. The time required for one hop was chosen from an exponential distribution according to the hopping probabilities: $t_i \sim -(\ln u)/\sum_j p_{ij}$, t_i is the time spent at the site *i* and *u* is the uniformly distributed random number from the interval (0,1). The time scale is comparative, because ν_0 in eq. (2.16) is unknown. The time scale was multiplied by the freely chosen factor in order to compare modeling with experimental results. This factor had to be the same for different sets of other input parameters (electric field, temperature).

2.6 Other experimental details

All fluorescence measurements were performed with an Edinburgh Instruments Fluorescence Spectrometer F900. For excitation a diode laser (EPL-375) emitting pulses of 50 ps duration at 375 nm wavelength with the repetition rate of 20 MHz was used. The average excitation power was about 150 μW/mm^2. The fluorescence spectra were corrected for the detector sensitivity. The time resolution of the setup is about 100 ps if deconvolution with the instrument response function is applied.

Transient absorption investigations were performed with a conventional pump-probe spectrometer based on the amplified femtosecond Ti:sapphire laser

Quantronix *Integra-C* generating 130 fs duration pulses at 810 nm central wavelength at the 1 kHz repetition rate. For tunable wavelength excitation the parametric generator *TOPAS C* was used. A white light continuum for probing differential absorption was generated by focusing the probe beam into a 2 mm thick sapphire plate. The excitation intensity was typically below 10 μJ /cm^2. In order to increase the sensitivity the pump beam was modulated by the mechanical chopper.

The electric field-modulated transient absorption has been investigated with the same pump-probe spectrometer introducing minor modifications. The modulation of the pump beam was switched off and voltage pulses were applied to the sample using a square pulse generator synchronized to the laser. The frequency of voltage pulses was set to half that of the laser, *i. e*. one laser pulse accompanied by the voltage pulse was succeeded by the other laser pulse without voltage. The data acquisition program recorded the intensities of the individual probe pulses, those with the simultaneously applied voltage and those without the applied voltage, and the difference of the optical density due to the external voltage was calculated. This arrangement enabled achieving the accuracy of 0,0001 OD (≈ 0,02%).

HOMO/LUMO levels and ionization energies and electron affinities (chapter 4.3) of the polymers were calculated from the half-wave potentials obtained by cyclic voltammetric measurements of the polymers dissolved in dry dichloromethane using $TBAPF_6$ as supporting electrolyte. These values referring to the analogues value of the redox couple ferrocene/ferrocenium ($FeCp_2/FeCp_2^+$) were converted to the absolute energy relative to the vacuum level supposing a value of -5,1 eV for the inonization energy of ferrocene. Details of the setup and conversion procedure can be found elsewhere [90]. All observed oxidation and reduction cycles were reversible.

A liquid helium cold finger cryostat (Janis CCS-100/204) has been used for measurements at different temperatures.

3 Excited state relaxation in PSF-BT

This chapter is dedicated to the investigation of excited state relaxation in PSF-BT polymer by means of time-resolved fluorescence and transient absorption techniques. The knowledge about excited state relaxation is required when generation and subsequent drift of charge carriers are considered.

3.1 Fluorescence

Figure 3.1a shows fluorescence decays of the PSF-BT film measured in different spectral positions. Amplitudes do not reflect actual fluorescence intensity at different wavelengths due to spectral dependence of the detector sensitivity. The fluorescence relaxation on the short wavelength side of the fluorescence band is slightly faster than at longer wavelengths, indicating a dynamic fluorescence band shift. The fluorescence relaxation at all detection wavelengths is clearly nonexponential. Decay curves obtained by fitting the fluorescence kinetics by three exponential functions with simultaneous deconvolution of the apparatus function (not shown) indicate that the initial relaxation time ranges from about 100 ps on the short wavelength side to about 300 ps on the long wavelength side. The relaxation rate gradually decreases in time, and the long fluorescence component may be characterized by about 50 ns relaxation time constant. It should be noted that application of the three exponential functions has no physical background, it only helps for the numerical characterization of the decay kinetics and deconvolution of the instrument response function. Fluorescence of the F8BT film decays almost exponentially with the time constant of about 900 ps.

Time resolved fluorescence spectra of the PSF-BT film were reconstructed from the kinetics measured at different probe wavelength. Figure 3.1b shows the fluorescence spectra at different delay times. For better comparison the spectra are normalized. The fluorescence band slightly broadens in time and its maximum experiences about 20 nm shift to the long wavelength side. The main spectrum modifications take place during initial several nanoseconds, *i.e.* during the initial relaxation phase.

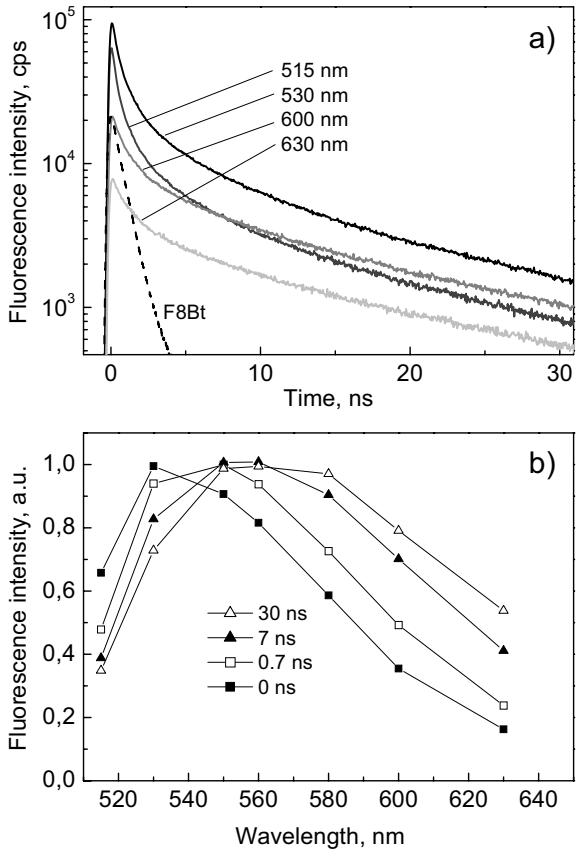

Fig. 3.1 a) Fluorescence decay of PSF-BT measured at different wavelengths. Fluorescence decay of F8BT is included for comparison (dashed curve). b) Fluorescence spectra of PSF-BT at different delay times reconstructed from time resolved kinetics.

In order to get more information about the relaxation mechanism, temperature dependences of the fluorescence kinetics were investigated. Figure 3.2 shows the fluorescence spectra obtained at different temperatures and the insert shows the temperature dependence of the fluorescence yield. Absolute fluorescence quantum yield at room temperature was measured using an integrating sphere setup with calibrated detection (Hamamatsu C5511). The yields at other temperatures were obtained comparatively to room temperature. The fluorescence yield increases from 8% at 300 K to 14% at 20 K and the fluorescence spectrum slightly narrows and shifts to the long wavelength side by cooling (see Fig. 3.2). The fluorescence yield of the F8BT film at 300 K is about 35%.

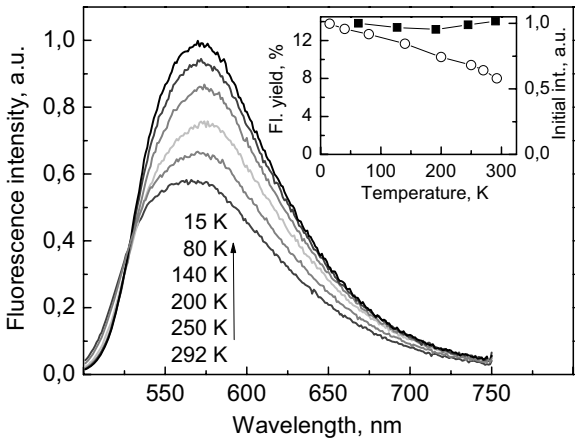

Fig. 3.2 Time-integrated fluorescence spectra of PSF-BT at different temperatures. The insert shows the temperature dependences of the fluorescence yield (○) and zero time fluorescence intensity (■).

Figure 3.3a shows the fluorescence kinetics at 575 nm measured at different temperatures and insert shows two most prominent ones on a linear scale. Fluorescence detection close to the maximum of the fluorescence band was selected in order to minimize the band shift influence. The fluorescence relaxation slows down by decreasing temperature from 292 to 80 K. The kinetics experience only weak changes below 80 K (not shown). For better representation of the temperature influence, the fluorescence decay rate was calculated as $k(t) = F^{-1}\frac{dF}{dt}$. Figure 3.3b shows the obtained time dependences of the decay rate at different temperatures. Since the differentiation procedure causes a significant increase in experimental fluctuations, curve smoothing was used prior to differentiation. In order to obtain efficient smoothing without loosing time resolution, different smoothing parameters were used for different time domains. In the case of exponential decay the decay rate should be constant in time and should be related to the decay time as $k = 1/\tau$, where τ is the fluorescence lifetime. The decay rate kinetics presented in Fig. 3.3b shows that the PSF-BT fluorescence decay is non-exponential in all time domains and at all temperatures. The decay rate decreases almost ten times during initial 10 ns and continues to decrease on a time scale of tens of nanoseconds. The temperature dependence of the decay rate is complicated. Initially the decay is about 20% faster at

room temperature than at 80 K. The difference gradually disappears, and in 2–4 ns time domain the decay rate is essentially temperature-independent. At longer delay times the temperature dependence appears again, and in time domain of tens of nanoseconds the decay at room temperature becomes about 1.5 times faster than at 80 K. The insert in Fig. 3.2 also shows the temperature dependence of the fluorescence intensity at zero time obtained after deconvolution procedure with the instrument response function. The initial intensity within experimental accuracy is constant, which indicates that the temperature dependence of the fluorescence yield results from the temperature dependent decay kinetics.

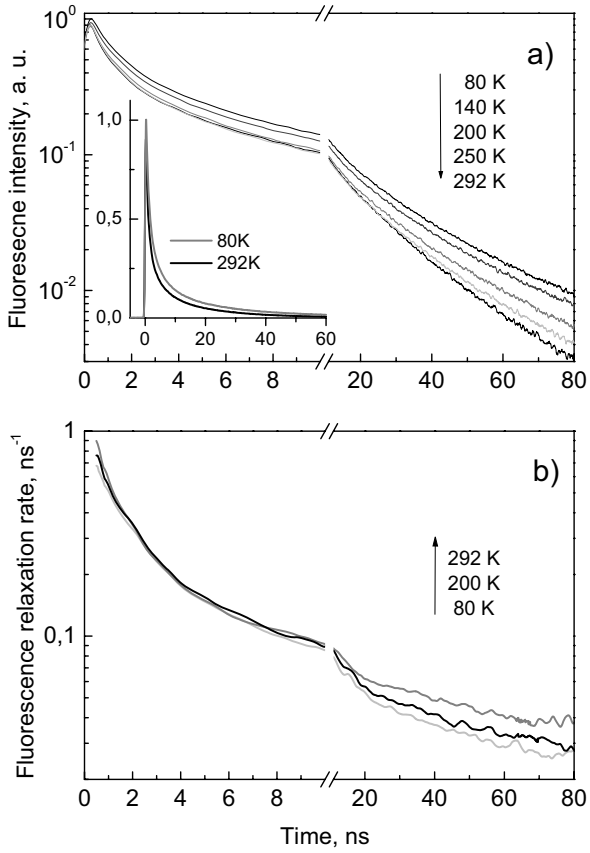

Fig. 3.3 a) Fluorescence decay kinetics of PSF-BT at 575 nm wavelength measured at different temperatures. b) Fluorescence decay rate kinetics ($k(t) = F^{-1} \cdot F'$) at different temperatures calculated from the data in a).

Let us briefly recall the mechanisms that can account for the unusually long fluorescence lifetimes and complicated kinetics observed in PSF-BT (Figs. 3.1 and 3.3). In principle, fluorescence lasting tens of nanoseconds can be due to three mechanisms: (i) triplet-triplet annihilation (TTA) as observed in polyfluorene and polyspirobifluorene [91, 92, 93], (ii) the formation of excimers or charge transfer (CT) states in bulk heterojunctions (blends) [94, 95], and (iii) excited state generation with high internal CT character [96] leading to a modified excited state relaxation mechanism [97]. First let us discuss and rule out mechanisms (i) and (ii) as explanation of the present results. Mechanism (i) relies on a high intersystem crossing yield to the triplet state to obtain high triplet densities essential for TTA. Phosphorescence in polyspirobifluorenes has been observed in [92, 93] testifying to the generation of triplets, its yield is usually low [98]. In PSF-BT phosphorescence is not observed, although weak delayed fluorescence (DF) can be observed in the microsecond time domain. The triplet density in films is, however, too low to generate such intense fluorescence on a nanoscale time scale. One has to keep in mind that it accounts for about half of the total fluorescence quantum yield. TTA is a bimolecular process, thus the DF intensity shows a quadratic dependence on the excitation intensity. The long-lived fluorescence in PSF-BT shows a linear dependence on the excitation intensity. Thus, because of these two arguments mechanism (i) is ruled out to account for the long-lived fluorescence in PSF-BT.

The mechanism (ii) of the exciton regeneration from CT state or excimers in blends of donor-acceptor-type polymers [95] cannot explain the present experimental data. This model suggests a biexponential fluorescence decay. The fast initial decay is caused by the exciton decay of the isolated polymers. In the blend this decay rate equals to the sum of the exciton decay and CT/excimer formation rates. The slow decay component is equal to the CT state decay. In PSF-BT a non-exponential decay, which strongly deviates from the biexponential function, is observed (Fig. 3.3). No clear transition from the prompt to DF is observed for both the fluorescence decay and decay rate kinetics. The second observation, inconsistent with the exciton regeneration from a CT state, is the temperature dependence of the long-lived fluorescence intensity. The long-lived fluorescence intensity increases with the sample cooling and saturates at about 80 K. The model (ii) predicts a decrease in

the fluorescence intensity at low temperatures because activation energy is required to regenerate the exciton from the lower lying CT/excimer state.

The mechanism (iii) has been proposed to account for the excited state dynamics in solutions of the *homo*-polymer polyspirobifluorene (EH-PSBF) [97]. According to this model, the initially created excited state is localized on the polymer backbone. It rapidly relaxes to an excited state delocalized over the backbone and the spirofluorene groups. This state gains some CT character and has a nonzero transition dipole moment to the ground state. Let it be called CT (charge transfer) exciton. CT character of this state is not proven yet, it will be done in the next chapter. Quantum chemical calculations have shown that despite of perpendicular orientation of the two fluorene groups (the side group and the one in the backbone) their wave functions overlap [99, 100]. Transition dipole moment is, however, much lower than that of the exciton localized on the backbone of the main chain. It has also been suggested that the transition dipole moment strongly depends on the spirobifluorene geometry and decreases during the conformational stabilization of the excited state [97]. Thus, according to this model, the fluorescence observed on a nanosecond time scale belongs to the CT exciton. The fluorescence decay is mainly caused by the decrease in the transition dipole moment in time rather than by the excited state decay to the ground state. The fluorescence kinetics in PSF-BT films on subnanosecond time scale is different from the transient absorption kinetics in the same time interval (see Fig. 3.5a). The fluorescence decays much faster. In line with (iii) this is because the decay of transient absorption reflects the relaxation of CT exciton to the ground state, while the initial fluorescence decay reflects the transformation of the exciton localized on the backbone to the exciton expanding over the spiro unit. The geometry of the spiro unit may be significantly distorted in a disordered polymer structure. This will lead to a distribution of both CT exciton energies and transition dipole moments. The states with low transition dipole moment have evidently lower energy also. Therefore, exciton localization in these states is accompanied by the fluorescence band shift as observed in PSF-BT (Fig. 3.1). The fluorescence band shift and a gradual decrease in transition dipole moment evidently reflect migration of spirobifluorene excitations and their localization at the bottom of DOS [9,94 101]. Spirobifluorene sites with the lowest CT exciton energy act as excitation traps. The temperature dependence of the fluorescence decay rate obtained during initial two nanoseconds (Fig. 3.3b)) reflects

this thermally assisted diffusion process. The thermal activation plays only a minor role in the initial diffusion process because the initial migration takes place down in energy within DOS. It is important to note that the temperature dependence completely disappears after about 2 ns (Fig. 3.3b)), while the fluorescence band shift and the decrease in the transition dipole moment still continue on a longer time scale. The temperature insensitivity of the long-time relaxation processes suggests that they are not related to exciton diffusion. It has been assumed that conformational changes in the spirobifluorene group take place in the *homo*-polymer EH-PSBF in solution after formation of the CT exciton leading to stabilization of the excited state [97]. The conformational relaxation time was found to increase from about 20 ps to more than 100 ps with increasing solvent viscosity. In the solid state these conformational changes are more hindered than in solution. Thus, in PSF-BT films conformational changes are expected to be much slower and cause fluorescence dynamics on a nanosecond time scale. Such conformational changes lead to exciton self-trapping and result in the fluorescence band shift and decrease in the transition dipole moment. The increase in the long-lived fluorescence intensity at low temperatures in PSF-BT is evidently caused by the reduced excited state quenching by quenching centers, impurities, or structural defects present in the polymer. Excitons reach these centers during the thermally activated migration. The energy disorder at 80 K significantly exceeds the thermal energy, therefore the exciton migration and quenching become inefficient and the fluorescence decay below 80 K becomes insensitive to temperature.

3.2 Transient absorption

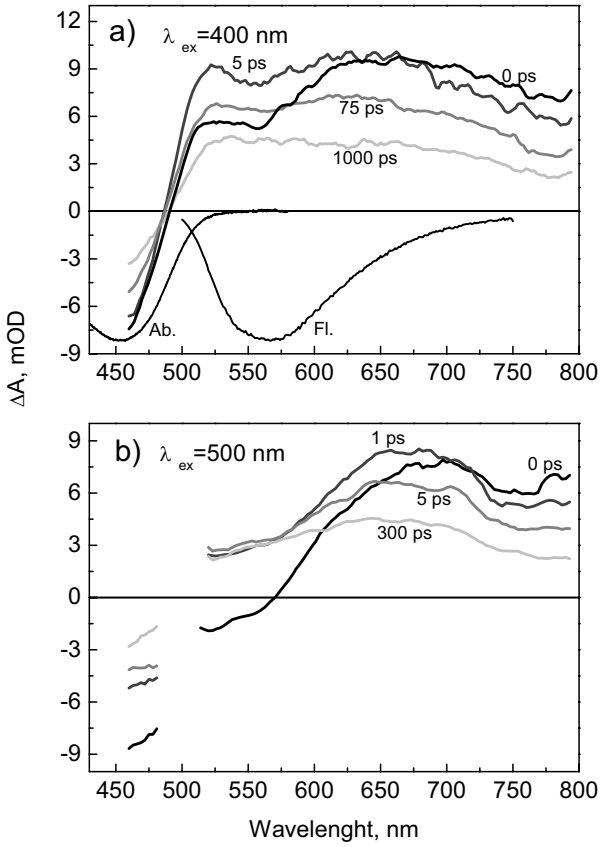

Fig. 3.4 Transient absorption spectra of PSF-BT film at different delay times measured with excitation at a) 400 nm and b) at 500 nm wavelength. The absorption and fluorescence bands (in arbitrary units) are included in a) for comparison.

Since the initial relaxation processes are not resolved in fluorescence measurements, they have been studied by means of femtosecond transient absorption spectroscopy. Figure 3.4a shows the transient absorption spectra at different delay times measured with excitation at 400 nm wavelength. The transient absorption spectra reveal absorption bleaching below 500 nm and an induced absorption at longer wavelengths. No negative transient absorption, which could be related to the stimulated emission, is present. On the other hand, the spectrum at short delay times shows a dip of induced absorption in the 500–575 nm region, where according to the zero-time fluorescence spectrum (Fig. 3.1b) the stimulated emission is expected. Thus, the stimulated emission is evidently present but it is

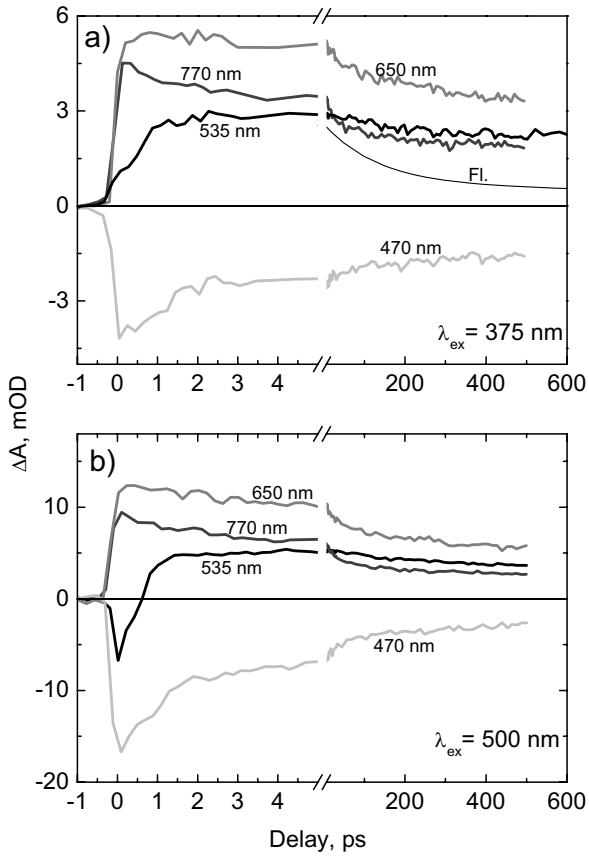

Fig. 3.5 Transient absorption kinetics of PSF-BT film at different probe wavelengths measured with excitation at a) 375 nm and b) 500 nm.

much weaker than the excited state absorption and just slightly reduces the latter. At longer delays the induced absorption in this spectral region slightly increases, and at 1000 ps this dip of induced absorption disappears. The spectra in the long wavelength region above 575 nm slightly evolve on a time scale of hundreds of picoseconds. Transient absorption spectra obtained with 500 nm excitation are slightly different. In contrast to 400 nm excitation, the negative transient absorption in the 525÷575 nm region at zero time delay is related to stimulated emission. At long delay time the spectrum becomes very similar to that obtained with 400 nm excitation. Figure 3.5 shows the transient absorption kinetics at different wavelengths obtained with excitations at 375 nm and 500 nm. Instantaneous induced absorption or absorption bleaching (470 nm) takes place at all probe wavelengths except for probe at 535 nm.

For excitation at 375 nm the induced absorption at 535 nm appears with about 1 ps delay. Similar kinetics was also obtained with excitations at 400 and 450 nm (not shown). Excitation at 500 nm initially creates stimulated emission (535 nm), which rapidly turns into induced absorption in agreement with the transient absorption spectra.

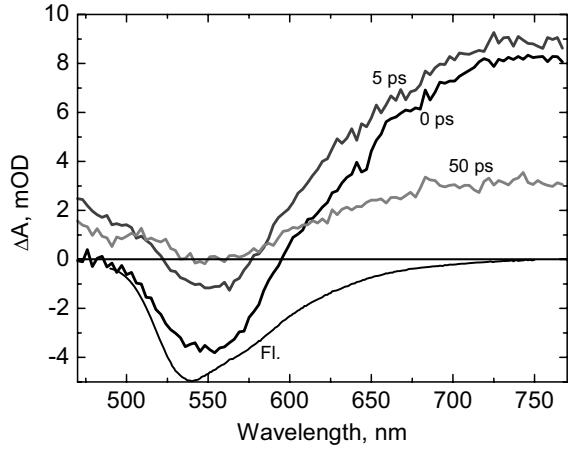

Fig. 3.6 Transient absorption spectra of F8BT at different delay times measured with excitation at 400 nm. Inverted fluorescence band is shown in arbitrary units for comparison.

The transient absorption spectra of the F8BT film (see Fig. 3.6) show the presence of stimulated emission at all delay times. The shape of the spectrum closely resembles that of the inverted fluorescence spectrum, which shows that the stimulated emission is present, but is reduced by the excited state absorption. This is also true for the 50 ps spectrum, which shows no negative transient absorption due to the compensation of stimulated emission by the excited state absorption. Thus, the stimulated emission of this polymer decays on a subnanosecond time scale in agreement with the fluorescence decay. However, the fraction of stimulated emission of the total transient absorption is small; therefore one cannot resolve the evolution of the stimulated emission spectrum and compare it with the fluorescence evolution.

Fluorene-based polymers show broad induced absorption in the visible-near IR region [96, 102 ,103, 104]. The induced absorption band in the near IR region observed in fluorene-based polymers has been assigned to absorption of singlet excitons with an additional contribution from charge carriers [102, 103]. The broad

band in the visible red spectral region has been attributed to absorption of singlet excitons [96, 102]. Gadermaier *et al.* demonstrated that singlet excitons in polyfluorene absorb in the 500-830 nm region, while a strong absorption band peaking at about 590 nm has been attributed to CT states of fluorenone [104]. King *et al*. also attributed the induced absorption in polyspirobifluorene in 500 nm to 650 nm region to the excited CT states [96].

Information from the initial transient absorption kinetics helps to elucidate the formation of the CT exciton. The short-lived stimulated emission, related to the polymer backbone excitons, decays during the transition to the CT exciton. With excitation at 450 nm and at shorter wavelength the transition to the CT exciton predominantly takes place already during the apparatus function of the setup of about 150 fs. Only the end of this process is observed as a delay in the growth of the induced absorption in the 500÷600 nm region. It is better observed with 500 nm excitation. Evidently formation of the CT exciton is slower with the excitation to the red edge of the absorption band. The wavelength dependence of the CT exciton formation rate shows that either an energetic barrier exists between the initial state and the final state, and the excess excitation energy helps the barrier crossing, or the CT exciton is formed only at some particular polymer sites, which are reached during the exciton migration to polymer segments possessing lower CT exciton energy. According to the fluorescence kinetics the CT exciton stabilization causing the decrease in the transition dipole moment continues on a nanosecond time scale. In transient absorption investigations only the initial part of this process is observed, the transient absorption at 535 nm slightly increases on a time scale of tens of picoseconds, while at other wavelengths the decrease is evident. The stimulated emission contribution almost disappears during this time. This is an indication that the CT exciton has a very low, however, nonzero transition dipole moment to the ground state. At longer times the transition dipole moment decreases even more and the stimulated emission becomes so weak that it has no influence on the transient absorption. Excited state stabilization is partly responsible for the evolution of the excited state absorption on a subnanosecond time scale. Comparison of the PSF-BT and F8BT transient absorption data shows that the spiroconjugated fluorene group in PSF-BT shortens the stimulated emission lifetime, but prolongs the excited state

lifetime. Exciton delocalization to the spiroconjugated fluorene in PSF-BT leads to formation of the long-lived excited state, thus preventing fast excited state relaxation.

3.3 Concluding remarks

The complex exciton relaxation mechanism of the *co*-polymer PSF-BT was revealed by combining nanosecond time-resolved fluorescence and femtosecond absorption pump-probe spectroscopy. Photoexcitation of the polymer to the lowest energy absorption band creates excitons on the backbone of PSF-BT. Exciton localization on the spirobifluorene takes place within 1 ps and is slightly slower with excitation to the long wavelength edge of the absorption band. This process significantly reduces the transition dipole moment to the ground state, but prolongs the excited state relaxation time to the time domain of tens of nanoseconds. Subsequent stabilization of the CT exciton taking place during several nanoseconds additionally reduces the transition dipole moment and causes faster fluorescence decay than the excited state relaxation on a time scale of tens of nanoseconds. Formation of the CT exciton several times reduces the fluorescence yield of the PSF-BT in comparison with the F8BT polymer.

4 Photogeneration of the electric charge carriers in PSF-BT

In organic materials charge carriers are not necessarily generated simultaneously with the exposure to light. Generation of charge carriers together with the excited state relaxation may extend to the nanoseconds after excitation. This should be accounted for when early stage of photogenerated charge transport is considered. This chapter deals with the charge carrier generation in PSF-BT polymer. Field-induced fluorescence quenching and electromodulated differential absorption experiments are invoked in conjunction with quantum chemical calculations.

4.1 Electric field-induced fluorescence quenching

The steady state fluorescence spectra of the PSF-BT film measured at different temperatures with and without electric field are shown in Fig. 4.1a. The fluorescence intensity increases by sample cooling from 292 K to 80 K and remains constant at lower temperatures (not shown). The applied electric field quenches the fluorescence intensity. Figure 4.1b shows the spectral dependence of the fluorescence quenching efficiency $Q = (F_0 - F_V)/F_0$ at the applied voltage of 13 V. Here F_0 and F_V are fluorescence intensities without and with an applied voltage, respectively. The quenching efficiency at room temperature is about 50 % and is slightly higher at short wavelengths. At 80 K, the quenching efficiency is close to 40 % in the short wavelength range, but only about 25% in the long wavelength range. This shows that the observed difference in the quenching efficiency by an external electric field of low energy excitons compared with that of high energy excitons is more pronounced at low temperatures than at high temperatures.

Figure 4.2 shows the time-resolved fluorescence intensities at 292 K and 80 K and an applied voltage of 0 V and 13 V measured at a wavelength close to that of the maximum of the fluorescence band (570 nm). Both common types of the fluorescence quenching, i.e. the amplitude and rate quenching, are clearly present. To allow for a quantitative comparison between both quenching types, Q obtained from time and spectrally integrated fluorescence data on the one hand and from fluorescence at zero time on the other hand are calculated and presented in Fig. 4.3. The quenching efficiency at zero time (about 0,2) representing the amplitude quenching is almost independent of temperature indicating that it is not temperature-activated in contrast

to the rate quenching. The portion of the latter, represented by the difference between the time-integrated and the zero-time quenching values, increases with temperature from 0.1 below 150 K to 0.25 at 292 K. The electric field-induced fluorescence quenching in conjugated polymers and other organic materials is routinely attributed to the charge carrier generation [9]. Fig. 4.3 also shows the temperature dependence of the time-integrated photocurrent generated by pulsed optical excitation at the applied voltage of 13 V. The photocurrent itself and its temperature dependence, resembling that of the fluorescence quenching, strongly support the conjecture that the fluorescence quenching in PSF-BT is related to the charge carrier generation. The stronger temperature dependence of the photocurrent evidently reflects the temperature activated charge transport. Some carriers remain trapped in the Coulomb potential of the counter charge or in traps (in the tail of the DOS) at low temperatures and only a fraction of them is collected.

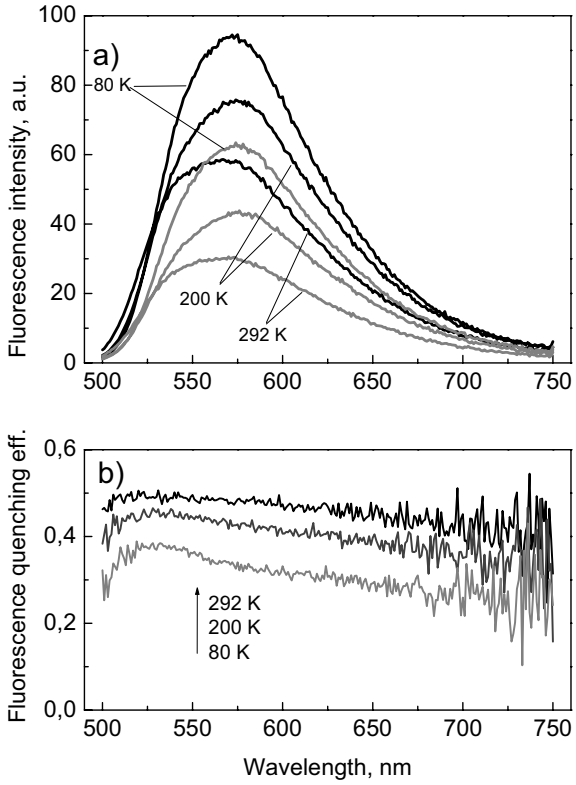

Fig. 4.1 a) Steady state fluorescence spectra of PSF-BT film without the applied voltage (black lines) and with the applied voltage of 13 V (grey lines) at different temperatures. b) Spectra of time-integrated fluorescence quenching efficiency Q measured at 13 V and varying temperatures as indicated.

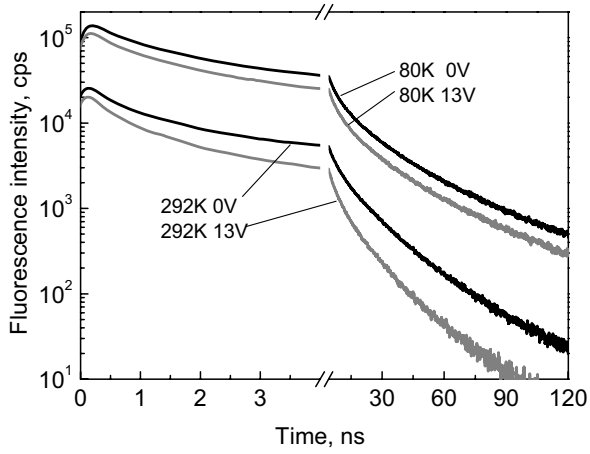

Fig. 4.2 Fluorescence kinetics without (black lines) and with the applied voltage (13 V, grey lines) measured at 80 K and 292 K. Kinetics at 292 K are vertically scaled by factor 0,2 for better presentation.

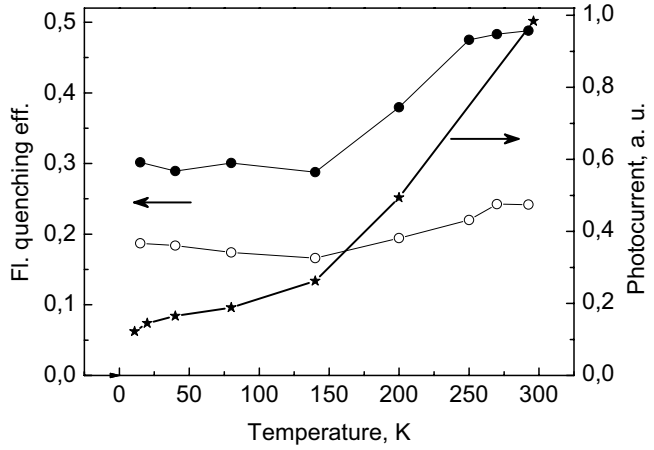

Fig. 4.3 Temperature dependences of the fluorescence quenching efficiency Q (left axis). Fluorescence quenching obtained from spectrally and time integrated fluorescence quenching (solid circles) and fluorescence quenching at zero time (open circles). The simultaneously measured photocurrent (stars) is also shown.

In order to gain more insight into the temperature dependence of the charge carrier generation process the carrier generation rate q (t,V) was calculated from the time-resolved fluorescence decays. The exciton decay kinetics with and without the electric field can be expressed from the following rate equations:

$$\frac{dn_V}{dt} = -k_R(t)n_V - k_{nR}(t)n_V - q(t,V)n_V . \quad (4.1)$$

$$\frac{dn_0}{dt} = -k_R(t)n_0 - k_{nR}(t)n_0 . \quad (4.2)$$

Here $k_R(t)$ and $k_{nR}(t)$ are radiative and non-radiative decay rates which are independent of the electric field, n_V and n_0 are the actual densities of excitons with and without the electric field, respectively. Combining eq. (4.1) and (4.2) and taking into account that the fluorescence is proportional to the product of the actual exciton density and the radiative decay rate, $F_V \sim k_R(t)n_V$, $F_0 \sim k_R(t)n_0$, yields:

$$q(t,V) = \frac{1}{F_0}\frac{dF_0}{dt} - \frac{1}{F_V}\frac{dF_V}{dt} . \quad (4.3)$$

The quenching rates at different temperatures are plotted in Fig. 4.4a. At room temperature the fluorescence quenching rate rapidly decreases within 10 ns and then remains constant but non-zero above 10 ns. At lower temperatures the initial quenching rate is almost the same as at room temperature, but it decays more rapidly and approaches zero, at least at the lowest investigated temperature of 80 K. The obtained quenching rates were used to calculate the evolution of the relative total number of quenched excitons $n_q(t)/n_0(0)$ (Fig. 4.4b) from the very beginning of the excitation ($t = 0$) up to the point t as:

$$\frac{n_q(t)}{n_0(0)} = \frac{F_0(0) - F_V(0)}{F_0(0)} + \frac{1}{F_0(0)} \cdot \int_0^t q(t')F_V(t')dt' . \quad (4.4)$$

Here the first term expresses the carrier generation related to the instantaneous (amplitude) fluorescence quenching ($t = 0$), which is beyond temporal resolution of the experimental setup. $F_V(0)$ and $F_0(0)$ are the fluorescence intensities at this point with and without the electric field, respectively. The second term expresses the amount of the subsequent carrier generation related to the rate quenching. This term is simplified by assuming the fluorescence intensity being proportional to the exciton density. This is a simplification in the case of PSF-BT due to the time dependent radiative decay rate. Therefore the calculated relative number of quenched excitons may be slightly underestimated at long times. At short times the fluorescence decays are affected by the time resolution of the measurement setup. Therefore

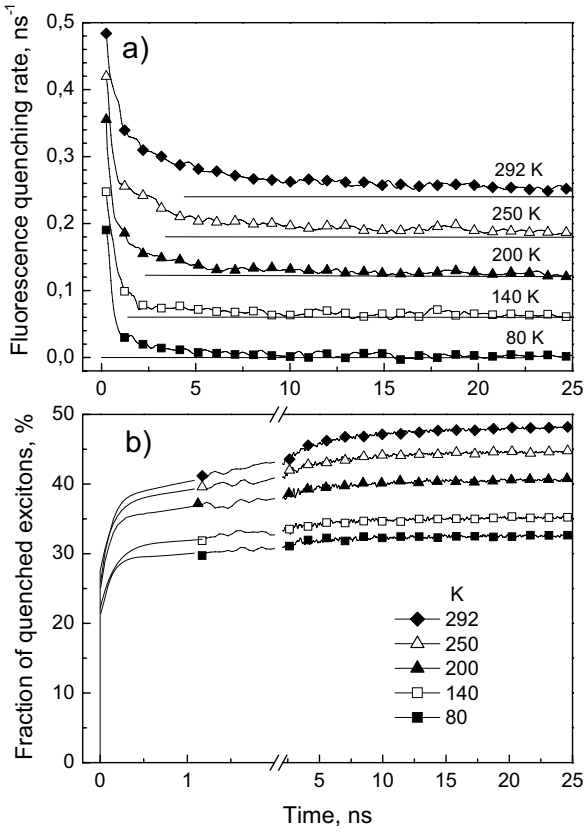

Fig. 4.4 a) Time dependences of the fluorescence quenching rate. b) Time dependence of the fraction of quenched excitons normalized to the initial exciton density. The measurement temperatures are indicated. The curves in (a) are vertically shifted, horizontal lines indicate zero values.

the initial parts of the quenching functions were calculated from the fluorescence kinetics obtained by applying a deconvolution procedure with the instrument response function. This allows a higher accuracy of calculated quenching functions. It is apparent from Figure 4.4b that the majority of excitons are quenched very fast, much faster than the time-resolution of the fluorescence setup. The quenching efficiency Q (Fig. 4.3) in this initial phase is only slightly lower at 80 K (19%) than at room temperature (25%). The next distinguishable phase of quenching proceeds dominantly on a subnanosecond time scale, but extends to several nanoseconds at high temperatures. The quenching rate during this time rapidly decreases, faster at low temperatures. About 10-12 % of excitons are quenched during this phase. The

last quenching phase lasts during the entire excited state lifetime and strongly depends on temperature; its contribution ranges from 2% at 80 K to 10 % of the overall quenched excitons at room temperature. As mentioned above, the product of quenched excitons is charge carriers. Therefore, results concerning the fluorescence quenching efficiency are directly applicable to the charge carrier generation efficiency.

4.2 Electromodulated transient absorption

Femtosecond time-resolved electromodulated differential absorption (EDA) measurements were performed to investigate the ultrafast part of the carrier generation dynamics. The wavelength and time-dependent EDA signal represents difference between the differential absorption with and without the electric field: $EDA(\lambda,t) = \Delta A(\lambda,t)^{E} - \Delta A(\lambda,t)^{E=0}$. In case of the charge carrier generation by the exciton dissociation the transient EDA signal originates from two contributions. One of them is related to reduction of exciton absorption and/or stimulated emission if the latter is observed. The other is related to increased absorption of charge carriers. However, if changes of the electric field for some reason take place, the third contribution may manifest itself, which is caused by field-dependent steady state absorption.

Fig. 4.5 shows the electromodulated differential absorption (EDA) spectra and EDA kinetics at some selected probe wavelengths. The EDA signal at all probe wavelengths except for 500 nm appears during the excitation pulse action. It has a weak rise component within 2-3 picoseconds. The EDA spectra and kinetics were identical with excitation at 375 nm and 500 nm (not shown).

Firstly, the origin of the negative strong dip at about 500 nm clearly observed in the 500 ps EDA spectrum will be discussed. The shape and spectral position of this dip are very similar to the steady state electroabsorption spectrum of PSF-BT, thus it is assigned to the dynamic Stark effect [105]. The Stark effect causes an increase in absorption intensity on the long wavelength side of the absorption band at around 500 nm with the applied voltage (Fig. 4.5a). The photocurrent created by the polymer excitation partly discharges the capacitor-like sample and reduces the electric field

inside the polymer. This leads to the attenuation of the field-induced absorption changes, which in turn are observed as a negative EDA signal.

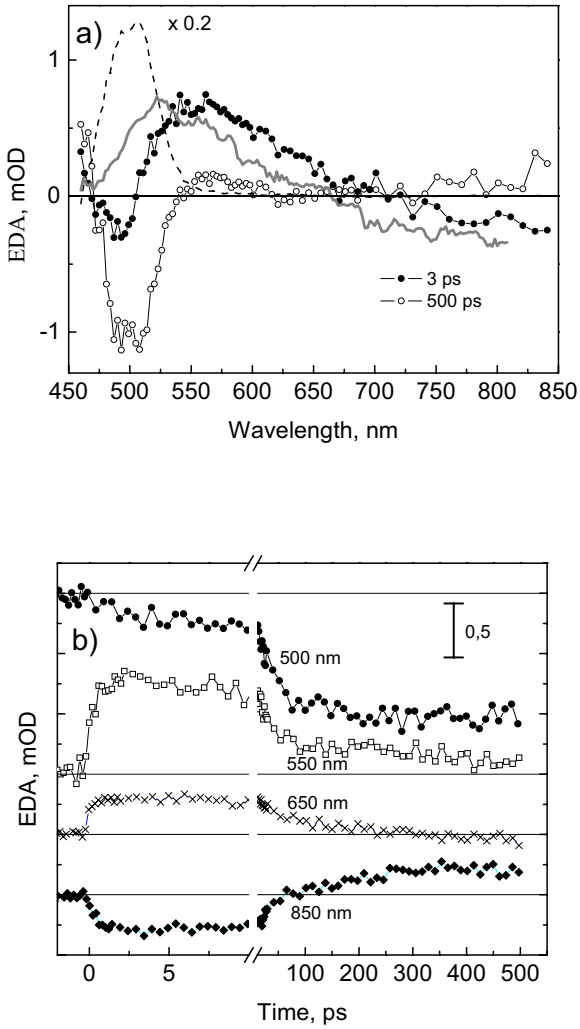

Fig. 4.5 a) Electromodulated transient differential absorption spectra at 3 ps (solid circles) and 500 ps (open circles). The solid grey line shows the difference between conventional differential absorption spectra measured at 0 ps and 5 ps delay times. The dashed line is the stationary electroabsorption spectrum, scaled by the factor 0.2. b) EDA kinetics at different probe wavelengths as indicated. Excitation wavelength was 375 nm. The kinetics are vertically shifted and the baselines are indicated by horizontal lines.

The EDA spectrum at 3 ps delay time is evidently composed of several components. In the short wavelength region, (450 -500) nm, the dynamic Stark shift dominates, which is still weaker than at 500 ps because the field attenuation increases in the course of time when created charge carriers drift and reduce the field (see for details [105]). The positive signal in the (500 – 600) nm range is caused by quenching of the stimulated emission and/or to the induced absorption of the created charge carriers. As demonstrated in chapter 3, these two effects compete in this spectral region. Thus, quenching of the stimulated emission as well as increase in the absorption of charge carriers cause an increase in the transient absorption in this spectral range. The negative signal above 700 nm is evidently caused by quenching of the CT exciton absorption when they dissociate into charge pairs. It indicates that absorption cross-sections of the CT excitons in this spectral range are slightly larger than absorption cross-sections of the created charge carriers. Hence, all these spectral changes should be assigned to quenching of the CT exciton state and to the field-assisted formation of charge carriers.

The EDA spectrum at 500 ps is dominated by the attenuation of the Stark effect. Quenching of the stimulated emission is weak at this time because stimulated emission due to its short lifetime is already absent, even without the electric field. The positive signal in the (550-625) nm region and above 700 nm should be assigned to absorption of charge carriers. The EDA signal above 700 nm changes its sign in time. This behavior is not straightforward because at both delay times (3 and 500 ps) the EDA signal is attributed to the field-assisted charge carrier generation. The explanation is as follows: both the CT excitons and charge carriers absorb above 700 nm, only the absorption cross-section of the CT exciton is larger. The applied electric field promotes formation of charge carriers, thus reducing CT exciton density. This lowers transient absorption at short time. However, CT excitons decay much faster than the carrier density. Therefore, absorbance of created charge carriers at 500 ps becomes stronger than the absorbance of CT excitons, which would remain at this time in the absence of the electric field.

Fig. 4.5a also shows that changes of the transient absorption spectrum of PSF-BT induced by the electric field are very similar to those taking place during 5 ps under field-free conditions (grey line). In other words, transient absorption spectrum with the applied field at some particular delay time is very similar to the transient

absorption spectrum without the field at later time. These changes in differential absorption were attributed to formation of CT exciton. Therefore, the EDA dynamics may be interpreted by assuming that the electric field just accelerates formation of CT excitons. To the best of author's knowledge such process has not been discussed in literature related to conjugated polymers. However, such explanation fails to explain the positive signal in the long wavelength region evident in the EDA spectrum at 500 ps, which is attributed to charge carriers. Moreover, photoconductivity shows that the charge carriers are indeed generated. The rapid dynamic Stark effect caused by photocurrent indicates that mobile charge carriers are indeed generated on a subpicosecond time scale [61]. Thus, it turns out that the electric field facilitates generation of separated mobile charge carriers. This interpretation suggests that separated charge carriers and CT exciton states have quite similar absorption spectra and these two species cannot be clearly spectrally distinguished.

4.3. Electrochemical data and quantum chemical calculations

HOMO/LUMO levels and ionization energies and electron affinities of the polymers were calculated from the half-wave potentials obtained by cyclic voltammetric measurements of the polymers dissolved in dry dichloromethane using $TBAPF_6$ as supporting electrolyte. These values refering to the analogue value of the redox couple ferrocene/ferrocenium ($FeCp_2/FeCp_2^+$) were converted to the absolute energy relative to the vacuum level supposing a value of -5,1 eV for the inonization energy of ferrocene. Details of the setup and conversion procedure can be found elsewhere [90]. All observed oxidation and reduction cycles were reversible.

Quantum chemical calculations were performed using Hyperchem® (Hypercube, Inc.). The geometry was optimized at the AM1 and PM3 level. Initially the geometry was optimized starting from a monomeric spirobifluorene-benzothiadiazol and building up the oligomer step by step up to a pentamer with an additional spirobifluorene to get two spirofluorene terminated ends. Different starting geometries were tested by varying the torsion angle between the fluorene and benzothiadiazol subunits. For simplification of calculations the alkoxy and alkyl side chains at the spirounit were mimicked by methoxy and methyl groups, respectively. The effect by extending the side chains was expected to be negligible. The energy and extension of the unoccupied and occupied orbitals were calculated at AM1 and

ZINDO/S level taking into account configuration interaction of an appropriate number of orbitals. The most important features of the oligomers do not noticeably change going from the trimer to the pentamer

Table 4.1 summarizes electrochemical data for PSF-BT and F8BT. F8BT serves as a reference compound since it has an identical backbone as PSF-BT, but possesses no fluorene side group. Literature data for F8BT are listed as well [106, 107]. The reduction potential of PSF-BT at -1,8 V vs. Fc/Fc+ is more or less unchanged compared with that of F8BT. Since the transferred electron is strongly localized on the BT unit, this is expected. Contrarily, PSF-BT has an additional oxidation wave at 0,38 V compared with F8BT. This oxidation potential is due to oxidation (abstraction of an electron) of the alkoxy substituted fluorene side group in PSF-BT. The second oxidation at 0,85 V is due to backbone oxidation at a similar potential compared with F8BT [106, 107] or PFO [107]. HOMO/LUMO energies calculated from the electrochemical data are listed in Table 4.1. The procedure described in [90] was used to calculate the energies from the redox potentials.

Table 1 Half-wave potentials and fluorescence quantum yield (PLQY) of F8BT and PSF-BT in solutions. The electrochemical data were obtained in dry oxygen-free dichloromethane.

Material	$E_{red}^{1/2}$ **[V]**	$E_{ox1}^{1/2}$ **[V]**	$E_{ox2}^{1/2}$ **[V]**	**LUMO [eV]**	**HOMO [eV]**
F8BT	-1,8	1,1	-	-3,1 (3,3[a]; 3,1[b])	-5,9 (5,9 [a,b])
PSF-BT	-1,89	0,38	0,85	-3,2	-5,48;-5,95

Solvent (ET_{30} polarity / kcal/mol)[c]	**F8BT PLQY (%)**	**PSF-BT PLQY (%)**
Xylene (33,1)	87,5	88,9
Toluene (33,9)	90,4	65,9
Methyl-tetrahydrofurane MTHF (35,1)	95,9	0,7
Dioxane (36)	-	8,9
Tetrahydrofurane THF (37,4)	97,1	0,2
Chlorobenzene (37,5)	76,2	2,9
o-Dichlorobenzene (38)	68,8	0,6
1,1,2-Tri-chloroethane (40,3)	75,3	0,1
Dichloromethane (40,7)	83,3	0,5

a: values in parentheses are taken from [106]

b: values in parentheses are taken from [107]

c: the higher the ET_{30} value, the higher the polarity (see [108])

Semi-empirical quantum chemical methods were used to calculate HOMO/LUMO orbitals and to support experimental data. Fig. 4.6 presents calculations of HOMO/LUMO orbitals of a PSF-BT oligomer. For clarity, only data for the oligomer containing three BT units are presented. There are only negligible quantitative changes upon increasing the oligomer length to five BT units. The LUMO of PSF-BT is localized on the BT unit in accord with earlier results [79]. However, the HOMO of PSF-BT is not localized along the backbone as in F8BT but on the fluorene side group carrying four *methoxy* groups. The four molecular orbitals of the PSF-BT trimer (HOMO, HOMO-1, HOMO-2 and HOMO-3) are almost iso-energetic with energy differences of 50 meV in total. The orbitals differ with respect to the methoxy substituted side-unit on which they are localized, therefore only one of them is shown. The HOMO-4 is delocalized along the backbone with a 340 meV lower energy compared with the HOMO. The findings are in accord with electrochemical data. The electron donating methoxy groups lower the oxidation potential by about 0,5 V, thus the fluorene side group HOMO is above the HOMO-4 delocalized along the backbone.

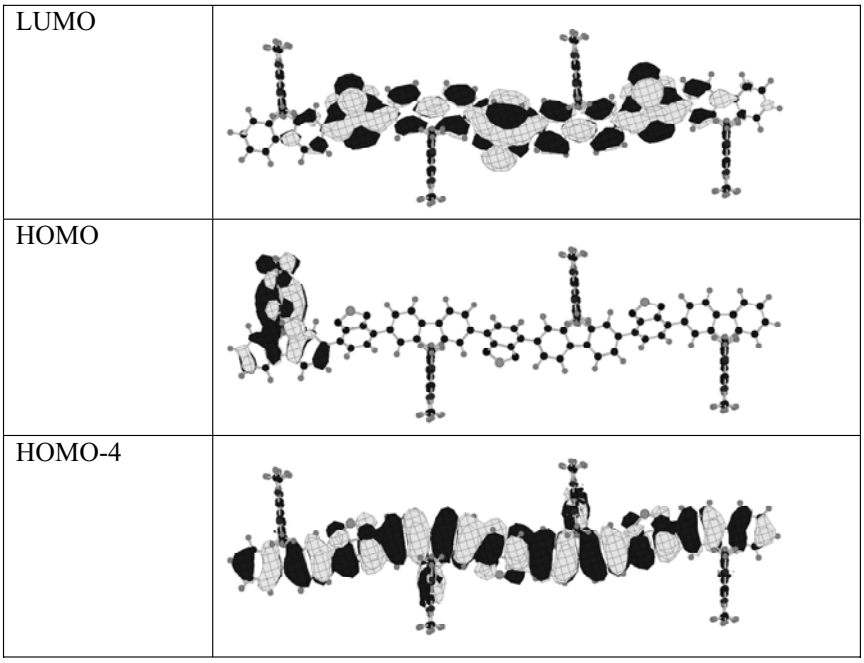

Fig. 4.6 LUMO, HOMO and HOMO-4 of a PSF-BT oligomer with methoxy-side groups. The HOMO-1 to HOMO-3 are localized as HOMO on the methoxy substituted fluorene side groups and are not shown.

Calculated electronic orbitals clearly demonstrate electronic structures of the photoactive singlet exciton and the CT exciton. Wave functions of the electron and hole are located on a backbone in the singlet exciton state, while in CT exciton state they are significantly spatially separated resulting in a very low transition dipole moment.

Quantum chemical calculations also suggest that electronic structures of the charge pair state and of the CT exciton should be very similar, only negative and positive charges are located on a more distant backbone fragment and fluorene side group in the charge pair state. This explains similarity of the charge carrier and CT exciton absorption spectra concluded from the EDA spectra.

Calculations of PSF-BT with *methyl* instead of *methoxy* side chain are in accord with literature data on similar model compounds [106] and F8BT [107] and are therefore not shown. They show delocalization of the HOMO within a few repeat units along the backbone and localization of the LUMO on the BT unit.

4.4 Carrier generation model

Based on experimental data one can distinguish three charge carrier generation phases: i) the initial ultrafast phase, ii) the subnanosecond phase and iii) the entire lifetime component. They will be shortly discussed.

(i) A significant fraction of mobile charge carriers is created instantaneously or almost instantaneously. The first ultrafast phase takes place predominantly during the excitation pulse of about 150 fs and continues for about 2 ps, as follows from EDA kinetics. This phase is almost insensitive to temperature and contributes more than 50 % to the total carrier yield.

Ultrafast charge carrier separation has been observed in various photoconducting conjugated polymers [109, 110, 111, 112, 113, 114, 115] including polyfluorene-based ones [103, 116, 117]. Since the energy of the charge pair is usually higher than that of the S_1 states, generally carrier generation is possible only before relaxation of high energy states, which usually takes place on a subpicosecond time scale and limits the carrier generation time. The ultrafast carrier generation process was considered as an auto-ionization of an excited state having sufficient energy [118]. Arkhipov *et al.* developed a theoretical framework taking into account the vibrational heat energy to assist charge carriers to escape from the Coulomb

potential. The model was successful to explain the often observed weak temperature dependence of charge generation in polymers [119].

It has also been demonstrated that high electronic states are often involved in generation of free charge carriers [120, 121, 122]. Based on this concept ultrafast carrier generation was explained as a consequence of polymer excitation to high energy excited states by sequential absorption of two photons during a single excitation pulse or by exciton-exciton annihilation [103, 109, 112, 117].

Charge carrier generation in PSBF [96] was found to last slightly longer; the EDA signal appeared gradually on a time scale of 10 ps. Carrier generation in PFO was found to take place both from singlet excitons and highly excited singlet states, the two mechanisms possessing different field and temperature dependences [123].

Electronic state properties as obtained from quantum chemical calculations suggest a quite natural explanation of the ultrafast initial carrier generation phase in PSF-BT. In contrast to other conjugated polymers, CT excitons in PSF-BT have a lower energy than the optically active singlet excitons. Therefore, the singlet exciton relaxes to the CT exciton during several picoseconds and the fluorescence dominantly originates from the CT exciton. This statement is supported by the fluorescence quantum yield measurements. Fluorescence yield of F8BT only weakly depends on solvent, while fluorescence of PSF-BT is quenched essentially to zero (Table 4.1) as soon as the solvent has a higher polarity than toluene or xylene, as expected for a CT exciton. The transition from solution to solid state should have the same effect since the polymer chains have high polarizability. In accordance with this notion the quantum yield in the solid state compared with solution is reduced by a factor of 2 for F8BT, but by an order of magnitude for PSF-BT. With the applied electric field, charge carrier generation competes with the CT exciton formation. EDA data suggest that charge carriers may be efficiently generated only before CT exciton is formed, *i.e.* when hole is still delocalized on a polymer backbone in HOMO-4 (Figure 4.6). Carrier generation during this phase is independent or only weakly depends on temperature and excitation wavelength indicating that energy of the generated charge pair only slightly exceeds the CT exciton energy. Charge carrier generation becomes more difficult after formation of the CT exciton when holes localize on fluorene side groups and become less mobile.

(ii) The subnanosecond carrier generation phase has not been observed before in any fluorene based polymers. However, carrier generation lasting during the entire excited state lifetime was observed in some other conjugated polymers [61, 124, 125]. A usually observed rapidly decreasing exciton splitting rate has been attributed to the interplay between dissociation and spectral relaxation of excitons within an inhomogeneously broadened density of states [124, 126, 127]. Localization of excitons at low energy sites reduces their mobility and reduces their probability to reach charge separation centers. The time dependent fluorescence quenching rate in PFS-BT at room temperature (Figure 4.4a) is quite similar to the fluorescence band shift dynamics presented in the previous chapter. It was also attributed to exciton relaxation within the density of states during their migration. Thus, the quenching rate dynamics is caused by a decreasing exciton migration rate with time. CT exciton evidently cannot be split in a perfect isolated polymer chain due to the high Coulomb binding energy. Therefore, charge acceptors such as impurities, structural defects or acceptors on neighboring chains are necessary for carrier generation. As Fig. 4.4a shows, the exciton splitting rate at the beginning of the second phase (the intial quenching rate value) only weakly depends on temperature. This is because initially the exciton migration is dominated by down-energy jumps. The exciton splitting rate more rapidly decreases at low temperatures and the second generation phase lasts shorter; excitons at low temperatures are more rapidly localized.

(iii) Carrier generation during the last, strongly temperature-dependent phase evidently occurs by the same mechanism as during the subnanosecond phase – generation on acceptors. Only the exciton migration at long times is temperature-activated. Excitons at low temperatures become localized and cannot reach charge separation centers. This temperature dependence is in agreement with the Monte Carlo simulations of the exciton migration process in the PPV polymer performed by Scheidler et al. [128] where they showed that initial phase of the exciton migration and quenching is temperature-independent, while after the spectral relaxation when excitons are localized in low energy states the thermal activation becomes important. The spectral dependence of the fluorescence quenching efficiency (Fig. 4.1b) supports the exciton migration based dissociation model; high energy excitons responsible for the short wavelength fluorescence band edge are more mobile and have higher probability to reach dissociation centers.

BT and fluorene side groups influence the charge carrier generation differently. The BT group has a low LUMO level and is often used to shift the fluorescence spectrum of copolymers to the long wavelength side [3]. According to the quantum chemical calculation results, electronic properties of the PSF-BT are caused by combination of alkoxy substituted side chain fluorene and BT. They cause formation of the long-lived CT exciton state with the efficient charge separation, characterized by weak fluorescence and absorption signatures similar to those of charge carriers. Comparing transient absorption data of PSF-BT with analogous data for PSBF [96] possessing no BT group, one does not observe a qualitative difference. Both of them possess wide induced absorption spectra with weakly expressed absorption bands in the green-yellow and red spectral regions. Contrarily, polyfluorenes without conjugated fluorene side group have no green-yellow induced absorption band independently of the presence of BT group [96]. Hence, the BT group has no significant influence on the induced absorption spectra of polyfluorenes, although it slightly localizes an electron in the excited state.

The role of the fluorene (with alkoxy side chains) side group is apparent. It has almost no influence on the main absorption band (~ 450 nm). Its absorption is at around 350 nm due to its high LUMO level. The presence of the fluorene side group changes the field-free excited state dynamics dramatically. The fluorene side group is responsible for the CT exciton formation and the green-yellow induced absorption band. It donates an electron to the polymer backbone in the excited state. One may also expect an easier charge carrier generation from the CT exciton state with partly separated charges. On the contrary, the charge separation rate decreases after CT exciton formation. Thus, there are no indications that the fluorene side groups facilitate the charge carrier generation; they probably make the carrier generation even less efficient, because of the hole localization.

In conclusion, the following model of the excited state relaxation and charge carrier generation in PSF-BT is proposed and sketched in Fig. 4.7. The polymer absorption is determined by the optical transition between the HOMO-4 occupied orbital delocalized on the polymer backbone. This is identical to the HOMO of F8BT or PSF-BT with alkyl side chains. The LUMO orbital is predominantly localized on BT in both polymers. The HOMO orbital of PSF-BT is localized on a conjugated fluorene side group and is strongly spatially separated from the LUMO orbital.

Therefore, the optical transition between these states has a very low transition dipole moment and the presence of the fluorene side group has no influence on the main absorption band. Stimulated emission is a peculiar feature of the initially excited state. Hole transfer from the depleted backbone HOMO-4 orbital to the HOMO orbital takes place during less than 1 ps, and CT exciton with electron density localized on BT unit and hole localized on conjugated fluorene forms. The CT exciton preserves some transition dipole moment to the ground state, thus causing weak fluorescence and weak stimulated emission of this state. Subsequent trapping at low energy sites and/or lattice relaxation during about 1 ns stabilizes the CT exciton and even more reduces the transition dipole moment and prolongs the lifetime of CT exciton.

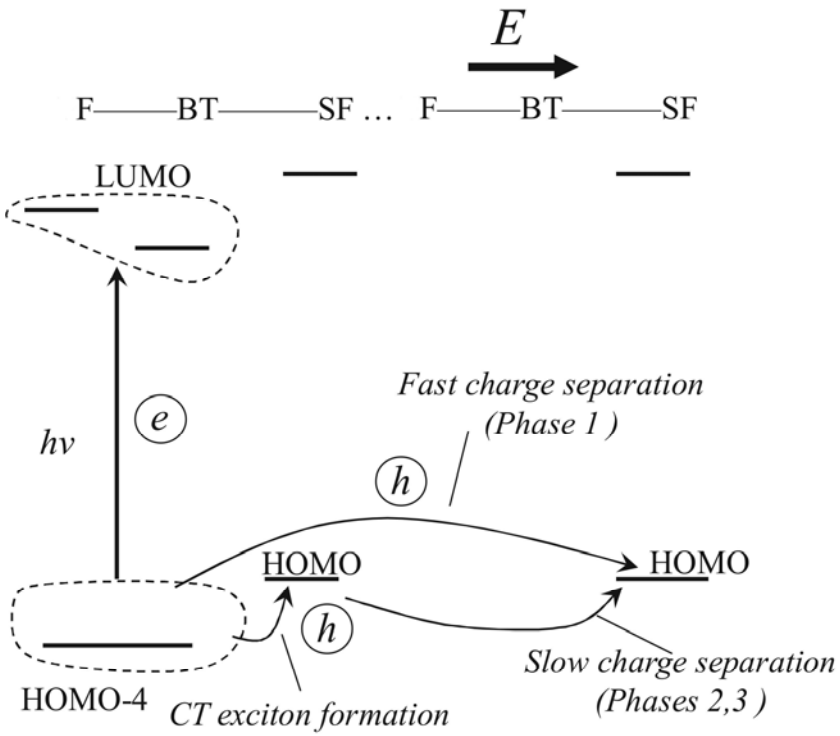

Fig. 4.7 Sketch of the charge carrier generation processes in PSF-BT. F is fluorene in the backbone, SF is the alkoxy substituted fluorene and BT is benzothiadiazole. The excitation is indicated by $h\nu$ corresponding to transfer of electron density (e) to the LUMO. (h) refers to transfer of positive charge density (hole) or more precisely – the lack of electron density.

The applied external electric field during the lifetime of the initially photoexcited singlet exciton facilitates a hole transfer from the depleted delocalized

backbone orbital to the HOMO orbital on a more distant side group. A pair of separated charge carriers may be created. This process causes the ultrafast charge carrier generation phase and amplitude-type fluorescence quenching. The carrier generation process becomes less efficient but still possible when the localized CT exciton is created. This process causes the rate-type fluorescence quenching by carrier separation at dissociation centers. CT exciton trapping on a subnanosecond time scale reduces the CT exciton migration rate, and their approaching to the dissociation centers becomes possible only by thermally assisted migration.

4.5 Concluding remarks

Formation of CT excitons and charge pair states in copolymer PSF-BT has been investigated by using the electric field-induced fluorescence quenching and transient absorption modulation. Quantum chemical calculations disclosed shapes of electronic orbitals and energies of electronic states. Common action of fluorene side group and BT facilitates rapid formation (during several ps) of the CT exciton with a small optical transition dipole moment and weakly overlapping hole and electron wave functions localized on fluorene side group and BT unit, respectively. The electric field applied before CT exciton formation efficiently splits optically created singlet excitons into charge pairs, and this process is independent of temperature. After the CT exciton formation, the charge pair generation rate significantly drops down; dissociation of localized CT exciton is evidently less efficient than dissociation of the delocalized singlet exciton. The dissociation rate continues to decrease on a subnanosecond time scale, faster at low temperatures. This decrease is related to the exciton trapping at low energy sites, which reduces the exciton mobility and their probability to reach charge carrier generation centers. The last thermally activated charge carrier generation phase continues on a nanosecond time scale and its rate strongly depends on temperature being almost zero at 80 K.

Another implication of presented results concerns the design of donor materials for solar cell applications. Care has to be taken to avoid chemical subunits that lead to formation of low energy CT exciton along a chain.

5 Mobility dynamics

Investigation of charge transport dynamics in MeLPPP and PSF-BT polymers by means of TREFISH method is presented in this chapter.

5.1 MeLPPP polymer

Fig. 5.1 shows raw data obtained by TREFISH technique for MeLPPP sample at different values of the applied external voltage. Curves represent the second harmonic intensity as a function of time delay between pump and probe pulses normalized to the second harmonic intensity without a pump pulse. Thus, the ratio equals to one at negative delays when the probe pulse arrives prior to the excitation pulse. The kinetics strongly depend on the applied voltage, which shows that several processes contribute to the second harmonic dynamics. At 4V there is an instantaneous (pulse width limited) drop of the second harmonic intensity during the sample excitation. After a few hundreds of picoseconds the second harmonic intensity almost recovers close to its initial value. At higher voltages the recovery is not complete. Increase of the applied voltage causes decay of the second harmonic intensity on a nanosecond time scale. At 20V (close to the limit the sample can stand) the recovery vanishes, after a fast initial drop the second harmonic intensity continues to decay at longer delay times.

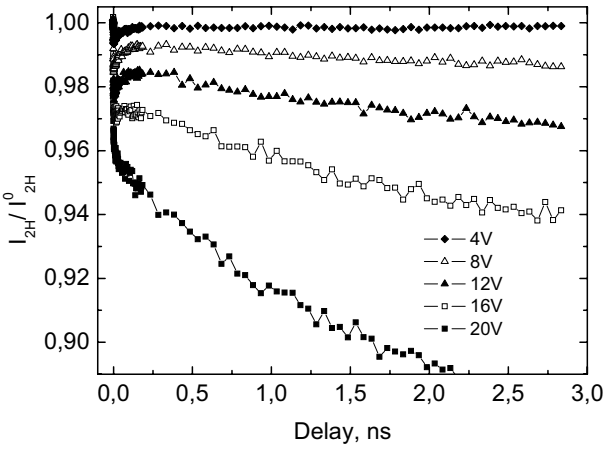

Fig. 5.1 Second harmonic kinetics in MeLPPP sample at different applied voltages. Excitation intensity is below 10 $\mu W/cm^2$, wavelength – 460 nm.

If properties of the charge carrier transport are the subject of interest, the second harmonic data have to be processed. Fig. 5.2 presents the electric field dynamics calculated from the second harmonic data using eq. (2.4). Application of eq. (2.4) is square root transform, therefore the same features remain as in Fig. 1. At low applied voltages there is a pulse width limited drop of the electric field which recovers within a few hundreds of picoseconds. After recovery of the field it starts to decay again on a nanosecond time scale at higher voltage. The field recovery eventually vanishes at the highest applied voltage and there is a continuous decrease of the electric field.

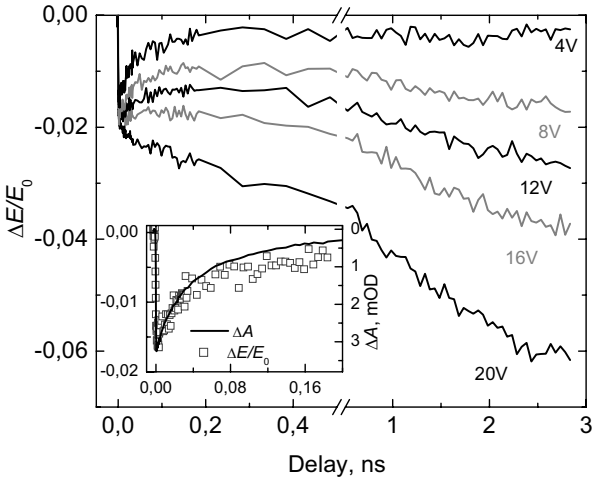

Fig. 5.2 Electric field dynamics obtained from the second harmonic kinetics presented in Fig. 5.1. Insert compares the electric filed and transient absorption kinetics at 810 nm (460 nm excitation) and 4V of the applied voltage.

Transient absorbtion kinetics at 810 nm, which were measured simultaneously with the 2H intensity, show the pulse width limited rise of the sample absorption at zero delay time and a successive decay of this excitation induced absorption with a characteristic time constant of several tens of picoseconds. The transient absorption kinetics is similar to that obtained in previous investigations and attributed to the exciton density relaxation. It has been shown in [87] that transient absorption of the MeLPPP polymer in the near IR region is mainly caused by excitons. The kinetics shows weak dependence on the applied electric field and its shape is very similar to 2H kinetics measured at low applied voltages. Insert in Fig. 5.2 shows comparison between the field kinetic measured at 4V of applied voltage

and transient absorption kinetics measured at 810 nm wavelength. It is obvious they are very akin.

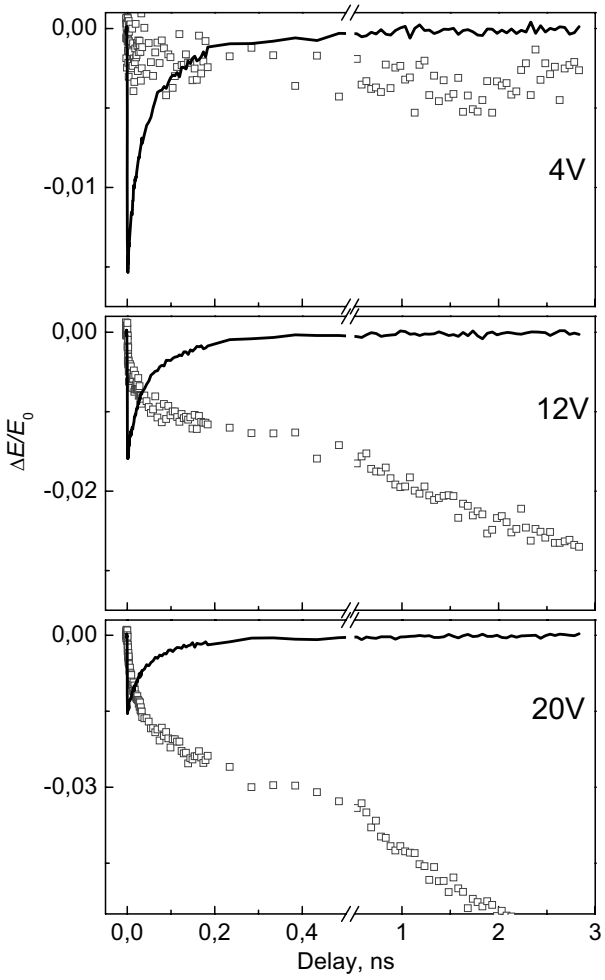

Fig. 5.3 Exciton (line) and charge carrier (data points) contributions to the electric field change at 4V, 12V and 20V of the applied voltage.

Indeed, transient absorption relaxing on a time scale of tens of ps is typical of the exciton dynamics in MeLPPP [73, 120]. Therefore, the field dynamics at low voltages should be assigned to the exciton contribution expressed by the first term in eq. (2.5). According to equation (2.6) the exciton contribution linearly depends on the applied field. Thus, at higher voltages the exciton contribution should scale linearly with the applied voltage. Field kinetics can be decomposed into the exciton and charge carrier contributions as shown in Fig. 5.3. At weak field the exciton contribution dominates

on a picosecond time scale. By increasing the applied field strength, the charge carrier contribution becomes important and at high voltages - dominating. It should be noted that the transient absorption at 810 nm changes by less than 20 % by increasing applied voltages, and shows that the field-induced exciton quenching is not very strong. The exciton contribution to the electric field dynamics decays during a few hundreds of picoseconds, while the charge carrier contribution increases with time.

Charge transported by photocurrent $\Delta q(t)_{CC}$ can be calculated from the charge carrier contribution to the electric field (eq. (2.7)). The same information about the integrated current only on a longer time scale was also obtained from the TOF measurements. Fig. 5.4 represents experimental data obtained from both TREFISH and integral mode TOF measurements – transported charge (integrated photocurrent) as a function of time. TREFISH data end at 3 ns, which is the end of optical delay stage. TOF data are shown starting with 4 ns, because 4 ns is an approximate time resolution of TOF setup. Curves reach plateau at tens of nanoseconds. Evidently, all photogenerated charge carriers are extracted up to this time. The value of the transported charge strongly depends on the applied voltage. This is because the carrier generation depends on the electric field. The electric field assists in the separation of geminate charge pairs and creation of free charge carriers [9]. Thus, more charge is extracted at the higher voltage.

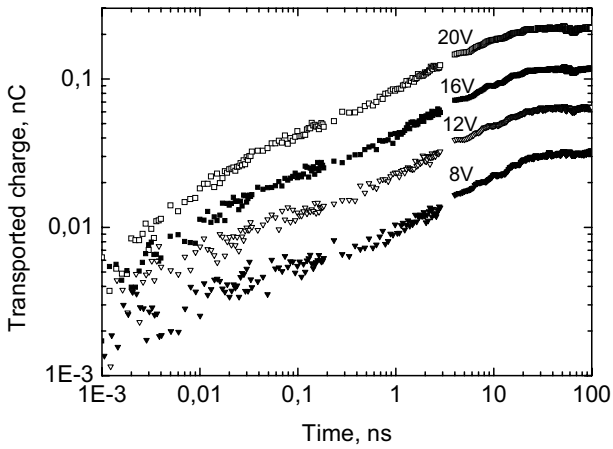

Fig. 5.4 Charge transported by photocurrent versus time-span after a pump pulse at different applied voltages. TREFISH data (from 0 to 3 ns) are combined with TOF data (from 4ns to 100 ns).

Mobility dynamics has been calculated from data presented in Fig. 5.4 employing eq. (2.13), (2.14) and using $g(t)$ from [61]. The carrier concentration at the end of generation process n_{cc}^{0} needed for mobility calculation was estimated from the integral mode TOF signal at long times. If all generated charge is extracted, one can evaluate the amount of generated charge from TOF signal. Results are presented in Fig. 5.5. The mobility dynamics can be separated into two time domains with a different curve slope. During the first time domain ending at approximately 100 ps the mobility changes approximately as $\sim t^{-1.5}$. Later a weakly time dependent mobility is observed. The initial mobility phase evidently corresponds to the non-stationary carrier transport. Likely carrier motion inside a single polymer chain or a single conjugated segment is dominant in this phase. The time interval from a nanosecond to tens of nanoseconds corresponds to the equilibrated carrier motion analogous to that observed in stationary experiments or in conventional TOF investigations of thicker samples. Because of thin samples used in this experiment the time-independent mobility has not been observed. However, the obtained mobility value of slightly less than 10^{-3} cm^2/Vs is in good agreement with that determined for holes in 1 μm thickness films at room temperature [23]. The result is rather noisy after 10 ns. The term mobility is not completely adequate to describe the carrier motion after 10 ns. The current is related to the deeply trapped carriers, which are gradually released from low energy levels. The calculation procedure formally gives mobility of the remaining charge carriers by dividing decreasing current by the gradually decreasing charge carrier density. It should be noted that the sample had low optical density at the excitation wavelength and carriers were generated homogeneously in the volume. Therefore, mobility presented in Fig. 5.5 is averaged over all drifting charge carriers – electrons and holes.

A gradual mobility decrease is in good agreement with earlier investigations of the initial carrier drift in MeLPPP by exploiting the Stark shift method [61], where it has been found that the carriers are initially separated by less than one nanometer and subsequently move at a rapidly decreasing speed. Application of the Stark shift method, however, is limited to the class of materials where this effect manifests itself [105, 62]. The mobility as high as 600 cm^2/Vs has been obtained by means of pulse-radiolysis time-resolved microwave conductivity (PR-TRMC) measurements in solution of MeLPPP polymer [15]. This is two orders of magnitude higher value than

that obtained in the present investigation. However, it should be noted that the two experiments probe significantly different processes. PR-TRMC experiment probes carrier motion at short distances along a polymer chain. While here charge carriers move in one direction perpendicularly to the film plane.

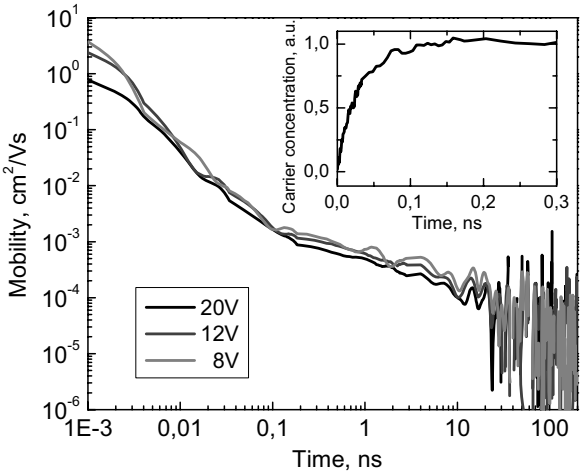

Fig. 5.5 Mobility of photogenerated charge carriers versus time at different applied voltages. Insert shows carrier generation progress (taken from [61]).

5.2 PSF-BT polymer

Fig. 5.6 shows dynamics of the second harmonic intensity in PSF-BT sample at different values of the applied voltage. Data are similar to those obtained for MeLPPP polymer. However, recovery of the second harmonic intensity is less pronounced and manifests itself only at the lowest voltage. Most probably, it is due to a slower decay of excitons in PSF-BT in comparison to MeLPPP. The drop of the second harmonic intensity continuously increases and is larger at higher voltages.

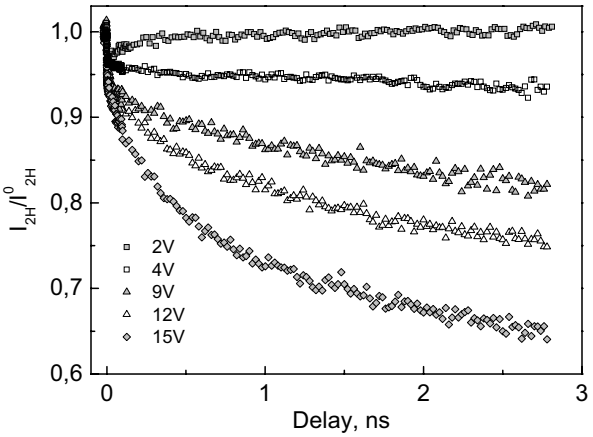

Fig.5.6 Excitation (460 nm) induced kinetics of the second harmonic intensity at different applied voltages (as indicated).

Evolution of theexcited state is very complex in PSF-BT. Spectral regions of the non-stationary states (excitons, charge carriers) overlap, and it is impossible to evaluate dynamics of the exciton density from differential absorption data as it was done for MeLPPP. Fluorescence decay kinetics were used to estimate the exciton contribution to the electric field dynamics. Assumption was made that florescence intensity is proportional to the exciton density, which, actually, is not completely correct for PSF-BT. Fig. 5.7 compares fluorescence decay with the electric field dynamics at 2V of the applied voltage obtained by using eq. (2.4). Deconvolution procedure with apparatus function was applied to fluorescence data. Approximately 60 ps time resolution is maintained in the fluorescence decay presented in Fig. 5.7. Resemblance between fluorescence and field kinetics is obvious. Thus, the exciton contribution to the electric field dynamics was estimated relying on fluorescence decay and assuming that their contribution linearly increases with an increase of the applied voltage. Decomposition of the electric field dynamics to exciton and charge carrier contributions is presented in Fig. 5.8. The exciton contribution decays with time, while the contribution of charge carrier increases. The latter contribution dominates at higher voltages because of more efficient carrier generation and a more rapid drift.

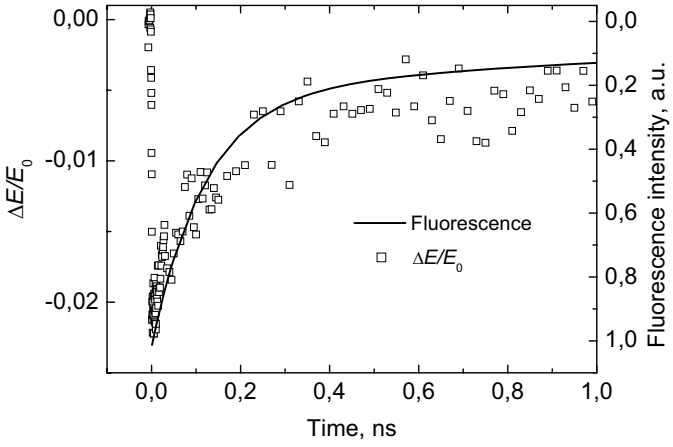

Fig. 5.7 Comparison of fluorescence decay at peak wavelength with the electric field dynamics at 2V of the applied voltage.

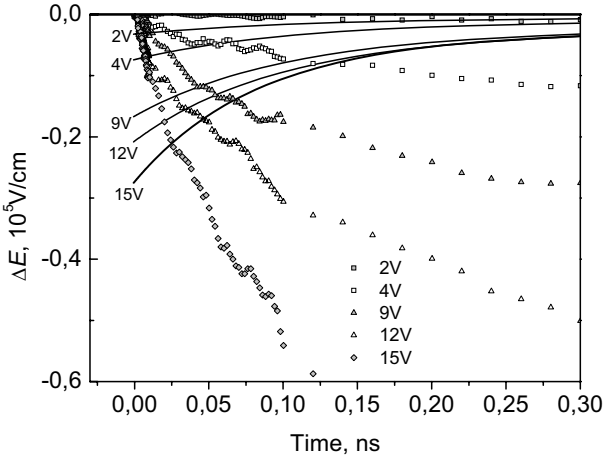

Fig. 5.8 Electric field kinetics obtained from the second harmonic signal at early times and different applied voltages (as indicated). The symbols show the charge carrier contribution and solid lines show the exciton contribution determined from the fluorescence.

Fig. 5.9 represents the amount of transported charge obtained from the charge carrier contribution to the electric field dynamics and integral mode TOF data. Like in MeLPPP, the amount of transported charge increases with an increase of the applied voltage due to the field-assisted carrier generation. However, plateau emerges, *i.e.* all photogenerated carriers are extracted, on a microsecond time scale. That is

substantially later in comparison to MeLPPP. Probably, it is due to delayed extraction of deeply trapped carriers because disorder is also substantially higher in PSF-BT.

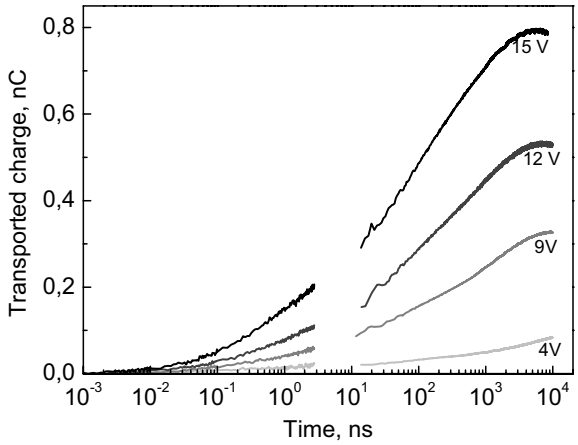

Fig. 5.9 Transported charge at different applied voltages determined from TREFISH and TOF investigations.

Temporal derivative of the transported charge, *i.e.* photocurrent, was calculated and equation (2.11) was solved numerically to obtain the average drift distance $\langle l(t) \rangle$ of the carriers. The function of carrier generation was taken from chapter 4, where it was obtained by means of the fluorescence quenching method [73, 129]. It is shown in insert of Fig. 5.10a. More than 50 % of photogenerated carriers are generated within the first picosecond after excitation. The density of photogenerated carriers n_{CC}^{0} was estimated from the integral mode TOF signal at long times, in the same way as for MeLPPP polymer. Mobility was calculated from TREFISH and TOF data according to eq. (2.14) and the result is presented in Fig. 5.10a. It decreases by about five orders of magnitude from about 0,1 cm^2/Vs at 1 ps to about $2 \cdot 10^{-6}$ cm^2/Vs at hundreds of nanoseconds. The mobility values correspond to the average value of both - electrons and holes.

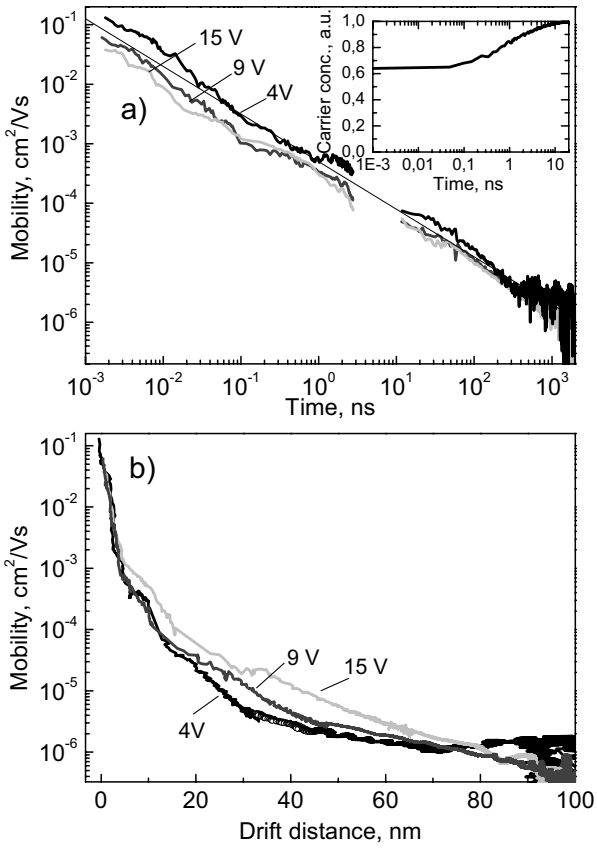

Fig. 5.10 Carrier mobility kinetics (a) and carrier mobility dependence on their drift distance (b).

The mobility kinetics follow a power law $\mu \sim t^{-\alpha}$ with α value of about 0,8. A power law is typical for dynamic processes in amorphous organic materials. It is considered evident that the mobility is limited by energetic and geometric disorder. Exponent α depends on the energetic disorder characterized by the width σ of the density of states (DOS) [101, 130]. Thus, disorder seems to control the charge transport already at very short (picosecond) times. Steady-state mobilities determined from TOF measurements on thick devices are of 10^{-3} cm^2/Vs and 10^{-5} cm^2/Vs for electrons and holes, respectively. Apparently the mobility at longer times should be attributed to holes when faster moving electrons are already extracted from the sample.

A change of the mobility on a time scale is not straightforward to relate to polymer morphology. This is more evident if temporal dependence of the mobility is translated into a spatial dependence. Fig. 5.10b shows the carrier mobility expressed as a function of the average drift distance. The carriers drift about 5 nm (during 100 ps) with high, but rapidly decreasing mobility ($10^{-1} \div 10^{-3}$ cm^2/Vs). Between 5 and 30 nm the mobility is $10^{-3} \div 10^{-5}$ cm^2/Vs. The mobility drops to 10^{-6} cm^2/Vs after about 30 - 50 nm. This value is below stationary mobility of holes. The drift distance is averaged over all carriers remaining in the sample. Thus, low mobility obtained at large distances is likely to be due to extraction of remaining deeply trapped holes. Apparently, there are three distinct transport regimes related to transport along a conjugated segment, along the single polymer chain and hopping between separate chains.

The slightly higher mobility at low voltages observed at short times might be in fact due to the saturation of the drift velocity, which occurs for applied fields of about $6 \cdot 10^5$ V/cm. Fig. 5.11 shows mobility dependence on the electric field obtained by means of the TOF method in a thick sample. Mobility obeys Poole-Frenkel behavior ($\mu \sim \exp\left(\sqrt{E}\right)$ [131]) at low fields. At higher fields it tends to saturate. The saturation is less evident for holes, but obvious for electrons at 800 $(\mathrm{V/cm})^{0,5}$. 1000 $(\mathrm{V/cm})^{0,5}$ corresponds to 10^6 V/cm field and 10 V of the applied voltage, thus saturation or even a drop of mobility may occur at 15V.

Relaxation within Gaussian shaped DOS has been studied theoretically [132]. It has been shown that decay of diffusivity, which is directly related to mobility via Einstein's equation, is faster in more disordered materials. Intuitively that is quite obvious. The opposite is observed if mobility dynamics in PSF-BT and MeLPPP are compared. Disorder is substantially lower in MeLPPP than in PSF-BT ($\sigma = 40 \div 50$ meV and $\sigma \approx 120$ meV, respectively). Mobility decay is much faster in MeLPPP than in PSF-BT during first hundreds of picoseconds. Evidently, relaxation within DOS cannot be the only cause of the mobility dynamics.

It should also be noted that the average mobility is not a perfect measure for determination of the charge transport on a picosecond time scale if generation of charge carriers is not prompt. That is because mobility is averaged over all carriers: just generated ones and those which already passed a certain distance. Thus, obtained dynamics of the mobility is a bit tangled.

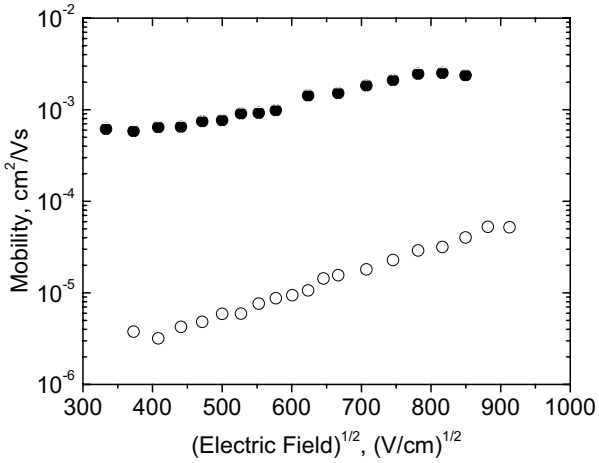

Fig. 5.11 Mobility of holes (empty circles) and electrons (filled circles) versus square root of the electric field in a 3.6 μm thick PSF-BT sample.

5.3 Concluding remarks

The electric field dynamics caused by the charge carrier generation and drift was investigated by means of TREFISH and integral mode TOF in films of MeLPPP and PSF-BT polymers. Mobility was calculated from the obtained data evaluating and eliminating the exciton contribution to field dynamics. It has been found that mobility of photogenerated charge carriers on a subnanosecond time scale is higher than stationary mobility measured in the bulk by orders of magnitude. It experiences rapid relaxation towards stationary values during the first nanosecond after photoexcitation. The influence of the electric field to this relaxation process is insignificant within the investigated range of field strengths.

6 Influence of polymer structure and temperature on initial carrier transport

Measurements of samples with a different film structure and at different temperatures were performed in order to clarify the origin of robust dynamics of carrier mobility. This chapter presents the obtained results.

6.1 Temperature influence

Fig. 6.1a shows TREFISH data obtained for PSF-BT film at different temperatures. There is a step-like drop of the $I_{2H}(t)$ signal at zero delay time. Later the $I_{2H}(t)$ signal gradually continues to decay. The $I_{2H}(t)$ signal decays more rapidly at higher temperatures. The temperature influence becomes more pronounced at longer delays. The temperature effect disappears at low temperatures; there is no difference between curves obtained at 10K and 20K. These data were used to calculate the electric field kinetics by using eq. (2.4). Fig. 6.1b shows the electric field kinetics separated into the charge carrier and exciton contributions. The exciton contribution was estimated and subtracted from the electric field kinetics on the basis of the fluorescence decay kinetics, by the same procedure as is demonstrated in chapter 5.2. Briefly, the kinetics of the second harmonic was measured at low applied voltage (Fig. 6.1a) when the carrier generation is negligible. The shape of the corresponding electric field kinetics was very similar to the fluorescence kinetics confirming that it was dominated by the exciton contribution. The exciton contribution at higher voltage was obtained by multiplying the field kinetics obtained at low voltage by the same factor as the applied voltage was increased according to eq. (2.6). Fluorescence decay kinetics only weakly depend on temperature (see Fig. 3.3a). Fluorescence kinetics below 80 K (not shown) is almost identical to that at 80 K. Fluorescence intensity is lower and decays slightly faster at higher temperatures. However, differences are not significant. Therefore, it was assumed that the exciton contribution to the change of the electric field is the same at all temperatures.

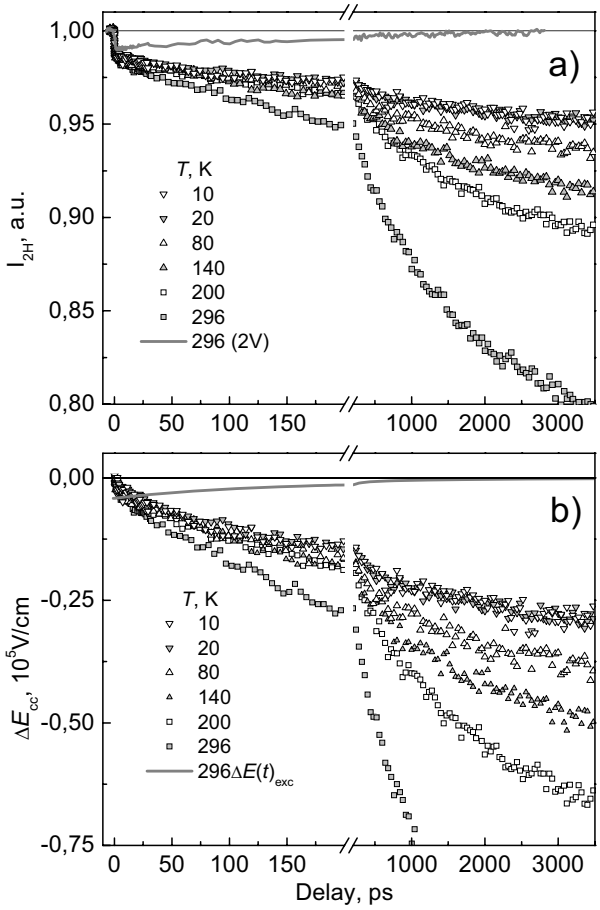

Fig. 6.1 a) The second harmonic intensity dependence on a probe pulse delay with respect to a pump pulse at different temperatures and 12V of the applied voltage (marked by the different point style), line shows result at 2V of the applied voltage. Y-axis is normalized to the second harmonic intensity without excitation. b) Field drop $\Delta E(t)_{CC}$ related to the charge carriers at different temperatures (symbols) and the exciton contribution $\Delta E(t)_{exc}$ at room temperature (solid line).

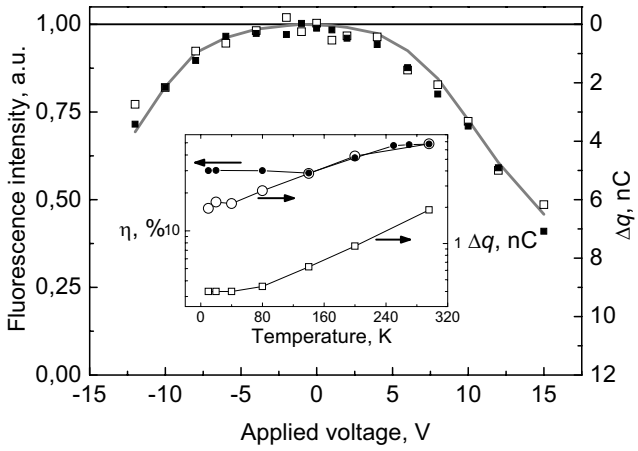

Fig. 6.2 Fluorescence quenching by the applied external voltage at two different excitation wavelengths (■ – 360 nm, □ – 500 nm). The integrated photocurrent (extracted charge) is also represented by the grey curve. The insert shows time and spectrally integrated fluorescence quenching efficiency η (●) and amount of the collected charge $\Delta q(t > \tau_{\text{extr}})$ (O) versus temperature, empty squares (□) represent values of $\Delta q(3.5\text{ns})$ obtained by TREFISH at 3.5 ns.

It is crucial to know the final density of photogenerated charge carriers n_{cc}^0 in order to calculate the average drift distance and the average mobility. It was obtained on the basis of electrical measurements of the photogenerated and extracted charge and electric field-assisted fluorescence quenching data presented in chapter 4. Fig. 6.2 compares voltage dependences of the total extracted charge and of the fluorescence quenching at room temperature. Both dependences are identical within the experimental accuracy indicating that i) all quenched excitons produced charge carriers and ii) all photogenerated carriers were extracted from the sample. Thus, the extracted charge is a good measure of the photogenerated charge density at room temperature. The situation slightly changes at low temperatures. Both the fluorescence quenching and the amount of extracted charge decrease (see insert in Fig. 6.2). Down to about 140 K both these values decrease proportionally. However, at lower temperatures the amount of the extracted charge continues to decrease while fluorescence quenching does not change. Evidently not all charge carriers are extracted at low temperature during the pulse of the applied voltage. Comparison of temperature dependences of the extracted charge and fluorescence quenching

suggests that about 50% of carriers remain trapped at 40 K and lower temperatures. Thus, the electrically measured extracted charge becomes an inadequate measure of the amount of the photogenerated charge at low temperatures. Therefore, assumption was made that the amount of the photogenerated charge follows the same temperature dependence as the fluorescence quenching. Thus, density at lower temperatures was obtained relying on temperature dependence of carrier generation built from fluorescence quenching measurements (chapter 4). Calculation of the average drift distance and carrier mobility described below supports this assumption. If one assumed that the generated charge at all temperatures equals that measured electrically, one would obtain an increase in the drift distance and carrier mobility at very low temperatures, which is completely irrational. The insert in Fig. 6.2 also shows the amount of the transported charge at 3 ns measured by the TREFISH method. This amount is about 5-7 times smaller than that measured electrically at long time.

The similar data as in insert of Fig. 6.2 are already presented in chapter 4 (Fig. 4.3). These separate measurements of separate samples gave a slightly different result concerning resemblance between fluorescence quenching and extracted charge. The discrepancy may be due to completely different experimental conditions, the excitation rate was 20 MHz in that case versus 1 kHz in this case and also excitation intensity differed by four orders of magnitude. The aging of the sample cannot be rejected as one of the possible causes either. Nevertheless the samples were encapsulated; it is a well know phenomenon that even moderate penetration of moisture and oxygen into the conjugated polymer drastically influences (reduces) the charge transport capability.

The average drift distance was calculated according to eq. (2.8) and neglecting carrier extraction. The latter simplification is fully legitimate on the short time scale. The time-dependent carrier density, also needed for mobility calculations (see below), was estimated from carrier generation data presented in chapter 4, where it has been determined that a major amount of the charge is already generated during the first picosecond. The calculated average drift distances are shown in Fig. 6.3. The time scale starts at 1 ps and a drift distance starts at zero. Thus, the initial charge carrier separation on a subpicosecond time scale here is not accounted for. Several important features of the charge drift are apparent in Fig. 6.3. First of all it is evident

that the carrier motion is independent of temperature during 100 ps. Later, the transport is temperature-activated. At room temperature charge carriers move rapidly and are one third the way towards the electrode after 3.5 ns. The motion slows down at lower temperatures. A decrease of temperature from 296 K to 80 K causes a gradual reduction of the drift distance. At 10K and 20K the curves are identical within the entire time interval under investigation, implying that temperature does not govern charge transport at low temperatures. One should note that the drift distance over the initial first hundred of picoseconds is approximately 3 nm and that is almost as much as over next 3 ns at 10 K and 20 K.

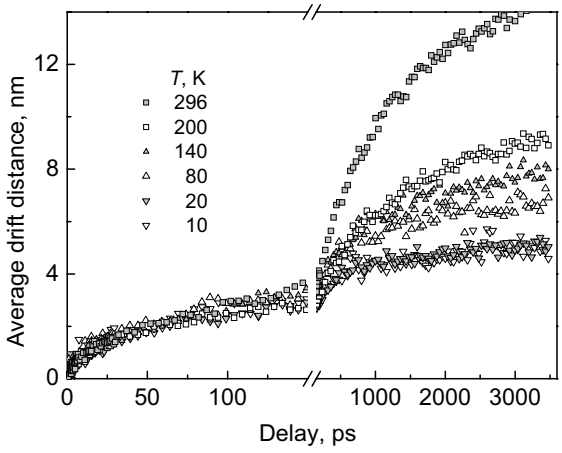

Fig. 6.3 Average drift distance of the charge carrier versus time delay after photoexcitation at different temperatures.

Fig. 6.4 shows the carrier mobility dynamics calculated by using eq. (2.15). In order to avoid large errors generated by differentiation of experimental data the electric field kinetics were approximated by polynomial functions and differentiated afterwards. The carrier mobility drops down by the order of magnitude during initial 100 ps, however the mobility values and decay rate are independent of temperature. Clear temperature dependence appears on a subnanosecond time scale. A more rapid decrease of mobility is observed at lower temperatures.

The typical approach of the transport analysis in amorphous molecular systems is based on the disorder model. This model assumes that the material is composed of randomly distributed molecular sites with different carrier energies at different sites. If we apply the disorder model to the charge transport in PSF-BT, the

charge carrier hops from site to site are determined by the energy difference and coupling between sites. It is reasonable to assume that carriers gradually occupy lower and lower energy sites (traps) during their drift and diffusional motion. Therefore, carrier hops on a subnanosecond time scale are likely to take place down in the density of states (DOS) and this transport phase still weakly depends on temperature. It resembles the triplet exciton migration, which is similar by a physical mechanism to electron transport. Temperature independent relaxation within DOS at the initial stage of exciton diffusion has been demonstrated by means of Monte-Carlo modeling [132, 133]. Mobility values at 1 ns (Fig. 6.4) at different temperatures were depicted in Arrhenius plot (not shown). Deviation from linear dependence manifested at low temperatures most probably is due to turnover from temperature activated to tunneling transfer. A line slope at higher temperatures gives the activation energy of 22 meV.

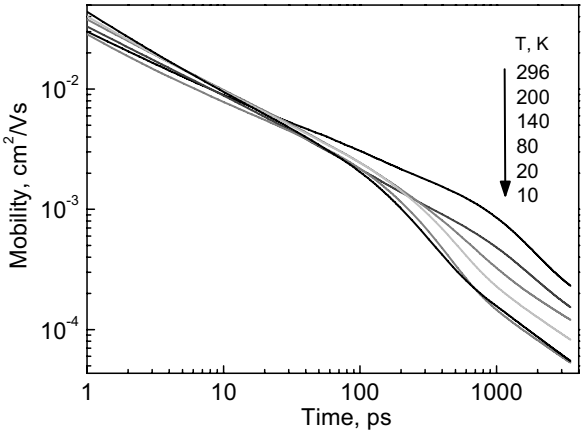

Fig. 6.4 Dynamics of carrier mobility at different temperatures.

Although this model gives a quantitative explanation of the temperature independent initial charge transport, conjugated polymers have more complex microscopic structure, which evidently plays a significant role in the charge transport at short distances. Conjugated polymers are composed of chains, which have relatively ordered regions, conjugated segments, separated by structural defects creating barriers for carrier motion. Carrier transport inside the polymer chain and between chains is expected to be rather different because of a different electron wave

function overlap between conjugated segments and polymer chains. Intrachain motion is expected to be significantly faster, which is supported by the higher macroscopic carrier mobility in polymer films with oriented chains as demonstrated for field-effect transistors [134]. Thus, the fast initial temperature independent carrier drift may also be assigned to the intrachain motion. The average charge drift of only about 3 nm during this transport phase seems to be too short for the entire intrachain carrier motion; the chain length is much longer. However, one should also take into account that this drift distance is only a projection of the total drift distance to the electric field direction. Assuming a random polymer chain orientation the total intrachain carrier drift should be about two times larger. This distance may be even larger if polymer chains are dominantly oriented along the film plane, as one may expect for the spin-cast film. Thus, the total drift distance may be of about 6 nm or longer, which is a reasonable value for the intrachain motion. Besides, holes are localized on fluorene side groups (see chapters 3, 4) and are expected to be less mobile on the ultrafast time scale already, thus the temperature independent electron drift distance is likely to exceed the 6 nm value.

The intrachain carrier motion may be of coherent type by spreading of the electron wave function within the entire polymer chain. This is evidently not the case in PSF-BT, which is truly a disordered polymer. The coherent motion should also be much faster. According to theoretical calculations the on-chain mobility in case of coherent motion may be as high as 1000 cm^2/Vs [12], while carrier mobility in PSF-BT at room temperature is of the order of (10^{-1}- 10^{-2}) cm^2/Vs even on a time scale of several ps. Incoherent carrier transport is more plausible. A common approach is that the incoherent charge transport consists of two contributions: temperature-activated hopping and tunneling transfer. The tunneling transport usually dominates at lower temperatures. The electron wave functions of neighbouring conjugated segments of the same polymer chain evidently still overlap strongly enough that carrier hops occur by tunnelling and need no thermal assistance. Certainly, one cannot completely exclude the possibility that polymer chains may also possess some defects, which create too large barriers to be overcome without thermal assistance. On the other hand, carrier hops down in the density of states, dominating at initial times, may also play a significant role.

The interchain carrier hops are much slower and need temperature assistance. The interchain motion is governed by the energetic and positional polymer disorder, which determines the macroscopic carrier mobility. Identical carrier motion dynamics at 10 K and 20 K suggest that the carrier tunneling is also responsible for the transport at very low temperatures. This is consistent with the observations of the temperature-independent macroscopic transport at low temperatures [135].

So far it is difficult to unambiguously determine which factor, relaxation within DOS or intrachain motion, plays a dominant role in the temperature-independent initial transport. According to calculations presented in [132] triplet exciton diffusivity kinetics at different temperatures start to deviate only when approaching equilibrium. Mobility dynamics (Fig. 6.4), however, gain temperature dependence before equilibrium is reached; there is no equilibrium in the investigated time interval, the mobility constantly decreases. Therefore, the relaxation within the DOS model alone hardly can explain the observed temperature dependence of the charge mobility dynamics. Hierarchical structure of conjugated polymers evidently is also important.

6.2 Morphology influence

Samples having different constitution or structural order were investigated by means of TREFISH and TOF measurements. Pure PSF-BT film manifested different behavior compared to the film made of PSF-BT and polystyrene blend containing 10% of PSF-BT. The blend constitutes non-conducting film with non-contacting chains or isles of semiconductive polymer PSF-BT in polystyrene matrix. Fig. 6.5 compares the voltage dynamics in both samples obtained by means of TREFISH measurement. The voltage drop was calculated from the second harmonic kinetics in the same way as shown before. The initial voltage drop kinetics in both samples is surprisingly similar. The differences of field dynamics appear on a nanosecond time scale. The field gradually decays in the pure PST-BT film, similarly as in MeLPPP, while it rapidly saturates in the blend. As was shown in previous chapters, the mobility can be obtained from the second harmonic kinetics taking into account the exciton contribution. However, voltage kinetics also reflects the charge transport process and can be used for comparative purposes with no effort. Similar initial kinetics shows that the

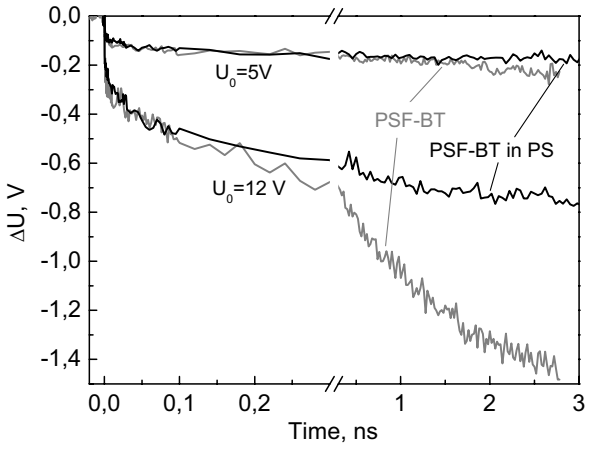

Fig. 6.5 Voltage kinetics evaluated from TREFISH measurements in PSF-BT film and in a non-conducting polystyrene film containing 10% PSF-BT at different applied voltages of 5V and 12V. Excitation intensity was adjusted in order to account for lower optical density of the blend.

initial charge transport at short distances is identical in both samples. It implies that PSF-BT polymer isles in blend have identical structure as in pure film, either initial charge transport takes place exclusively by carrier motion inside a single polymer chain.

In order to verify the importance of the intrachain carrier transport a sample, where this kind of transport is suppressed, was investigated. A liquid crystalline F8BT polymer [24, 106] was a suitable choice for this purpose. The chains of F8BT polymer can be oriented parallel to the substrate if the substrate has a specially prepared alignment layer [24]. Aligned chains are oriented perpendicularly to the electric field in the present device configuration. Fig. 6.6 shows the electric field kinetics in amorphous disordered F8BT film prepared with the alignment layer but not annealed (*i. e.* non-oriented) and in annealed (oriented) sample. The field kinetics in amorphous film is quite similar to that in PSF-BT or MeLPPP. In oriented F8BT no substantial field decay is observed on a subnanosecond to nanosecond time scale. However, TOF data show similar dynamics in oriented and non-oriented samples at later time.

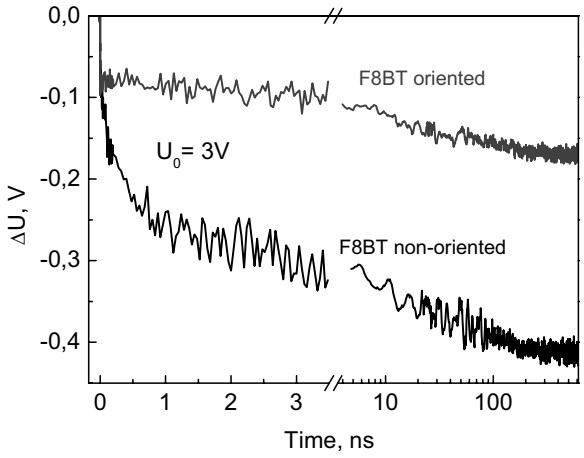

Fig. 6.6 Voltage kinetics evaluated from TREFISH and TOF measurements in oriented and non-oriented F8BT film.

In order to get deeper insight into the carrier motion mechanism the carrier drift and related voltge kinetics in MeLPPP film of 100 nm thickness were numerically simulated applying the Gaussian disorder model. Input parameters were: temperature (293 K), applied electric field and energetic disorder. The only one variable parameter was energetic disorder; various values of variance were used to get best coincidence with experimental data. The value of 0,04 eV proved to be the best choice. The simulation procedure was verified by simulating TOF data of the thick sample from [23]. Experimental transit time dependence on temperature and field was well reproduced by simulation. The simulation procedure is described in chapter 2.5. Fig. 6.7 shows the simulated kinetics as well as experimental data at the applied voltage of 20V and 8V. Good agreement between the simulated and measured kinetics at long times was obtained (curve a) by using simulation parameters obtained to reproduce TOF curves for 1 μm thick films presented in [23]. However, below 30 ns the field kinetics could not be reproduced. Moreover, any attempts to modify the parameter set and shape of DOS used for simulation did not improve the agreement on a ps-ns time scale without worsening agreement at longer times.

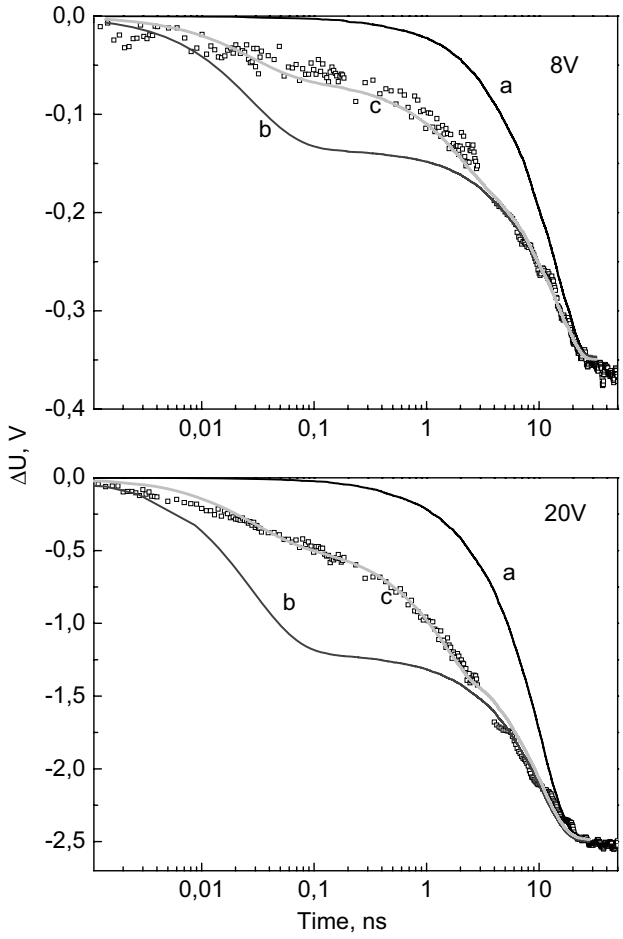

Fig. 6.7 Time dependences of the voltage attenuation (squares) by mobile charge carriers transport at 20V and 8V of the applied voltage. Solid lines show MC simulation results. The curve **a**) was obtained by means of a conventional Gaussian disorder model. The curve **b)** was obtained by a modified model assuming initial instantaneous carrier separations of 25 nm. Curve **c)** was obtained with 10 nm initial separation distance and assuming that carriers move additional 15 nm at 10 times faster hopping rate than in equilibrium at long distances.

The simulation always yielded far too slow initial dynamics in comparison with experimental results. It implied that transport properties on a short time and length scale were different compared with the steady-state or equilibrium transport on a macroscopic scale. The model was modified by introducing an instantaneous initial charge separation beyond the Coulomb binding field of the mutual pair as suggested in [136]. Initial separation of 25 nm improved the agreement in (2-20) ns time

domain, but the simulated kinetics on a picosecond time scale was now too fast (curve b). Further, the initial separation distance was reduced to 10 nm, but it was assumed that carriers move additional 15 nm with the ten times higher hopping rate compared with equilibrium. The agreement with experimental data became excellent (curve c).

From these results the following picture of charge transport after optical excitation in MeLPPP emerges. Three distinct transport domains are present. During the initial time domain, which is faster than time resolution of about 1 ps, the charge carriers are separated by about 10 nm. Subsequently, from a few ps to several hundreds of ps carriers move with high mobility additional 10÷15 nm. The following last carrier motion phase is well described by the stochastic drift determining the macroscopic equilibrium mobility.

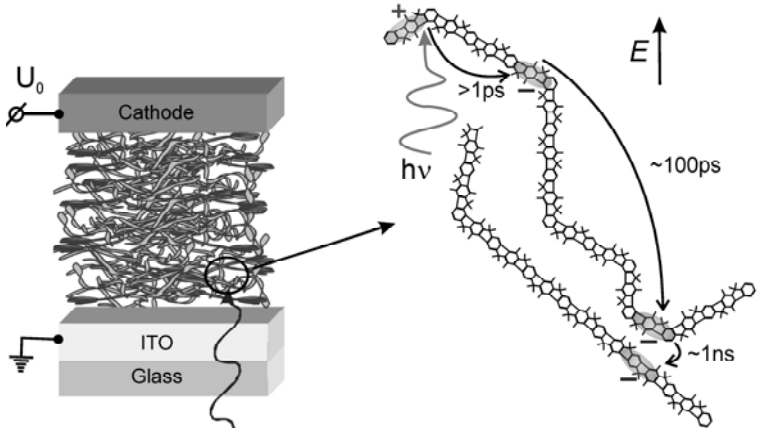

Fig. 6.8 Conceptual sketch of the charge transport processes in conjugated polymers.

It is natural to relate the observed three-phase carrier motion to the structural hierarchy of conjugated polymers (see sketch in Fig. 6.8). At short times, carriers move along a conjugated segment characterized by high electronic coupling among molecular units [11]. The 600 cm^2/Vs on-chain mobility obtained in [15] probably corresponds to this motion phase. It implies that a carrier passes the conjugated segment length on a subpicosecond time scale. The drift distance is determined by the average conjugated segment projection to the direction of the external applied field. The length of conjugated segments in MeLPPP may be significantly longer than the value obtained from absorption measurements of oligomers of MeLPPP, which is about 8 nm [137]. If both electron and hole move to opposite directions on different

segments, the initial charge displacement of about 10 nm is reasonable. Bends or twists separating conjugated segments break the conjugation of electron wavefunctions, thus creating barriers for charge transport and reducing the intrachain carrier mobility at a larger distance and on a picosecond time scale. This carrier motion phase ends when carriers reach dead ends or the chain bends to the opposite direction. According to presented data carriers move roughly 10 to 15 nm during this phase. There is slim probability for carriers to reach electrodes moving on the same polymer chain, interchain hops are unavoidable. Coupling between chains is much weaker than coupling between segments of the same chain. Simulations suggest the interchain jump time being by an order of magnitude longer (about 1 ns) than the intrachain jump-over-barrier time. Actually, the slowest event in all transport sequence limits the transport speed on a macroscopic scale. The thicker the sample the less is the contribution of the fast initial phases to the overall transmitted charge.

The concept of multiphase charge transport described above is supported by results obtained for PSF-BT and F8BT samples with different morphology. A field drop manifesting itself on a subnanosecond time scale in the pure PSF-BT and blend films is assigned to intrachain motion of the charge carriers (Fig. 6.5). The field decrease on a nanosecond time scale is assigned to interchain jumps, since it is evident only in pure PSF-BT. Chains are isolated by non-conducting polystyrene, thus interchain transport is not possible in a blend.

It is *vice versa* in oriented film of F8BT. Intrachain carrier drift is not possible due to the perpendicular alignement of chains and the electric field. Indeed, the field decay on a subnanosecond time scale in the oriented sample is much smaller in comparison to the non-oriented one. The field decay at longer times is attributed to the interchain carrier transfer being similar in oriented and non-oriented samples (Fig. 6.6).

Three carrier transport phases are distinguished in conjugated polymers corresponding to carrier motion on the conjugated segment, along the polymer chain and between chains. Although, intuitively this carrier motion picture was anticipated, it was verified experimentally for the first time by real time and space measurements. Results indicate importance of polymer morphology for the short distance nonequilibrium carrier motion, which is of utmost importance for photoelectrical

polymer devices, such as OLEDs, electrically pumped lasers [4] or solar cells where carrier motion distances hardly exceed tens of nanometers.

6.3 Concluding remarks

TREFISH measurements reveal temperature-independent charge transport in PSF-BT during initial hundred of picoseconds after photoexcitation. This phenomenon is likely due to intrachain transport or relaxation within DOS. The importance of the former is confirmed by investigations of the samples of different structure (pure PSF-BT, PSF-BT in non-conductive matrix, disordered and aligned F8BT) and Monte Carlo modeling of the charge transport in MeLPPP. TREFISH and TOF measurements together with computer modeling show the great evidence of three phase transport of charge carriers in conjugated polymers: transport along a conjugated segment, intrachain transport and interchain hopping.

General conclusions

1. Polyfluorene-based conjugated copolymer alkoxy substituted PSF-BT experiences nontrivial excited state relaxation. HOMO orbital of this polymer does not participate in optical absorption due to a poor spatial overlap between HOMO and LUMO orbitals. Within 1ps after optical excitation charge transfer (CT) exciton, having low transition dipole moment to the ground state, forms as the fluorene side group donates the electron from HOMO to the polymer backbone. Subsequent conformational stabilization of the CT exciton taking place during several nanoseconds additionally reduces the transition dipole moment. These processes significantly reduce the transition dipole moment to the ground state and lead to non-exponential fluorescence decay, but prolong the excited state lifetime to the time domain of tens of nanoseconds. Formation of the CT exciton several times reduces the fluorescence yield of the spiroconjugated PSF-BT in comparison with the F8BT polymer.

2. The applied electric field efficiently splits optically created singlet excitons into charge pairs in PSF-BT polymer. Three different time domains of carrier generation have been identified: an ultrafast phase, a subnanosecond phase and an entire lifetime phase. The charge generation efficiencies during the first and second phases were found to be almost independent of temperature being of about 25% and 10 %, respectively, at the applied electric field of $1.3 \cdot 10^6$ V/cm, while the contribution of the third phase increases from 2% at 80 K to 10% at room temperature. After the CT exciton formation, the charge pair generation rate significantly drops down; dissociation of localized CT excitons is less efficient than dissociation of the delocalized singlet excitons. The dissociation rate continues to decrease on a subnanosecond time scale, faster at low temperatures. This decrease is related to the exciton trapping at low energy sites, which reduces the exciton mobility and their probability to reach charge carrier generation centers. The last thermally activated charge carrier generation phase continues on a nanosecond time scale and its rate strongly depends on temperature being almost zero at 80 K.

3. The time-resolved electric field-assisted second harmonic generation method has been developed. This method enables probing of the electric field dynamics inside the polymer film and determination of the charge carrier drift. Generally, it is applicable

to all conjugated polymers. There are no strict restrictions to the choice of fundamental wavelength; however, avoidance of electronic resonances is preferred. Together with complementary information about the exciton and charge carrier concentrations the electric field dynamics enables determination of the charge carrier mobility and its dynamics on a femtosecond/picosecond time scale.

4. The determined electric field dynamics in MeLPPP and PSF-BT polymer films shows that the displacement current originating from the exciton polarization contributes to the electric field change. The contribution of the exciton polarization dominates at the fields below 10^5 V/cm and decreases with time as relaxation to the ground state progresses. The electric field dynamics is largely determined by the carrier drift at a higher electric field due to more efficient generation and faster drift.

5. Motion of photogenerated charge carriers in π-conjugated polymer films with different disorder and chain orientation and also in a blend of conducting and insulating polymers has been investigated. Motion of charge carriers experiences rapid dynamics after excitation. Experimental results and Monte Carlo simulation enabled distinguishing different time domains of charge transport. Initial fast transport of photogenerated charge carriers corresponds to the carrier motion along the single polymer chain or conjugated segment of the polymer chain. Slowest carrier motion phase is well described by the stochastic drift, which is attributed to interchain jumps and determines the macroscopic equilibrium mobility. Thus, the equilibrium mobility value is not applicable to the transport on nanometer scale up to tens of nanometers.

6. Transport of photogenerated charge carriers initially is temperature-independent in PSF-BT polymer. Turnover from temperature-independent to temperature-activated carrier drift takes place on the time scale of about hundred of picoseconds and at the average drift distance of several nanometers. This phenomenon is related to relaxation of the carrier energy within density of states (DOS) and intrachain carrier motion. At longer times temperature actuates charge transport and obtained result is consistent with the thermally activated hopping concept at this point. At low temperatures (10K, 20K) the charge movement is negligible, most probably due to the trapping at the bottom of DOS.

References

[1] S. Juršėnas, Organinės optoelektronikos prietaisai, Vilnius, (2007).

[2] G. Lanzani (Ed.), *Photophysics of Molecular Materials*, Wiley-VCH Verlag GmbH & Co. KGaA, Weinheim, (2006).

[3] D. C. Müller, A. Falcou, N. Reckefuss, M. Rohjan, V. Wiederhirn, P.Rudati, H. Frohne, O. Nuyken, H. Becker, and K. Meerholz, *Nature*, **421**, 829 (2003).

[4] B. K. Yap, R. D. Xia, M. Campoy-Quiles, P. N. Stavrinou, and D. D. C. Bradley, *Nature Mater*., **7**, 376 (2008).

[5] C. R. McNeill, J. J. M., Halls, R. Wilson, G. L. Whiting, S. Berkebile, M. G. Ramsey, R. H. Friend, and N. C. Greenham, *Adv. Funct. Mater*.**, 18**, 2309 (2008).

[6] T. P. I. Saragi, T. Spehr, A. Siebert, Th. Fuhrmann-Lieker, and J. Salbeck, *Chem. Rev*., **107**, 1011 (2007).

[7] Y. Wu, J. Zhang, Z. Fei, and Z. Bo, *J. Am. Chem. Soc.*, **130**, 7192 (2008).

[8] H.Klauk (Ed.), *Organic electronics, Materials, Manufacturing and Applications*, Wiley–VHC Verlag Gmbh & Co. KGaA, Weinheim (2006).

[9] D. Hertel, and H. Bässler, *Chem. Phys. Chem*, **9**, 666 (2008).

[10] H. Bässler, *Phys. Stat. Sol. B*, **175**, 15 (1993).

[11] V. Coropceanu, J. Cornil, D. A. da Silva Filho, Y. Olivier, R. Silbey, and J.-L. Bredas, *Chem. Rev*., **107**, 926 (2007).

[12] J. W. van der Horst, P. A. Bobbert, M. A. J. Michels, and H. Bässler, *J. Chem. Phys*., **114**, 6950 (2001).

[13] A. Horvath, G. Weiser, C. Lapersonne-Meyer, M. Schott, and S. Spagnoli, *Phys. Rev. B*, **53**, 13507 (1996).

[14] F. Dubin, R. Melet, T. Barisien, R. Grousson, L. Legrand, M. Schott, and V. Voliotis, *Nature Phys*., **2**, 32 (2005).

[15] P. Prins, F. C. Grozema, J. M. Schins, S. Patil, U. Scherf, and L. D. A. Siebbeles, *Phys. Rev. Lett.*, **96**, 146601 (2006).

[16] Ch. Bosshard, G. Knöpfle, P. Pretre, and P. Günter, *J. Appl. Phys*., **71**, 1594 (1992).

[17] J.W. Perry, in *Nonlinear Optical-Properties of Molecules and Materials,* in *Materials for Nonlinear Optics* (edited by S. R. Marder, E. J. Sohn, and G. D. Stucky), American Chemical Society, Washington, D.C., p. 67 (1991).

[18] R. M. Corn, and D. A. Higgins, *Chem. Rev.*, **94**, 107 (1994).

[19] Y. D. Glinka, T.V. Shahbazyan, I. E. Perakis, N. H. Tolk, X. Liu, Y. Sasaki, and J. K. Furdyna, *Appl. Phys. Lett*., **81**, 3717 (2002).

[20] M. Nagel, C. Meyer, H.-M. Heiliger, T. Dekorsy, H. Kurz, R. Hey, and K. Ploog, *Appl. Phys. Lett*., **72**, 1018 (1998).

[21] T. Manaka, E. Lim, R. Tamura, and M. Iwamoto, *Nature Photon.*, **1**, 581 (2007).

[22] G. Hadziioannou and G. G. Malliaras (eds.), *Semiconducting Polymers*, Wiley-VCH Verlag GmbH & Co. KGaA, Weinheim, (2007).

[23] D. Hertel, H. Bässler, U. Scherf, H. H. Hörhold, *J. Chem. Phys.*, **110**, 9214 (1999).

[24] J. Zaumseil, C. Groves, J. M. Winfield, N. C. Greenham, and H. Sirringhaus, *Adv. Funct. Mater*., **18**, 3630 (2008).

[25] H. Shirakawa, E. J. Louis, A. G. MacDiarmid, C. K. Chiang, and A. J. Heeger, *J Chem Soc Chem Comm.*, 579 (1977).

[26] http://nobelprize.org.

[27] W. Barford, *Electronic and Optical Properties of Conjugated Polymers*, Oxford University Press, New York (2005).

[28] Q. Zhu, J. E. Fischer, R. Zuzok, and S. Roth, *Solid State Comm.*, **83**, 179 (1992).

[29] C. R. Fincher, Jr., C. -E. Chen, A. J. Heeger, and A. G. MacDiarmid J. B. Hastings, *Phys. Rev. Lett*., **48**, 100 (1982).

[30] J. C. W. Chien, *Macromol. Chem*., **3**, 655 (1982).

[31] S. Stafström, *Phys Rev B*, **32**, 4060 (1985).

[32] U. Scherf, D. Neher, *Adv. Polym. Sci.*, **212**,1 (2008).

[33] J. Pei, W. L. Yu, W. Huang, A. J. Heeger, *Chem. Commun.*, 1631 (2000).

[34] Q. Hou, Y. Xu, W. Yang, M. Yuan, J. Peng, Y. Cao, *J. Mater. Chem*., **12**, 2887 (2002).

[35] J. Salbeck, In *Inorganic and Organic Electroluminescence*, (edited by R. H. Mauch, H. E. Gumlich); Wissenschaft und Technik Verlag, Berlin, p 243 (1996).

[36] R. Pudzich, T. Fuhrmann-Lieker, J. Salbeck, *Adv. Polym. Sci*., **199**, 83 (2006).

[37] F. Laquai, and D. Hertel, *Appl. Phys. Lett*., **90**, 142109 (2007).

[38] M. C. Gather, R. Alle, H. Becker, and K. Meerholz, *Adv. Mater*., **19**, 4460 (2007).

[39] N. Karl, *Synthetic Metals*, **133–134**, 649–657 (2003).

[40] W. G. Gill, *J. Appl. Phys*., **43**, 5033 (1972).

[41] S. F. Alvarado, S. Barth, H. Bässler, U. Scherf, J. W. van der Horst, P. A. Bobbert, and M. A. J. Michels, *Advanced Functional Materials*, **12,** 117 (2002).

[42] V. I. Arkhipov, P. Heremans, E. V. Emelianova, G. J. Adriaenssens, and H. Bässler, *Appl. Phys. Lett*., **82,** 3245 (2003).

[43] D. Monroe, *Phys. Rev. Lett*., **54**, 146 (1985).

[44] M. C. J. M. Vissenberg, M. Matters, *Phys. Rev. B*, **57**, 12 964 (1998).

[45] C. Tanase, Unified charge transport in disordered organic field-effect transistors and light-emitting diodes, Ph.D. thesis, University of Groningen (2005).

[46] A. Miller, E. Abrahams, *Phys. Rev*., **120**, 745 (1960).

[47] R. A. Marcus, *J. Chem. Phys.*, **24**, 966 (1956).

[48] D. H. Dunlap, P. E. Parris, and V. M. Kenkre, *Phys. Rev. Lett*., **77**, 542 (1996).

[49] S. V. Novikov, D. H. Dunlap, V. M. Kenkre, P. E. Parris, A. V. Vannikov *et al., Phys. Rev. Lett*., **81**, 4472 (1998).

[50] Z. G. Yu, D. L. Smith, A. Saxena, R. L. Martin, and A. R. Bishop, *Phys. Rev. Lett*., **84**, 721 (2000).

[51] J. W. van der Horst, P. A. Bobbert, M. A. J. Michels, and H. Bässler, *J. Chem. Phys.*, **114**, 6950 (2001).

[52] C. Tanase, E. J. Meijer, P.W.M. Blom, and D.M. de Leeuw, *Phys. Rev. Lett*., **91**, 216601 (2003).

[53] P. W. M. Blom, M. J. M. de Jong, and M. G. van Munster, *Phys. Rev.*, *B*, **55**, 656 (1997).

[54] N. I. Craciun, J. Wildeman, and P.W. M. Blom, *Phys. Rev. Lett.*, **100**, 056601 (2008).

[55] D. Moses, J. Wang, G. Yu, and A. J. Heeger, *Phys. Rev. Lett.*, **80**, 2685 (1998).

[56] G. Juška, K. Genevičius, R. Österbacka, K. Arlauskas, T. Kreouzis, D.D.C. Bradley, and H. Stubb, *Phys. Rev.* B, **67**, 081201 (2003).

[57] R. Österbacka, K. Genevičius, A. Pivrikas, G. Juška, K. Arlauskas, T. Kreouzis, D.D.C. Bradley, H. Stubb, *Synthetic Metals*, **139**, 811 (2003).

[58] C. H. Lee, G. Yu, D. Moses and A. J. Heeger, *Phys. Rev*. *B*, **49**, 2396 (1994).

[59] R. J. O. M. Hoofman, M. P. de Haas, L. D. A. Siebbeles, and J. M. Warman, *Nature*, **392**, 54 (1998).

[60] E. Hendry, M. Koeberg, J. M. Schins, H. K. Nienhuys, V. Sundström, L. D. A. Siebbeles, A. Bonn, *Phys. Rev. B*, **71**, 125201 (2005).

[61] Gulbinas, V. Y. Zaushitsyn, V. Sundström, D. Hertel, H. Bässler, and A. Yartsev, *Phys. Rev. Lett*., **89**, 107401 (2002).

[62] J. Cabanillas-Gonzalez, J. T. Virgili, A. Gambetta, G. Lanzani, T. D. Anthopoulos, D. M. de Leeuw, *Phys. Rev. Lett.*, **96**, 106601 (2006).

[63] E.A.Silinsh, and V.Čapek, Organic Molecular Crystals. Interaction, Localization and Transport Phenomena, AIP Press, New York (1994).

[64] R. G. Kepler, *Phys. Rev*., **119**, 1226 (1960).

[65] O. H. LeBlanc, *J. Chem. Phys*., **33**, 626(1960).

[66] "Krūvininkų dreifinio judrio tyrimas organiniuose fotopuslaidininkiuose" Laboratorinio darbo aprasymas, VU FF kietojo kuno elektronikos katedra.

[67] G. Juška, K. Arlauskas, M. Viliūnas J. Kočka, *Phys. Rev. Lett*., **84**, 4946 (2000).

[68] A. J. Mozer, N. S. Sariciftci, L. Lutsen, D. Vanderzande, R. Österbacka, M. Westerling, G. Juška, *Appl. Phys. Lett*., **86**, 112104 (2005).

[69] M. A. Lampert, P. Mark, *Current Injection in Solids*, Academic Press, New York (1970).

[70] G. Horowitz, R. Hajlaoui, H. Bouchriha, R. Bourguiga, and M. Hajlaoui, *Advanced Materials*, **10,** 365 (1998).

[71] G. Horowitz, *Semiconducting Polymers*, Wiley–VHC Verlag Gmbh & Co. KGaA, Weinheim (2007).

[72] J. M. Warman, P. de Haas, and A. Hummel., *Chem. Phys. Lett*., **22**, 480 (1973).

[73] W. Graupner, G. Cerullo, G. Lanzani, M. Nisoli, E. J. W. List, G. Leising, S. De Silvestri, *Phys. ReV. Lett*., **81**, 3259 (1998).

[74] A. Haugeneder, M. Neges, C. Kallinger, W. Spirkl, U. Lemmer, J. Feldmann, *J. Appl. Phys*., **85**, 1124 (1999).

[75] J. Stampfl, W. Graupner, G. Leising, U. Scherf, *J. Lumin*., **63**,117 (1995).

[76] U. Scherf, *J. Mater. Chem*., **9**, 1853 (1999).

[77] H. J. Bolink, E. Coronado, D. Repetto, and M. Sessolo, *Appl. Phys. Lett*., **91**, 223501 (2007).

[78] H. J. Snaith, N. G. Greenham, R. H. Friend, *Adv. Mater*., **16**, 1640 (2004).

[79] J. Cornil, I. Gueli, A. Dkhissi, J. C. Sancho-Garcia, E. Hennebicq, J. P. Calbert, V. Lemaur, D. Beljonne, and J. L. Bredas, *J. Chem. Phys*., **118**, 6615 (2003).

[80] A. R. Buckley, M. D. Rahn, J. Hill, J. Cabanillas-Gonzalez, A. M. Fox, and D. D. C. Bradley, *Chem. Phys. Lett*., **339**, 331 (2001).

[81] A. C. Morteani, P. Sreearunothai, L. M. Herz, R. H. Friend, and C. Silva, *Phys. Rev. Lett*., **92**, 247402 (2004).

[82] R. Xia, G. Heliotis, P. N. Stavrinou, and D. D. C. Bradley, *Appl. Phys. Lett*., **87**, 031104 (2005).

[83] U. Scherf, *Macromol. Chem. Phys*., **193**, 1127 (1992).

[84] O. A. Aktsipetrov, A. A. Fedyanin, J. I. Dadap, and M. C. Downer, *Laser Physics*, **6**, 1142 (1996).

[85] D. R. Lide (Ed.) Handbook of Chemistry and Physics on CD-ROM Version, CRC Press, (2008).

[86] H. Ishii, K. Sugiyama, E. Ito, and K. Seki, *Adv. Mater*., **11**, 605 (1999).

[87] G. Cerulo, S. Stagira, M. Nisoli, S. De Silvestri, G. Lanzani, G. Kranzelbinder, W. Groupner, and G. Leising, *Phys. Rev. B*, **57**, 1280, (1998).

[88] N. Metropolis, *The beginning of the Monte Carlo method*, Los Alamos Science (Special Issue dedicated to Stanislaw Ulam), 125 (1987) http://library.lanl.gov/la-pubs/00326866.pdf.

[89] http://en.wikipedia.org/wiki/Marsaglia_polar_method (retrieved 2008).

[90] P. Zacharias, M. C. Gather, M. Rojahn, O. Nuyken, K. Meerholz, *Angew. Chem., Int. Ed*., **46**, 4388 (2007).

[91] C. Rothe, R. Guentner, U. Scherf, and A. P. Monkman, *J. Chem. Phys*., **115**, 9557 (2001).

[92] D. Hertel, H. Bässler, R. Guentner, and U. Scherf, *J. Chem. Phys*., **115**, 10007 (2001).

[93] C. Rothe, S. M. King, and A. P. Monkman, *Phys. Rev. B*, **72**, 085220 (2005).

[94] A. C. Morteani, A. S. Dhoot, J.-S. Kim, C. Silva, N. C. Greenham, C. Murphy, E. Moons, S. Cina, J. H. Burroughes, and R. H. Friend, *Adv. Mater*., **15**, 1708 (2003).

[95] A. C. Morteani, P. Sreearunothai, L. M. Herz, R. H. Friend, and C. Silva, *Phys. Rev. Lett*., **92**, 247402 (2004).

[96] S. M. King, S. I. Hintschich, D. Day, C. Rothe, and A. P. Monkman, *J. Phys. Chem. C*, **111**, 18759 (2007).

[97] S. I. Hintschich, C. Rothe, S. M. King, S. J. Clark, and A. P. Monkman, *J. Phys. Chem. B*, **112**, 16300 (2008).

[98] S. M. King, C. Rothe, D. Dai, and A. P. Monkman, *J. Phys. Chem. B*, **124**, 234903 (2006).

[99] P. Maslak and A. Chopra, *J. Am. Chem. Soc*., **115**, 9331 (1993).

[100] P. Maslak, A. Chopra, C. R. Moylan, R. Wortmann, S. Lebus, A. L. Rheingold, and G. P. A. Yap, *J. Am. Chem. Soc*., **118**, 1471 (1996).

[101] S. C. J. Meskers, J. Hübner, M. Oestreich, and H. Bässler, *J. Phys. Chem*., **105**, 9139 (2001).

[102] C. Silva, M. A. Stevens, D. M. Russel, S. Setayesh, K. Müller, R. H. Friend, *Synth. Met*., **116**, 9 (2001).

[103] M. A. Stevens, C Silva, D. M. Russell, and R. H. Friend, *Phys. Rev. B*, **63**, 165213 (2001).

[104] C. Gadermaier, L. Romaner, T. Piok, E. J. W. List, B. Souharce, U. Scherf, G. Cerullo, and G. Lanzani, *Phys. Rev. B*, **72**, 045208 (2005).

[105] V. Gulbinas, R. Kananavičius, L. Valkūnas, and H. Bässler, *Phys. Rev. B*, **66**, 233203 (2002).

[106] L. L. Chua, J. Zaumseil, J. F. Chang, E. C. W. Ou, P. K. H. Ho, H. Sirringhaus, R. H. Friend, R. H.. *Nature*, **434**, 194 (2005).

[107] A. J. Campbell, D. D. C. Bradley, H. Antoniadis, *J. Appl. Phys*., **89**, 3343 (2001).

[108] C. Reichardt, *Chem. Rev*., **94**, 2319 (1994**)**.

[109] S. Stagira, M. Nisoli, G. Lanzani, and S. De Silvestri, T. Cassano and R. Tommasi, F. Babudri, G. M. Farinola, and F. Naso, *Phys. Rev. B*, **64**, 205205 (2001).

[110] C. Gadermaier, G. Cerullo, G. Sansone, G. Leising, U. Scherf, and G. Lanzani, *Phys. Rev. Lett*., **89**, 117402 (2002).

[111] D. Moses, A. Dogariu, and A. J. Heeger, *Phys. Rev. B*, **61**, 9373 (2000).

[112] T. Virgili, D. Marinotto, C. Manzoni, G. Cerullo, and G. Lanzani, *Phys. Rev. Lett*., **94**, 117402 (2005).

[113] L. Lüer, H.-J. Egelhaaf, D. Oelkrug, C. Gadermaier, G. Cerullo, and G. Lanzani, *Phys. Rev. B*, **68**, 155313 (2003).

[114] P. B. Miranda, D. Moses, and A. J. Heeger, *Phys. Rev. B*, **70**, 085212 (2004).

[115] E. Hendry, M. Koeberg, J. M. Schins, L. D. A. Siebbeles, and M. Bonn, *Phys. Rev. B*, **70**, 033202 (2004).

[116] C. Silva, A.S. Dhoot, D.M. Russell, M.A. Stevens, A.C. Arias, J.D. MacKenzie, N.C. Greenham, R.H. Friend, S. Setayesh, and K. Müllen, *Phys. Rev. B*, **64**, 125211 (2001).

[117] S.V. Frolov, Z. Bao, M. Wohlgenannt, and Z.V. Vardeny, *Phys. Rev. Lett*., **85**, 2196 (2000).

[118] E. V. Emelianova, M. Van der Auweraer, H. Bässler, *J. Chem. Phys.*, **128**, 224709 (2008).

[119] V. I. Arkhipov and E. V. Emelianova, S. Barth, and H. Bässler, *Phys. Rev. B*, **61**, 8207 (2000).

[120] V. Gulbinas,Yu. Zaushitsyn, H. Bässler, A. Yartsev, and V. Sundström, *Phys. Rev. B*, **70**, 035215 (2004).

[121] A. Köhler, D. A. dos Santos, D. Beljonne, Z. Shuai, J.-L. Brėdas, A. B. Holmes, A. Kraus, K. Müllen, and R. H. Friend, *Nature*, **392**, 903 (1998).

[122] J. G. Müller, U. Lemmer, J. Feldmann, and U. Scherf, *Phys. Rev. Lett.*, **88**, 147401 (2002).

[123] M. S. Mehata, C.-S. Hsu, Y.-P. Lee and N. Ohta, *J. Phys. Chem. C*, **113**, 11907 (2009).

[124] Yu. Zaushitsyn, V. Gulbinas, D. Zigmantas, F. Zhang, O. Inganäs, V. Sundström and A. Yartsev, *Phys. Rev. B*, **70**, 075202 (2004).

[125] V. I. Arkhipov, H. Bässler, M. Deussen, and E. O. Göbel , R. Kersting and H. Kurz, U. Lemmer and R. F. Mahrt, *Phys. Rev B*, **52**, 4932 (1995).

[126] R. Kersting, U. Lemmer, M. Deussen, H. J. Bakker, R. F. Mahrt, H. Kurz, V. I. Arkhipov, H. Bässler, and E. O. Göbel, *Phys. Rev. Lett*., **73**, 1440 (1994).

[127] G. Lanzani, G. Cerullo, S. Stagira, and S. De Silvestri, F. Garnier, *Phys. Rev. B*, **58**, 7740 (1998).

[128] M. Scheidler, U. Lemmer, R. Kersting, S. Karg, W. Riess, B. Cleve, R. F. Mahrt, H. Kurz, H. Bässler, E. O. Göbel and P. Thomas, *Phys. Rev. B*, **54**, 5536 (1996).

[129] D. Hertel, E. V. Soh, H. Bässler, and L. J. Rothberg, *Chem. Phys. Lett*., **361**, 99 (2002).

[130] C. Rothe,and A. P. Monkman, *Phys. Rev. B*, **68**, 075208 (2003).

[131] J. Frenkel, *Phys. Rev*., **54**, 647 (1938).

[132] B. Movaghar, M. Grünewald, B. Ries, H. Bässler, D. Würtz, *Phys. Rev. B*, **33**, 5545 (1986).

[133] R. Richert, H. Bässler, *Chem. Phys. Lett*., **118**, 235 (1985).

[134] H. Sirringhaus, *et al., Nature*, **401**, 685-688 (1999).

[135] G. Horowitz, M. E. Hajlaoui, and R. Hajlaoui, *J. Appl. Phys*., **87**, 4456 (2000).

[[136]] Juška, G. *et. al*. Initial transport of photogenerated charge carriers in π-conjugated polymers**.** *Phys. Rev. B*, **67**, 081201 (2003).

[137] J. Grimme, M. Kreyenschmidt, F. Uckert, K. Müllen, U. Scherf, *Adv. Mater*., **7**, 292 (1996).